

AWARD NUMBER: W81XWH-12-1-0457

TITLE: Noninvasive Detection and Differentiation of Axonal Injury/Loss,
Demyelination, and Inflammation

PRINCIPAL INVESTIGATOR: Sheng-Kwei Song

CONTRACTING ORGANIZATION: Washington University
SAINT LOUIS, MO 63130-4862

REPORT DATE: OCTOBER 2014

TYPE OF REPORT: Annual

PREPARED FOR: U.S. Army Medical Research and Materiel Command
Fort Detrick, Maryland 21702-5012

DISTRIBUTION STATEMENT: Approved for Public Release;
Distribution Unlimited

The views, opinions and/or findings contained in this report are those of the author(s) and should not be construed as an official Department of the Army position, policy or decision unless so designated by other documentation.

REPORT DOCUMENTATION PAGE				Form Approved OMB No. 0704-0188	
Public reporting burden for this collection of information is estimated to average 1 hour per response, including the time for reviewing instructions, searching existing data sources, gathering and maintaining the data needed, and completing and reviewing this collection of information. Send comments regarding this burden estimate or any other aspect of this collection of information, including suggestions for reducing this burden to Department of Defense, Washington Headquarters Services, Directorate for Information Operations and Reports (0704-0188), 1215 Jefferson Davis Highway, Suite 1204, Arlington, VA 22202-4302. Respondents should be aware that notwithstanding any other provision of law, no person shall be subject to any penalty for failing to comply with a collection of information if it does not display a currently valid OMB control number. PLEASE DO NOT RETURN YOUR FORM TO THE ABOVE ADDRESS.					
1. REPORT DATE October 2014		2. REPORT TYPE Annual		3. DATES COVERED 30 Sep 2013 - 29 Sep 2014	
4. TITLE AND SUBTITLE Noninvasive Detection and Differentiation of Axonal Injury/Loss, Demyelination, and Inflammation				5a. CONTRACT NUMBER	
				5b. GRANT NUMBER W81XWH-12-1-0457	
				5c. PROGRAM ELEMENT NUMBER	
6. AUTHOR(S) Sheng-Kwei Song, William M. Spees, Peng Sun, Yong Wang, Anne Cross E-Mail: ssong@wustl.edu				5d. PROJECT NUMBER	
				5e. TASK NUMBER	
				5f. WORK UNIT NUMBER	
7. PERFORMING ORGANIZATION NAME(S) AND ADDRESS(ES) Washington University St. Louis, MO 63110-1010				8. PERFORMING ORGANIZATION REPORT NUMBER	
9. SPONSORING / MONITORING AGENCY NAME(S) AND ADDRESS(ES) U.S. Army Medical Research and Materiel Command Fort Detrick, Maryland 21702-5012				10. SPONSOR/MONITOR'S ACRONYM(S)	
				11. SPONSOR/MONITOR'S REPORT NUMBER(S)	
12. DISTRIBUTION / AVAILABILITY STATEMENT Approved for Public Release; Distribution Unlimited					
13. SUPPLEMENTARY NOTES					
14. ABSTRACT During year 2 of this funding support, we have developed more tools to demonstrate that DBSI is the future of diffusion MRI and neuroimaging modality to effectively detect underlying white matter tract pathologies noninvasively. We developed an objective quantitative histology analysis approach that allows an exact match between histology images and MRI maps. For situations where co-registered MRI-histology is not available due to data acquisition difficulties, the objective quantitative analysis of histology remains readily applicable. Current preliminary results suggest that DBSI detected axonal injury, demyelination, and inflammation closely correlated with histology findings. Most interestingly, results from the shorter time course of DBSI of optic nerve from EAE mice during acute ON indicated that visual impairment did not reflect underlying severity of optic nerve damage. DBSI detects all pathologies in optic nerves during ON.					
15. SUBJECT TERMS Multiple sclerosis, diffusion basis spectrum imaging, diffusion tensor imaging, EAE, inflammation, axonal injury, curizone, demyelination					
16. SECURITY CLASSIFICATION OF:			17. LIMITATION OF ABSTRACT	18. NUMBER OF PAGES	19a. NAME OF RESPONSIBLE PERSON
a. REPORT	b. ABSTRACT	c. THIS PAGE			USAMRMC
U	U	U	UU	37	19b. TELEPHONE NUMBER (include area code)

Table of Contents

	<u>Page</u>
1. Introduction.....	4
2. Keywords.....	4
3. Overall Project Summary.....	4 – 8
4. Key Research Accomplishments.....	8
5. Conclusion.....	8
6. Publications, Abstracts, and Presentations.....	8 – 9
7. Inventions, Patents and Licenses.....	9
8. Reportable Outcomes.....	9
9. Other Achievements.....	9
10. References.....	9
11. Appendices.....	10

Introduction

Acute neurological impairments in MS are associated with the combined effect of the underlying inflammation, axonal injury, and demyelination, while long-term MS disability is due to the extent of permanent axonal damage, may or may not be dependent on the frequency or severity of relapses¹⁻¹⁰. In the current proposal, *in vivo* diffusion basis spectrum imaging (DBSI) has been employed to simultaneously quantify axonal injury, demyelination, and inflammation in CNS white matter, correlating with postmortem immunohistochemical staining, in experimental autoimmune encephalomyelitis (EAE) and cuprizone treated mice.

Keywords

Multiple sclerosis, diffusion basis spectrum imaging, diffusion tensor imaging, EAE, inflammation, axonal injury, cuprizone, demyelination

Overall project Summary

The primary goal of this project is to quantitatively validate diffusion basis spectrum imaging (DBSI) derived metrics of axonal injury, demyelination, and inflammation with post-MRI histology. Our work during this funding period (1) support our hypothesis that DBSI reflects underlying white matter pathologies, (2), DBSI derived white matter pathological metrics reflect acute neurological impairments, and (3) acute neurological impairments do not correlate with underlying white matter pathologies. In the following, we summarize the progress of the proposed studies in the current funding period.

1. Longitudinal and cross-sectional DBSI of corpus callosum (CC) from cuprizone treated mice

The approved statement of work for the year one covers all tasks proposed in specific aim 1 “*Longitudinal DBSI evaluation of evolving pathology of corpus callosum from mice treated with cuprizone for 0, 4, and 8 weeks followed by 4, and 8 weeks of recovery. Cross sectional DBSI studies will be performed on the same longitudinal time points for histology validation of DBSI findings. (Months 1 – 14)*”. At present time, we have completed the proposed longitudinal (Table 1) and cross-sectional (Table 2) DBSI-histology studies on CC from cuprizone treated mice.

Table 1. Summary of Longitudinal DBSI					
	0 weeks	6 weeks	12 weeks	12 + 6 weeks	12 + 12 weeks
Control	6	scanner down	6	3 (50% mortality)	3
Cuprizone	8	scanner down	7	7	7

Table 2. Summary of Cross-Sectional DBSI-IHC			
	6 weeks	12 weeks	12 + 6 weeks
Control	6	5	5
Cuprizone	6	6	6

Previously, we have demonstrated that DBSI derived axial diffusivity (AD) accurately reflected axonal injury in CC from mice after 4 weeks of cuprizone feeding by correctly modeling increased cellularity resulting from microglial activation.¹¹ In the present study, we examined CC at the chronic stage of cuprizone feeding. Our finding suggested that there is minimal axonal injury as previously reported using DTI.¹² Our results also indicated that at the chronic stage, microglial activation subsided and both DTI and DBSI derived AD and radial diffusivity (RD) was capable to reflect axon and myelin integrity (data are being organized and correlated with quantitative histology for potential publication). Most interestingly, increased inter-axonal and extracellular space seen at chronic stage by previous electron micrograph (EM) examinations was also seen by DBSI derived non-restricted isotropic diffusion tensor component fraction in current study.

2. New approach for quantitative validation of DBSI derived pathological metrics

To validate *in vivo* DBSI findings with quantitative histology, we have developed a new approach to automatically quantify histology slides at high resolution after histology-DBSI image co-registration. Herein, we report the development of this method using autopsy human MS spinal cord specimens as the example.

Cervical spinal cord specimens were obtained following autopsy from three MS patients. The spinal cord and other tissues were fixed in 10% formalin in phosphate buffered saline (PBS) at room temperature at time of autopsy. A segment of the three fixed MS cervical spinal cord tissues was placed in a 3-ml syringe with 10% formalin and was imaged using a custom-made solenoid coil on an Agilent DirectDrive console equipped with a 4.7 T magnet and a 15-cm inner diameter, actively shielded Magnex gradient coil (60 G/cm, 270 μ s rise time). The data acquisition parameters are: repetition time (TR) 2s, spin echo time (TE) 39 ms, time between

application of gradient pulse 20 ms, diffusion gradient on time 8 ms, slice thickness 0.5 mm, number of slices 5, field-of-view $2.4 \times 2.4 \text{ cm}^2$, data matrix 96×96 . Diffusion sensitizing gradients were applied in 99 directions with max b-value = 3200 s/mm^2 . In-plane resolution was $250 \times 250 \mu\text{m}^2$. Following MR imaging, the formalin fixed MS spinal cord was embedded in paraffin and sectioned using a sliding microtome at $5\text{-}\mu\text{m}$ thick. Sections were individually stained with Bielschowsky's silver, Hematoxylin and Eosin (H&E), and Luxol Fast Blue-Periodic Acid Schiff (LFB-PAS) stains. Images were acquired with a Hamamatsu NanoZoomer 2.0-HT System (Hamamatsu, Japan) with a 40x objectives.

ImageJ (<http://rsbweb.nih.gov/ij/>) with NDPI Tools plugin¹³ was employed to process the full-view raw histology

images. At 40x objective, the raw histology image had $0.23 \mu\text{m}/\text{pixel}$ spatial resolution. One MRI image voxel ($250 \mu\text{m}^2$ in-plane) corresponded to 1087×1087 histology image pixels. NDPI Tools plugin was employed to split the large raw histology images into small square pixels containing 1087×1087 pixels, equivalent to a single MRI imaging voxel.

Each small RGB color histology image pixel was converted to indexed color image using minimum variance quantization method.¹⁴ Minimum variance quantization allocates fewer entries to colors that appear infrequently. The accuracy of the colors is higher than with uniform color quantization for a given number of colors. In this example, twenty indexed colors

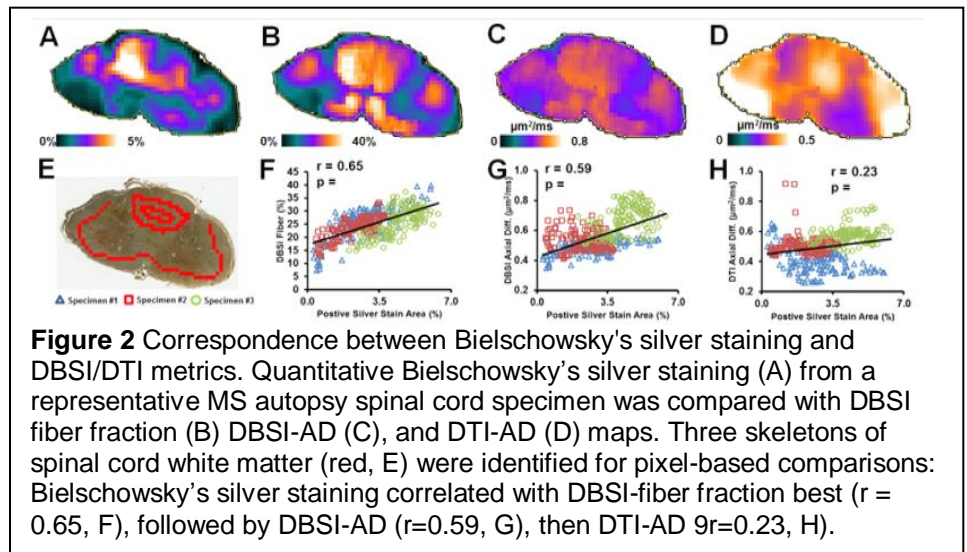
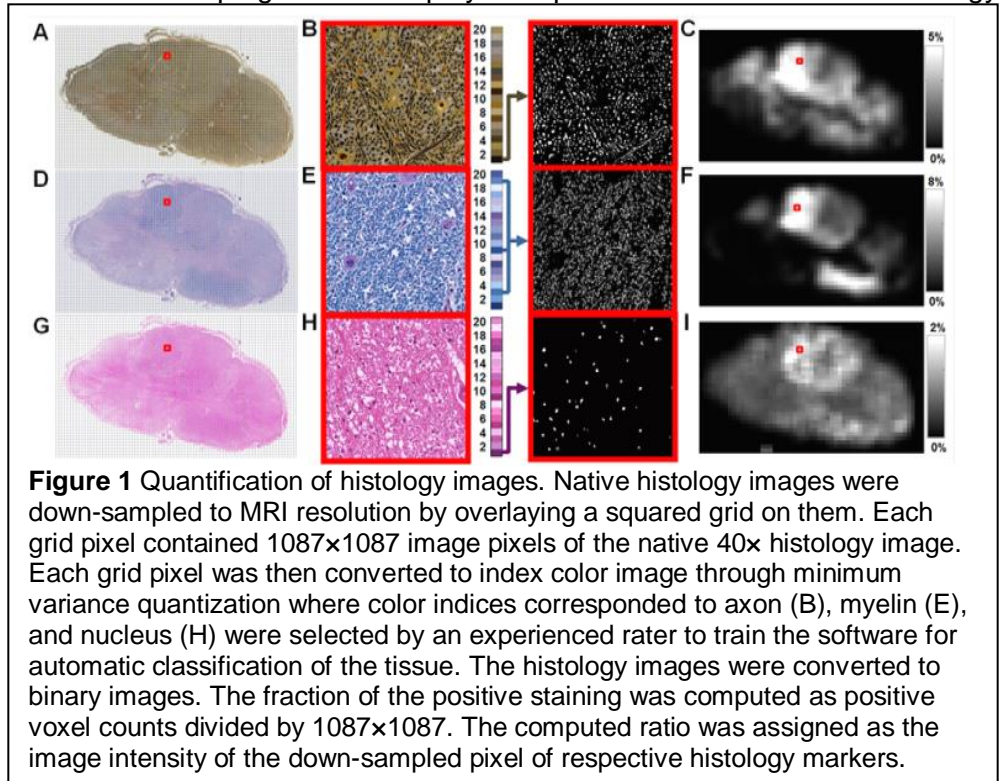
for each type of histologic images were employed. The color indices corresponding to positive staining were selected and consistently applied for all small square histologic image blocks of the same stain type to segment the positive staining regions. The ratio between positive stained pixel number and the total pixel number ($1087 \times 1087 = 1181569$) was calculated as the quantitative measure of positive staining (Fig. 1).

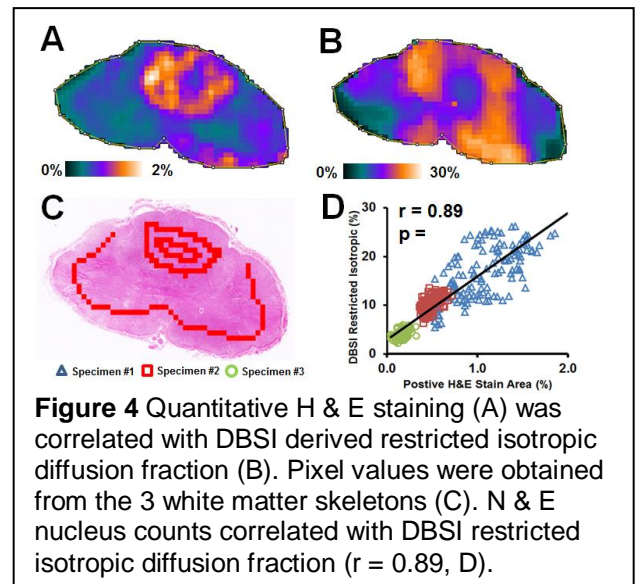
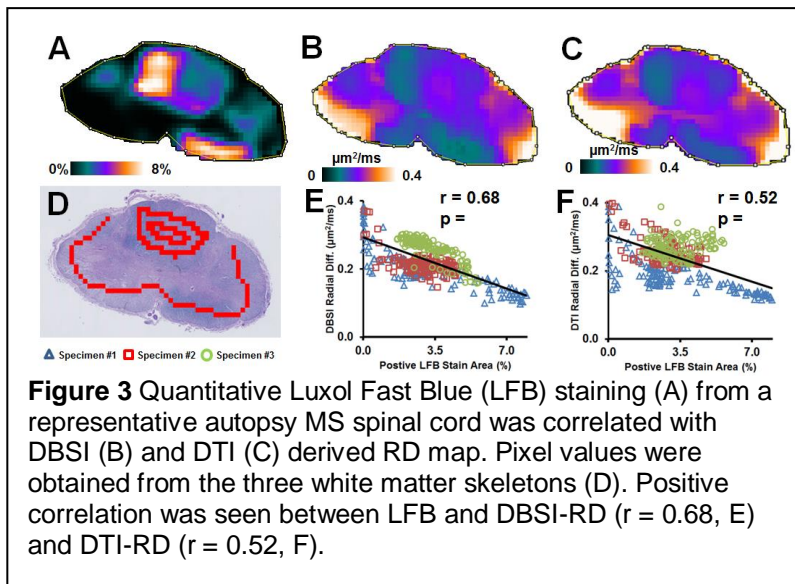
ImageJ (<http://rsbweb.nih.gov/ij/>)

with an in-house developed image registration plugin was employed to conduct the rigid registration between quantitative histology images and DBSI images using a modification of previously described method.¹⁵

Twelve corresponding pairs of landmarks along the perimeter of the cord were manually placed on both quantitative histology images and DBSI indices image to compute the transformation matrix of rigid registration. The computed transformation matrix was then used to convert the quantitative histology image to the orientation of DBSI images. The success of the newly developed

quantification of histology slides can be demonstrated (Figs. 2 – 4).





Cross-sectional DBSI examined mouse brains have been perfusion fixed, sectioned, and stained using Bielschowsky's silver, LFB-PAS, and H& E. High resolution 40 \times images have been captured and are currently being processed for quantification. Although the co-registered images would not be doable since we had to image mice at a different view to improve signal-to-noise ratio (SNR), we will be able to correlate quantitative histology measurements of the entire CC with in vivo DBSI metrics.

3. *In vivo* DBSI of optic nerve at the onset of optic neuritis (ON)

In the previously approved statements of work, year 2 focused on performing tasks related to Aim 2: "Longitudinal DBSI measurements will be performed on the optic nerve from experimental autoimmune encephalomyelitis (EAE) induced by active immunization of C57BL/6 mice using MOG₃₅₋₅₅ peptide at baseline, onset of optic neuritis (assessed by decreased visual acuity), and chronic state of EAE (4 weeks after immunization). Cross sectional DBSI will be performed on the same time points with matched histology validation of DBSI findings. (Months 13 – 26)".

We imaged 10 mice at baseline before immunization. All mice then undergone MOG-EAE induction and daily visual acuity (VA) was performed. At the day when VA ≤ 0.25 cycles/degree mice were imaged and daily VA assessment continued. In this cohort of mice, unilateral ON was seen in every mouse. In vivo DBSI was performed again when the VA of the initially unaffected eye was lower than 0.25 cycles/degree. After the third DBSI examination, all mice were perfusion fixed and optic nerves excised, paraffin-embedded, sectioned, and Immunohistochemical staining performed. Our results show that in vivo DBSI detected underlying inflammation, demyelination, and axonal injury in the optic nerves at the onset of ON (Fig. 5). The corresponding Immunohistochemical staining results were quantitatively analyzed to count the SMI-31 positive axons, MBP positive myelin, and DAPI positive nuclei. Quantitative IHC results were consistent with *in vivo* DBSI findings suggested that acute VA impairment during ON is primarily

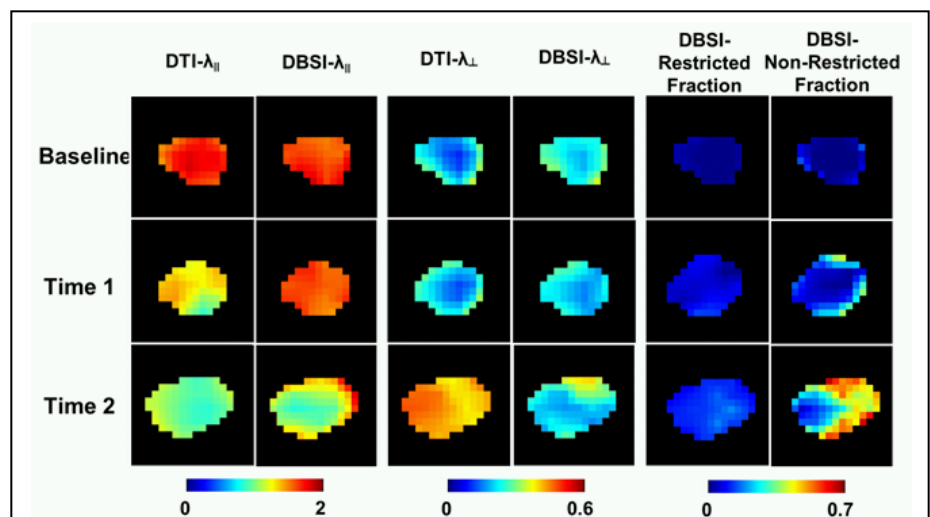


Figure 5 *In vivo* DBSI/DTI pathological metrics time course of an arbitrarily selected optic nerve from a representative mouse before immunization (baseline), at the onset of ON (time 1), and at the subsequent ON onset of the fellow eye (time 2). DTI-AD decreased while DBSI-AD remained relatively unchanged at the onset. DTI-RD significantly increased at time 2 while DBSI-RD only mildly increased. There was not a significant increase in cellularity (restricted diffusion fraction) but significant elevation of edema (non-restricted diffusion fraction) in the optic nerve. Apparently increased cross-section area of optic nerve at time 2 also suggested the presence of inflammation of the optic nerve.

caused by the significantly increased edema resulting from inflammation (Fig. 6). Group-averaged time course of DBSI derived pathological metrics (Fig. 7) suggested that the severity of optic nerve pathologies between eye-1 (earlier ON onset) and eye-2 (later ON onset) was not apparent. This is consistent with the notion that neurological impairments do not reflect the underlying nerve damages in MS.

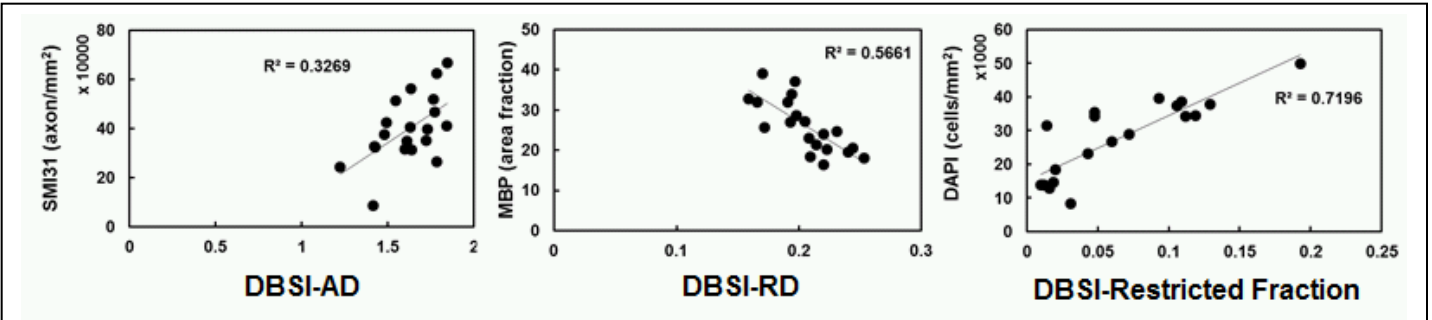


Figure 6 Correlations between quantitative IHC and DBSI-metrics. Results support that DBSI-AD correlated with SMI-31 positive axon counts, DBSI-RD correlated with MBP positive area, and DBSI-restricted isotropic diffusion fraction correlated with DAPI positive nuclear counts.

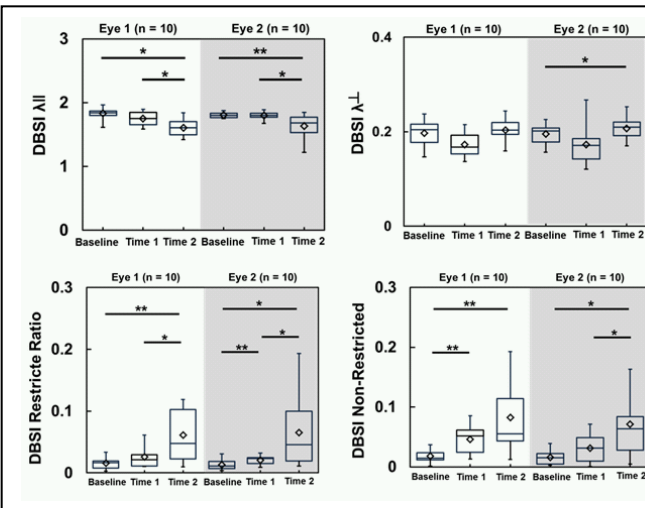


Figure 7 Box-plots of group-averaged DBSI metrics for eye 1(earlier ON onset) and eye 2 (later ON onset) at baseline, time 1 (ON onset of eye 1), and time 2 (ON onset of eye 2) suggested that optic nerve axonal injury and demyelination occurred early in EAE, at the onset of ON. However, the most significant changes resulted from inflammation associated increase in cellularity (DBSI restricted isotropic diffusion fraction) and edema (DBSI non-restricted isotropic diffusion fraction). The timing of ON onset does not seem to be the primary factor of optic nerve damage.

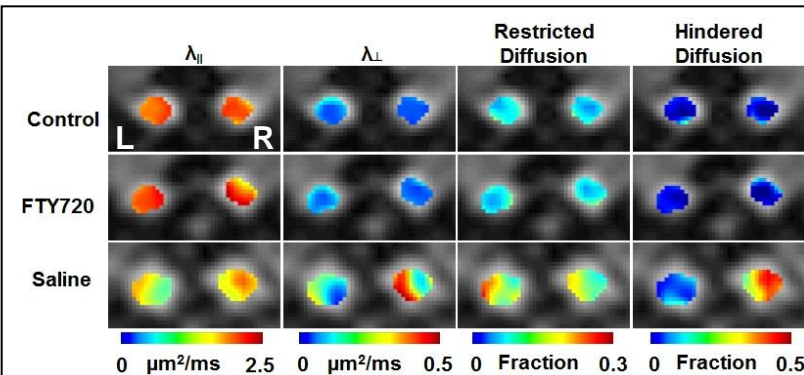


Figure 8 Inflammation and axon/myelin injury were assessed using DBSI derived $\lambda_{||}$, λ_{\perp} , and fractions of restricted (~cellularity) and hindered (~edema) diffusion tensors. Without treatment (saline), optic nerves exhibited heterogeneous inflammation (\uparrow fractions of restricted and hindered diffusion) and axon/myelin damage ($\downarrow \lambda_{||}$ and $\uparrow \lambda_{\perp}$). FTY720 effectively prevented inflammation (normal appearing restricted and hindered diffusion fractions) and axon/myelin injury (normal appearing $\lambda_{||}$ and λ_{\perp}).

4. *In vivo* DBSI may be used to assess treatment efficacy

Preliminary studies were performed where Oral FTY720 (1 mg/kg) or saline was given on the day of immunization to EAE mice ($n = 5$ each group). The onset of ON was defined operationally as $VA \leq 0.25$ c/d. VA was normal in FTY720 treated and naïve control mice. After the VA of saline-treated EAE mice returned to normal for two consecutive days (~2 - 3 weeks after immunization), *in vivo* DBSI was performed on EAE mice accompanied by one randomly chosen animal from the FTY720-treated EAE and naïve control mice (Fig. 8). FTY720 prevented ON, preserved axon/myelin integrity (normalized $\lambda_{||}$ and λ_{\perp}), and prevented inflammation (as evidenced by unchanged fractions of restricted and hindered diffusion, i.e., no increase in cellularity or edema). In the saline-treated EAE mouse shown in Figure 8, for which the right eye remained blind while left eye function appeared normal, the DBSI determined pathologies were heterogeneous within and between optic nerves. The left eye exhibited a more significantly decreased $\lambda_{||}$ and increased cellularity while the right eye showed more increased λ_{\perp} and edema. Overall (individual differences exist, Fig. 8), prophylactic FTY720 did not fully protect axons (non-statistically significant reductions in $\lambda_{||}$ and SMI-31 positive axon counts vs. control)

although it prevented myelin injury (Fig. 9) and suppressed inflammation (normalized fractions of restricted and hindered diffusion and DAPI counts; data not shown). A very preliminary therapeutic FTY720 treatment starting at the onset of ON for 4 weeks suggested that FTY720 did not effectively prevent ON, protect axon/myelin, or suppress inflammation as seen in prophylactic treatment. This strongly supports our experimental design using FTY720 treatments to vary the severity of inflammation and axon/myelin injury to test the sensitivity and specificity of DBSI. All indications so far support DBSI as a versatile outcome measure for assessing drug trials in EAE mice. By combining DBSI assessment of pre-treatment axonal pathologies with FTY720 administration at the onset of the disease axon/myelin preservation efficacy of FTY720 will be elucidated.

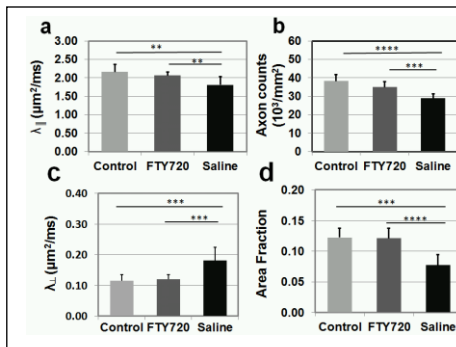


Figure 9 Summary of FTY720 treatments. Statistically significantly decreased $\lambda_{||}$ (a), and increased λ_{\perp} (c) are consistent with decreased SMI-31 positive axon counts (b) and MBP positive area (d) staining was seen in the saline treated EAE optic nerves compared with those of the naïve control. **p < 0.01; *** p < 0.001.

Key Research Accomplishments

1. Developed a novel quantitative analysis approach dealing with histology that is independent of signal intensity threshold allowing the generation of quantitative histology counts in a map mode. Once published, this approach will change the practice of conventional manual counting of histology slides.
2. *In vivo* DBSI was able to reveal previously detected inter-axonal and extracellular space increase using EM in CC from chronic cuprizone fed mice.
3. Correlations between DBSI pathological metrics and quantitative histology findings strongly support the feasibility of the goal of this project. The future validation of DBSI in live human MS would significantly facilitate the development of new therapy by offering a more effective outcome measure.

Conclusion

We have been productive under the current support. However, the proposed aims have not been easy to complete due to many technical developments necessary for the execution of the proposed work. Up to now, we have completed majority of work associated with Aim 1 with the exception of quantitative histological analysis. To this end, a novel objective quantitative analysis approach has been developed and will be applied to all histology slides from the cross-sectional studies. The development itself will result in a publication that will teach fellow researchers in the field changing the labor intensive manual counting of histology slides.

On the longitudinal DBSI examination of optic nerve during the course of ON, we were able to complete one shorter time course (same numbers of scans but all before reaching peak EAE) than planned due to the experience gained from preliminary “practice” to learn the limitation of the proposed plan. We learned that after ON onset and multiple (typically three) *in vivo* DBSI examinations increased and unpredictable mortality of EAE mice at the peak of the disease preventing the completion of a time course extending to chronic stage as initially planned. Thus, we performed a time course study monitoring the onset of ON of both eyes. Mice were perfusion fixed after the 3rd scan without allowing mouse to experience the peak of EAE. The current finding has provided interesting insights on the utility of DBSI and the interrelationship between underlying optic nerve pathologies and visual function. A publication is being prepared based on the preliminary results. Another time course is being planned to only follow the ON course of one eye reducing the number of scans to extend the time course to chronic stage for an opportunity to assess whether acute DBSI is capable of predicting outcome.

Publications

1. Wang X, Cusick MF, Wang Y, Sun P, Libbey JE, Trinkaus K, Fujinami RS, Song SK. Diffusion basis spectrum imaging detects and distinguishes coexisting subclinical inflammation, demyelination and axonal injury in experimental autoimmune encephalomyelitis mice. *NMR Biomed.* 2014 Jul; 27(7):843-52. PubMed PMID: 24816651; PubMed Central PMCID: PMC4071074.
2. Lin TH, Spees WM, Chiang CW, Trinkaus K, Cross AH, Song SK. Diffusion fMRI detects white-matter dysfunction in mice with acute optic neuritis. *Neurobiol Dis.* 2014 Jul; 67:1-8. PubMed PMID: 24632420; PubMed Central PMCID: PMC4035476.
3. Chiang CW, Wang Y, Sun P, Lin TH, Trinkaus K, Cross AH, Song SK. Quantifying white matter tract diffusion

parameters in the presence of increased extra-fiber cellularity and vasogenic edema. *Neuroimage*. 2014 Jul 11; 101C:310-319. PubMed PMID: 25017446.

Inventions, Patents and Licenses

None

Reportable Outcomes

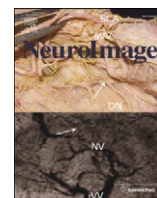
None

Other Achievements

None

References

- 1 Andersen, O. Predicting a window of therapeutic opportunity in multiple sclerosis. *Brain* **133**, 1863-1865, doi:awq182 [pii]10.1093/brain/awq182 (2010).
- 2 Bjartmar, C., Kidd, G., Mork, S., Rudick, R. & Trapp, B. D. Neurological disability correlates with spinal cord axonal loss and reduced N-acetyl aspartate in chronic multiple sclerosis patients. *Ann Neurol* **48**, 893-901 (2000).
- 3 Confavreux, C. & Vukusic, S. Natural history of multiple sclerosis: a unifying concept. *Brain* **129**, 606-616, doi:awl007 [pii]10.1093/brain/awl007 (2006).
- 4 Constantinescu, C. S. & Gran, B. Multiple sclerosis: autoimmune associations in multiple sclerosis. *Nat Rev Neurol* **6**, 591-592, doi:nrneurol.2010.147 [pii]10.1038/nrneurol.2010.147 (2010).
- 5 Conway, D. S. & Cohen, J. A. Multiple sclerosis: Mechanisms of disability accumulation in multiple sclerosis. *Nat Rev Neurol* **6**, 654-655, doi:nrneurol.2010.175 [pii]10.1038/nrneurol.2010.175 (2010).
- 6 Fisniku, L. K. *et al.* Disability and T2 MRI lesions: a 20-year follow-up of patients with relapse onset of multiple sclerosis. *Brain* **131**, 808-817, doi:awm329 [pii]10.1093/brain/awm329 (2008).
- 7 Frischer, J. M. *et al.* The relation between inflammation and neurodegeneration in multiple sclerosis brains. *Brain* **132**, 1175-1189, doi:awp070 [pii]10.1093/brain/awp070 (2009).
- 8 Kutzelnigg, A. *et al.* Cortical demyelination and diffuse white matter injury in multiple sclerosis. *Brain* **128**, 2705-2712, doi:awh641 [pii]10.1093/brain/awh641 (2005).
- 9 Scalfari, A. *et al.* The natural history of multiple sclerosis: a geographically based study 10: relapses and long-term disability. *Brain* **133**, 1914-1929, doi:awq118 [pii]10.1093/brain/awq118 (2010).
- 10 Trapp, B. D. & Nave, K.-A. Multiple Sclerosis: An Immune or Neurodegenerative Disorder? *Annual Review of Neuroscience* **31**, 247-269, doi:doi:10.1146/annurev.neuro.30.051606.094313 (2008).
- 11 Wang, Y. *et al.* Quantification of increased cellularity during inflammatory demyelination. *Brain* **134**, 3587 - 3598 (2011).
- 12 Xie, M. *et al.* Rostrocaudal analysis of corpus callosum demyelination and axon damage across disease stages refines diffusion tensor imaging correlations with pathological features. *J Neuropathol Exp Neurol* **69**, 704-716, doi:10.1097/NEN.0b013e3181e3de90 (2010).
- 13 Deroulers, C. *et al.* Analyzing huge pathology images with open source software. *Diagn Pathol* **8**, doi:Artn 92 Doi 10.1186/1746-1596-8-92 (2013).
- 14 Heckbert, P. S. Color image quantization for frame buffer display. *Computer Graphics* **16**, 7 (1982).
- 15 Budde, M. D., Xie, M., Cross, A. H. & Song, S. K. Axial diffusivity is the primary correlate of axonal injury in the experimental autoimmune encephalomyelitis spinal cord: a quantitative pixelwise analysis. *J Neurosci* **29**, 2805-2813, doi:29/9/2805 [pii]10.1523/JNEUROSCI.4605-08.2009 (2009).



Quantifying white matter tract diffusion parameters in the presence of increased extra-fiber cellularity and vasogenic edema

Chia-Wen Chiang^{a,1}, Yong Wang^{b,f,1}, Peng Sun^b, Tsen-Hsuan Lin^c, Kathryn Trinkaus^d, Anne H. Cross^{e,f}, Sheng-Kwei Song^{b,f,*}

^a Department of Chemistry, Washington University, St. Louis, MO 63130, USA

^b Department of Radiology, Washington University School of Medicine, St. Louis, MO 63110, USA

^c Department of Physics, Washington University, St. Louis, MO 63130, USA

^d Division of Biostatistics, Washington University School of Medicine, St. Louis, MO 63110, USA

^e Department of Neurology, Washington University School of Medicine, St. Louis, MO 63110, USA

^f Hope Center for Neurological Disorders, Washington University School of Medicine, St. Louis, MO 63110, USA

ARTICLE INFO

Article history:

Accepted 27 June 2014

Available online 11 July 2014

Keywords:

Magnetic resonance imaging
Diffusion tensor imaging
Diffusion basis spectrum imaging
Multiple tensor model
Monte-Carlo simulation
White matter injury
Inflammation
Restricted diffusion
Experimental autoimmune encephalomyelitis (EAE)
Immunohistochemistry (IHC)

ABSTRACT

The effect of extra-fiber structural and pathological components confounding diffusion tensor imaging (DTI) computation was quantitatively investigated using data generated by both Monte-Carlo simulations and tissue phantoms. Increased extent of vasogenic edema, by addition of various amount of gel to fixed normal mouse trigeminal nerves or by increasing non-restricted isotropic diffusion tensor components in Monte-Carlo simulations, significantly decreased fractional anisotropy (FA) and increased radial diffusivity, while less significantly increased axial diffusivity derived by DTI. Increased cellularity, mimicked by graded increase of the restricted isotropic diffusion tensor component in Monte-Carlo simulations, significantly decreased FA and axial diffusivity with limited impact on radial diffusivity derived by DTI. The MC simulation and tissue phantom data were also analyzed by the recently developed diffusion basis spectrum imaging (DBSI) to simultaneously distinguish and quantify the axon/myelin integrity and extra-fiber diffusion components. Results showed that increased cellularity or vasogenic edema did not affect the DBSI-derived fiber FA, axial or radial diffusivity. Importantly, the extent of extra-fiber cellularity and edema estimated by DBSI correlated with experimentally added gel and Monte-Carlo simulations. We also examined the feasibility of applying 25-direction diffusion encoding scheme for DBSI analysis on coherent white matter tracts. Results from both phantom experiments and simulations suggested that the 25-direction diffusion scheme provided comparable DBSI estimation of both fiber diffusion parameters and extra-fiber cellularity/edema extent as those by 99-direction scheme. An *in vivo* 25-direction DBSI analysis was performed on experimental autoimmune encephalomyelitis (EAE, an animal model of human multiple sclerosis) optic nerve as an example to examine the validity of derived DBSI parameters with post-imaging immunohistochemistry verification. Results support that *in vivo* DBSI using 25-direction diffusion scheme correctly reflect the underlying axonal injury, demyelination, and inflammation of optic nerves in EAE mice.

© 2014 Elsevier Inc. All rights reserved.

Introduction

Diffusion tensor imaging (DTI) successfully detects axon and myelin injury through decreased axial diffusivity (λ_{\parallel} , parallel to white matter tract) and increased radial diffusivity (λ_{\perp} , perpendicular to white matter tract) in animal models of central nervous system (CNS) diseases and injuries (DeBoy et al., 2007; Kim et al., 2006; Song et al., 2002;

Sun et al., 2006). Although decreased DTI-derived fractional anisotropy (FA) has been demonstrated to reflect myelin damage in multiple sclerosis (MS) (Schmierer et al., 2007), it is not a marker specific to myelin damage since other pathological components may also contribute to diffusion anisotropy change (Assaf et al., 2002; Werring et al., 1999). For example, inflammation associated vasogenic edema has been recognized to increase apparent diffusion coefficient (ADC) and underestimate the DTI-derived FA of fiber tracts (Naismith et al., 2010; Pasternak et al., 2009). Increased cellularity has been demonstrated to decrease DTI-derived ADC (Anderson et al., 2000). However, its impact on diffusion anisotropy remains unclear. An *in vivo* experiment of white matter inflammation in rats has suggested the association of changes in DTI-derived ADC with the evolution of pathology

* Corresponding author at: Biomedical MR Laboratory, Campus Box 8227, Washington University School of Medicine, Room 3221, 4525 Scott Ave, St Louis, MO 63110, USA. Fax: +1 314 362 0526.

E-mail address: ssong@wustl.edu (S.-K. Song).

¹ These authors contributed equally to this work.

(Lodygensky et al., 2010). It is clear that both axon/myelin and extra-fiber pathological changes can impact DTI-derived metrics.

DTI assumes that diffusion of water molecules in the CNS white matter follows mono-exponential diffusion weighted signal decay (typically at b -value < 1000 s/mm²), and was modeled by a single anisotropic tensor. Thus, diffusion anisotropy of white matter tracts in the presence of multiple structural and pathological compartments poses significant challenges in DTI analysis of white matter tracts since non-Gaussian models or multiple diffusion tensors are needed to reflect the tissue and pathological complexity. Various diffusion techniques have been proposed to overcome the limitation of DTI by non-Gaussian modeling of both parametric (model-based) or non-parametric (model-free) approaches. For instance, diffusion spectrum imaging (DSI) resolves crossing or branching fibers by direct evaluation of diffusion displacement probability density function which is the inverse Fourier transform of the diffusion weighted signals, but typically requires a large number of measurements with extensive diffusion weighting (Wedeen et al., 2005); diffusion kurtosis imaging (DKI) quantifies the non-Gaussian diffusion by estimating apparent diffusion kurtosis of diffusion displacement probability distribution (Jensen et al., 2005); generalized diffusion tensor imaging (gDTI) models the white matter tract via higher order tensors (Liu et al., 2004); composite hindered and restricted model of diffusion (CHARMED) evaluates an extra-cellular compartment (assigned to hindered diffusion resulting from extra-axonal diffusion weighted signal) and intra-cellular compartments (assigned to restricted diffusion in a cylinder representing individual intra-axonal space) employing a comprehensive diffusion weighting scheme (Assaf and Basser, 2005). Recently, Scherrer et al. proposed multiple fascicle models (MFM) to model an isotropic compartment (assigned to free water diffusion) and multiple anisotropic compartments (assigned to single fascicle) using a cube and sphere (CUSP) acquisition scheme (Scherrer and Warfield, 2012). Zhang et al. proposed neurite orientation dispersion and density imaging (NODDI) to model tissue components. Using high-angular-resolution diffusion imaging (HARDI) acquisition scheme, NODDI assesses intra-cellular (assigned to space within neurites), extra-cellular (assigned to space around the neurites but occupied by glial cells), and CSF compartments for deriving neurite density and orientation dispersion (Zhang et al., 2012). Although these approaches resolve possible fiber orientations and free water diffusion contaminations confounding DTI in the CNS, the restricted water diffusion outside fiber tracts affecting DTI measurements was less commonly dealt with. Glial cells have been modeled as a highly restricted isotropic component in an analytical model (Stanisz et al., 1997). A four-tensor model was proposed to include the restricted isotropic diffusion resulting from cell and the extracellular water components (Alexander et al., 2010), and most recently, restricted isotropic diffusion component has been included as one type of isotropic restricted compartment model in a taxonomy comparison study (Panagiotaki et al., 2012).

The recently-developed diffusion basis spectrum imaging (DBSI) approach models white matter diffusion as the linear combination of multiple discrete anisotropic diffusion tensors describing axonal tracts and a spectrum of isotropic diffusion tensors describing restricted (reflecting cells), and non-restricted (reflecting extra-axonal and extracellular space) diffusion components outside of axonal tracts (Wang et al., 2011). Employing a 99-direction diffusion-encoding scheme, DBSI has shown promise to accurately detect and quantify crossing fibers, axonal injury, demyelination, and inflammation-associated cell infiltration and edema in both *ex vivo* phantom and *in vivo* mouse brain. Although the effect of increased cell infiltration and edema on DTI-derived indices has been demonstrated previously using cuprizone treated mouse model and mouse trigeminal nerve phantoms (Wang et al., 2011), a more comprehensive study was needed to investigate the effect of increased cellularity and vasogenic edema associated with inflammation. In this study, diffusion weighted signals derived from Monte-Carlo simulations and acquired from tissue phantoms of fixed mouse trigeminal nerve and 2% agar gel were employed to demonstrate how cellularity

and edema change DTI indices. The accuracy of DBSI to resolve the complication of inflammation was also examined. To image the coherent white matter tracts without fiber crossing, such as optic nerve and spinal cord, a simplified DBSI with one anisotropic diffusion tensor component and a spectrum of isotropic diffusion tensors would be sufficient requiring less diffusion encoding directions. A reduced scanning time can be achieved by significantly reducing the number of diffusion weighted images. Thus, we adopted a 25-direction diffusion encoding scheme (Batchelor et al., 2003) on both fixed tissue phantoms and Monte-Carlo (MC) simulation. Comparisons between 25- and 99-direction DBSI results on both experimental tissue phantom and simulated data were conducted to examine the accuracy of DBSI analysis using the 25-direction diffusion encoding scheme. To further demonstrate the feasibility of the 25-direction scheme for DBSI analysis, *in vivo* DBSI was performed on a group of experimental autoimmune encephalomyelitis (EAE) affected mice at the onset of optic neuritis comparing with the age and gender matched sham control mice. The *in vivo* diffusion MRI data were analyzed using DBSI and verified by post-imaging immunohistochemistry.

Materials and methods

Diffusion-encoding schemes

Both 99- (Wang et al., 2011) and 25-direction (Batchelor et al., 2003) diffusion-encoding schemes were employed for DBSI analysis in this study. The 99 diffusion-encoding directions were selected as prescribed in diffusion spectrum imaging (DSI) where the position vectors are the entire grid points (q_x, q_y, q_z) over the 3-D q -space under the relationship that $(q_x^2 + q_y^2 + q_z^2) \leq r^2$, where $r = 3$ for DBSI (Kuo et al., 2008; Wang et al., 2011; Wedeen et al., 2005). The icosahedral 25-direction sampling scheme was as prescribed by Batchelor et al. with the addition of one extra non-diffusion ($b = 0$) weighted image. See Appendix A and B for the 99- and 25-direction diffusion-encoding schemes.

Fixed trigeminal nerve phantom

Trigeminal nerves (~4 mm long) were dissected from adult female normal C57BL/6 mice (The Jackson Laboratory, Bar Harbor, ME) after perfusion fixation with 4% paraformaldehyde in 0.01 M phosphate buffered saline (PBS) followed by immersion fixation for 24 h and kept in 0.01 M PBS solution at 4 °C. Twenty trigeminal nerves were employed to generate phantoms of a single trigeminal nerve only ($n = 7$) and a single nerve juxtaposed with different amount of 2% aqueous agar gel to mimic vasogenic edema ($n = 13$). All phantoms were prepared with a nerve gently blotted using Kimwipes® tissue to remove extra solution. Nerves were placed on a microscope slide with an identifier, with or without agar gel, covering with plastic wrap to avoid dehydration.

Diffusion-weighted spectroscopy of fixed trigeminal nerve phantom

Diffusion-weighted data were collected immediately after nerve phantom preparation using a 6-mm inner diameter single-turn surface coil. Diffusion-weighted spin-echo spectroscopy was performed with the following acquisition parameters: repetition time (TR), 2 s; echo time (TE), 32 ms; time between application of gradient pulses (Δ), 16 ms; gradient pulse duration (δ), 8 ms; number of average, 1; the maximum diffusion-weighting factor (b -value), 3200 s/mm² for both 99- and 25-direction diffusion weighting schemes at a single setting. Total acquisition time was 4 min 15 s.

Monte-Carlo simulation

Monte-Carlo simulations were performed to evaluate the effect of vasogenic edema and cellularity on DTI and DBSI indices in a computer generated geometric model, mimicking the trigeminal nerve tissue

phantoms. The simulation was performed by allowing water molecules (2.5×10^5 , randomly distributed) to undergo random walk within a $90\text{-}\mu\text{m}$ diameter sphere (light blue, Fig. 1A) at 20°C . Diffusivity for free water was set to be $2.02\text{ }\mu\text{m}^2/\text{ms}$ (at 20°C). The time-step for simulated random walk was 0.2 ms . The computer generated model of the trigeminal nerve phantom for simulation were composed of (1) a coherent axon fiber bundle modeled by uniformly oriented, and tightly packed cylindrical tubes (green cylinders in Fig. 1A) with a diameter of $2\text{ }\mu\text{m}$; (2) cellular components modeled as isotropic spheres (blue in Fig. 1A) with a diameter of $6\text{ }\mu\text{m}$ randomly placed surrounding the axonal fiber bundle; (3) extra-axonal and extracellular space occupied by water molecules distributed outside of axonal bundle and cellular components (Fig. 1A). The size of axonal cylinder and cells was adapted according to literature reports (Stanisz et al., 1997; Stolzenburg et al., 1989). The imaging voxel ($50 \times 50 \times 50\text{ }\mu\text{m}^3$, pink cube in Fig. 1A) was placed in the center of the sphere defined for random walk (light blue outer sphere in Fig. 1A). At the boundary of axon and cell components, the water spin reflected elastically (Liu et al., 2004). During the simulation, water spins were allowed to walk in or out of the imaging voxel without constraints to reflect the real physical condition (Liu et al., 2004). The boundaries of the axon and cell components were assumed to be impermeable. The random walk trajectory of each water spin was recorded and saved during the simulation.

Based on previous fixed mouse trigeminal nerve phantom study (Wang et al., 2011), baseline simulation model (model # 1, Fig. 1B), mimicking nerve only mouse trigeminal nerve without added gel, consisted of 12% cells (133 spheres), 68% axonal fibers (529 cylinders), and 20% extra-axonal/extracellular space. The tissue phantom of single nerve plus gel was simulated by increasing the size of imaging voxel of baseline simulation model (model # 1, Fig. 1B), thereby increasing the extra-axonal/extracellular space (model # 2–11, Fig. 1B), to mimic vasogenic edema. In model # 2–11, the cell fraction ranged from 7% to 15%, the axonal fiber fraction ranged from 15% to 57%, and the extra-axonal/extracellular space fraction ranged from 27% to 78% (Fig. 1B). It is very challenging if at all possible to control the amount of cellular components in the experimental trigeminal nerve tissue phantom. However, the cellular components can be readily adjusted and simulated by increasing the number of spheres (cells) inside the simulated imaging voxel. In model # 12–21, the cell volume fraction ranged from 14% to 80%, the axonal fiber fraction ranged from 12% to 63%, and the extra-axonal/extracellular space fraction ranged from 8% to 22%.

A simple spin echo sequence with diffusion gradients was implemented to simulate the diffusion weighted MRI signals from the simulated imaging voxel. The simulated phase of each water spin within TE was calculated based on the random walk trajectory (Liu et al., 2004). The overall measured diffusion MRI signal was simulated as the summation of signals contributed from all water spins, ending within the voxel of imaging at the time of TE. The effects of T1 and T2 decay for all spin trajectories were neglected (Liu et al., 2004). Both 99- and 25-direction schemes were employed to acquire the diffusion weighted signals. Other key MRI acquisition parameters included TE 32 ms, Δ 16 ms, δ 8 ms, maximum b-value 3200 s/mm^2 were kept the same intentionally with the fixed trigeminal nerve phantom experiment above. Rician noise was added to the simulated diffusion weighted signals from model # 12 mimicking mild cell infiltration (Fig. 1B) to examine the effect of signal-to-noise ratio (SNR) on DBSI-derived indices obtained using 25-direction diffusion scheme at SNR = 10, 20, 30, 40, and 100 of the non-diffusion weighted signal. The simulation was repeated 20 times for each SNR level.

Acute optic neuritis of EAE

Five adult female 8-week-old C57BL/6 mice (The Jackson Laboratory, Bar Harbor, ME, USA) were immunized using $50\text{ }\mu\text{g}$ myelin oligodendrocyte glycoprotein peptide (MOG_{35–55}) emulsified in incomplete Freund's adjuvant with $50\text{ }\mu\text{g}$ *Mycobacterium tuberculosis*. Five age-matched female mice received only incomplete Freund's adjuvant and *Mycobacterium tuberculosis* in the absence of MOG_{35–55} served as the sham control. For EAE-immunized mice, the adjuvant pertussis toxin (300 ng; PTX, List Laboratories, Campbell, CA) was injected intravenously on the day of immunization and two days later. Transverse view of mouse optic nerve was imaged at the onset of acute EAE optic neuritis (Chiang et al., 2011). Matched sham control mice were randomly selected for *in vivo* DBSI acquisition whenever an EAE mouse was imaged.

In vivo magnetic resonance imaging

In vivo diffusion MRI experiments were performed on a 4.7 T Agilent DirectDrive™ small-animal MRI system (Agilent Technologies, Santa Clara, CA) equipped with Magnex/Agilent HD imaging gradient coil (Magnex/Agilent, Oxford, UK) with pulse gradient strength up to 58 G/cm and a gradient rise time $\leq 295\text{ }\mu\text{s}$. After anesthetized using 1%

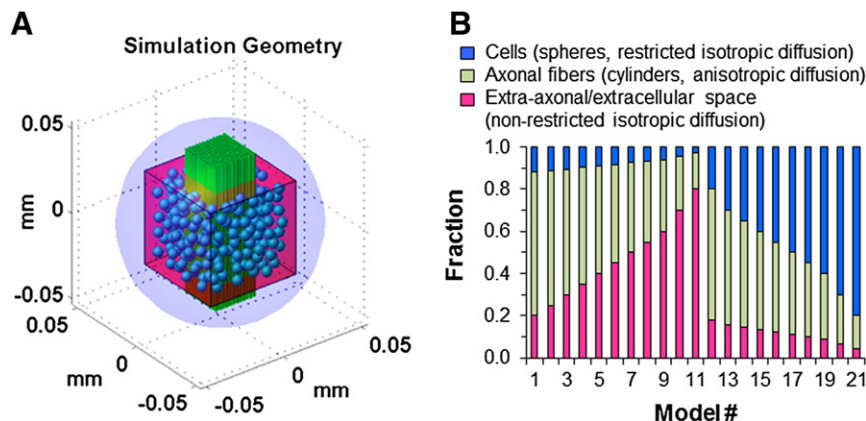


Fig. 1. (A) A three-dimensional computer-synthesized trigeminal nerve model was constructed for Monte-Carlo simulations. The coherently oriented axonal fiber bundle was composed of tightly packed cylinders of $2\text{-}\mu\text{m}$ diameter (green cylinders), to be described by anisotropic water diffusion components. Cells were represented by spheres of $6\text{-}\mu\text{m}$ diameter (blue spheres) randomly placed surrounding the fiber bundle for simulating restricted isotropic water diffusion in cells. Extra-axonal/extracellular space was represented as non-restricted isotropic diffusion within an imaging voxel. Voxel of interest ($50 \times 50 \times 50\text{ }\mu\text{m}^3$ pink cube) was placed in the center of the simulation space for the random walk of water molecules (light blue outer sphere of $90\text{-}\mu\text{m}$ diameter). (B) Baseline trigeminal nerve model (model # 1) consisted of intra- and extra-axonal water diffusion closely associated with axonal fibers (anisotropic diffusion; green bar), cells (restricted isotropic diffusion; blue bar) and extra-axonal/extracellular space (non-restricted isotropic diffusion; pink bar). Similar to the fixed normal trigeminal nerve phantoms with different amount of gel, by gradually increasing the size of imaging voxel, a set of baseline trigeminal nerve model with varying fractions of non-restricted isotropic diffusion (model # 2–11) was used to assess the impact of edema on DTI and DBSI measurements. By increasing the number of spheres, i.e., restricted isotropic diffusion components (model # 12–21), the impact of increased cellularity on DTI and DBSI was also assessed.

isoflurane/oxygen, mice were placed in a custom-made head holder. The rate of respiration and rectal temperature, at 37 °C, was monitored and controlled by a small animal physiological monitoring and control unit (SAIL Inc., NY). An actively-decoupled volume (transmit)/surface (receive) coil pair was used for MR excitation and signal reception. All image slices were acquired based on previously reported procedures (Sun et al., 2008) to plan for the final-targeted slice showing a transverse view of mouse brain with two optic nerves, as nearly as orthogonal to image slice as possible. A multi-echo spin-echo diffusion-weighted sequence (Tu et al., 2010) and a 25-direction diffusion-encoding scheme combined with one $b = 0$ were employed and MR acquisition parameters were TR 1.5 s, TE 37 ms, Δ 18 ms, δ 6 ms, max. b -value 2200 s/mm², slice thickness 0.8 mm, and in-plane resolution 117 $\mu\text{m} \times 117 \mu\text{m}$ (before zero-filled). The total acquisition was approximately 2 h, 20 min.

Immunohistochemistry

Mice were perfusion fixed with 0.01 M phosphate-buffered saline (PBS, pH = 7.4) followed by 4% paraformaldehyde in 0.01 M PBS immediately after imaging. Brains were excised and fixed for 24 h, and then transferred to 0.01 M PBS for storage at 4 °C until histological analysis. Fixed optic nerves were embedded in 2% agar blocks (Blewitt et al., 1982) before being embedded in paraffin. Five- μm thick transverse slices were sectioned, deparaffinized, rehydrated, and blocked using a 1:1 mixture of 10% normal goat serum and 2% bovine serum albumin in PBS for 20 min at room temperature to prevent nonspecific binding of goat secondary antibody. Sections were incubated in monoclonal anti-phosphorylated neurofilament primary antibody (SMI-31; 1:1000, Covance, US) to stain non-injured axons, and in rabbit anti-myelin basic protein (MBP) primary antibody (1:1000, Sigma Inc., MO) to stain myelin sheath at 4 °C overnight. After several rinses, secondary goat anti-mouse IgG and goat anti-rabbit IgG conjugated Alexa 488 (1:800, Invitrogen) were applied, respectively, to visualize immunoreactivity of materials at room temperature for 1 h. After washing, slides were covered using Vectashield Mounting Medium with 4',6-diamidino-2-phenylindole (DAPI) (Vector Laboratory, Inc., Burlingame, CA). Histological images were acquired at 20 \times and 60 \times (water objective) magnifications on Nikon Eclipse 80i fluorescence microscope using MetaMorph software (Universal Imaging Corporation, Sunnyvale, CA).

Data analysis

Experimental and simulated data obtained using 99- and 25-direction diffusion encoding schemes were examined by DBSI multi-tensor model analysis package developed in-house with Matlab® (MathWorks) (Wang et al., 2011) and conventional DTI single-tensor model analysis. Briefly, Eq. (1) was first solved by fitting total number k diffusion signals using a linear combination of diffusion basis sets consisting of cylindrically symmetric diffusion tensors with the freedom to vary λ_{\parallel} and λ_{\perp} to estimate the number of anisotropic diffusion tensor components (N_{Aniso}) and the associated principal directions. After N_{Aniso} was computed, isotropic diffusion tensor components were further analyzed using nonnegative least-squares (NNLS) technique. For coherent white matter tract in this study, $N_{\text{Aniso}} = 1$. The global nonlinear optimization was conducted employing direct pattern search to solve Eq. (1). S_k is the k th measured diffusion weighted signals ($k = 1, 2, \dots, 99$; or 25 in this study). f_i and $f(D)$ are signal intensity fractions of i th anisotropic diffusion components and a spectrum of isotropic diffusion components from a to b (diffusivity, typically from 0 to 3 $\mu\text{m}^2/\text{ms}$), respectively.

$$S_k = \sum_{i=1}^{N_{\text{Aniso}}} f_i e^{-|\vec{b}_k| \lambda_{\perp i}} e^{-|\vec{b}_k| (\lambda_{\parallel i} - \lambda_{\perp i}) \cos^2 \psi_{ik}} + \int_a^b f(D) e^{-|\vec{b}_k| D} dD \quad (k = 1, 2, 3, \dots) \quad (1)$$

To the first approximation, the intracellular water may be modeled as restricted isotropic diffusion due to the hindrance of cell membranes and sub-cellular structures. Based on our previous experimental findings, the restricted isotropic diffusion fraction reflecting cellularity is derived by the summation of $f(D)$ at $0 \leq \text{ADC} \leq 0.3 \mu\text{m}^2/\text{ms}$. The summation of the remaining $f(D)$ at $3 > \text{ADC} > 0.3 \mu\text{m}^2/\text{ms}$ was assigned to non-restricted isotropic diffusion reflecting vasogenic edema and CSF water.

Statistical analysis

All data were expressed as mean \pm standard deviation or median and interquartile range (IQR). The comparison between DTI and DBSI derived diffusion parameters was performed on data obtained from trigeminal nerve phantoms and from Monte-Carlo simulations using t-tests or linear regression models with repeated measures where more than one observation per subject was included. A nonparametric Wilcoxon signed rank test has been performed to test equivalence of 99- and 25-direction DBSI-derived parameters including λ_{\parallel} , λ_{\perp} , and FA, as well as the fractions of different diffusion tensor components. Nonparametric Spearman's rank correlations were used to compare DBSI/DTI and IHC. The tests were repeated for data from all simulation models, i.e., changing proportion of extra-axonal/extracellular space and for those with a changing proportion of cells. All statistical analyses were performed using SAS V9.3 (SAS Inc., Cary, NC).

Results

Effect of vasogenic edema on DTI/DBSI-derived parameters

For 99-direction diffusion weighted data (SNR = 40) from fixed trigeminal nerve only phantoms ($N = 7$), DTI derived $\lambda_{\parallel} = 0.77 \pm 0.05 \mu\text{m}^2/\text{ms}$, $\lambda_{\perp} = 0.18 \pm 0.02 \mu\text{m}^2/\text{ms}$, and FA = 0.72 ± 0.04 were compared with those derived using DBSI where $\lambda_{\parallel} = 1.09 \pm 0.06 \mu\text{m}^2/\text{ms}$, $\lambda_{\perp} = 0.15 \pm 0.02 \mu\text{m}^2/\text{ms}$, and FA = 0.84 ± 0.02 ($n = 7$, mean \pm standard deviation). DBSI estimated axonal fiber fraction to be $67 \pm 3\%$, cellularity to be $14 \pm 2\%$, and extra-axonal/extracellular space to be $20 \pm 3\%$ of the total signal intensity. This finding explains the difference of axial diffusivities derived by DTI and DBSI, and is consistent with our previously published results supported by immunohistochemistry (Wang et al., 2011). With the addition of 2% agar gel, DTI derived λ_{\perp} or FA was significantly affected while DBSI derived parameters remained unchanged (Fig. 2A). A comparable observation was seen in MC simulation data where DTI derived FA decreased while λ_{\parallel} , λ_{\perp} increased with increasing vasogenic edema (i.e., extra-axonal/extracellular space, non-restricted isotropic diffusion component; Fig. 2B) with relatively stable DBSI derived FA, λ_{\parallel} , and λ_{\perp} .

Effect of increased cellularity on DTI/DBSI-derived parameters

Since cellularity is difficult to change experimentally using the fixed nerve, MC simulation was performed with various extents of extra-fiber cells (i.e., spheres, restricted isotropic diffusion component) to mimic cellularity changes. Diffusion parameters derived by DTI were significantly affected with increasing cellularity, i.e., DTI derived λ_{\parallel} , and FA significantly decreased with increasing cellularity while DBSI derived parameters were largely unaffected (Fig. 3). DTI derived λ_{\perp} was minimally affected in contrast to the more profound changes seen in λ_{\parallel} .

Close correspondence between 25- and 99-direction DBSI-derived parameters

There was no discernible difference between 25- vs. 99-direction diffusion encoding scheme in DBSI derived diffusion parameters on data

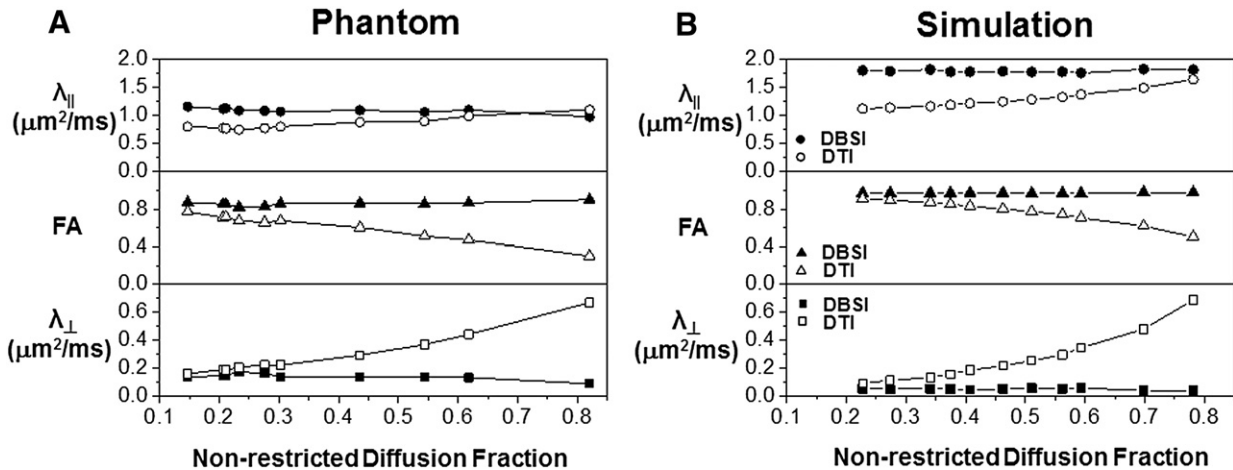


Fig. 2. The impact of various extents of vasogenic edema (or tissue loss) on DTI (open symbols) and DBSI (filled symbols) measurements was mimicked experimentally by adding various amount of 2% agar gel to the fixed normal trigeminal nerve (A) or by increasing the extent, i.e., by enlarging the voxel size without changing the cell or axon bundle content, of non-restricted diffusion component in the Monte-Carlo simulation (B). Experimentally (A), increased gel content resulted in overestimating DTI derived $\lambda_{||}$ and λ_{\perp} (comparing with the nerve only phantom) while underestimating FA (open symbols). The DBSI derived diffusion parameters were not affected by varying the content of the gel (filled symbols). On the data generated using Monte-Carlo simulation (B), increasing non-restricted diffusion components also resulted in overestimating DTI derived $\lambda_{||}$ and λ_{\perp} while underestimating the FA (open symbols). The DBSI derived diffusion parameters (filled symbols) were not affected by increasing non-restricted diffusion component.

generated using Monte-Carlo simulation (25-dir vs. 99-dir): axial diffusivity ($1.80 \pm 0.03 \mu\text{m}^2/\text{ms}$ vs. $1.81 \pm 0.05 \mu\text{m}^2/\text{ms}$), radial diffusivity ($0.05 \pm 0.01 \mu\text{m}^2/\text{ms}$ vs. $0.04 \pm 0.01 \mu\text{m}^2/\text{ms}$) and FA (0.96 ± 0.01 vs. $0.97 \pm 0.01 \mu\text{m}^2/\text{ms}$). DBSI derived non-restricted and restricted isotropic diffusion fractions using 25- and 99-direction diffusion schemes (Figs. 4A and B) were not different from the true values for the simulation.

Effects of noise on 25-direction DBSI-derived parameters

MC simulation of 25-direction diffusion weighted data with SNR of non-diffusion weighted image at 10, 20, 30, 40 and 100 was performed on a mild cell infiltration model (model # 12). The noise affected the bias and precision of the 25-direction DBSI-derived axial diffusivity (Fig. 5A), radial diffusivity (Fig. 5B), restricted isotropic diffusion tensor fraction (Fig. 5C), and non-restricted isotropic diffusion

tensor fraction (Fig. 5D). At SNR = 100, DBSI axial diffusivity, radial diffusivity, restricted isotropic diffusion and non-restricted isotropic diffusion fractions were all estimated with high precision indicated by a small interquartile range and absence of outliers (Fig. 5). With decreasing SNR, both bias and precision worsened (Fig. 5). At the SNR range readily achieved on typical animal and clinical scanner (SNR = 20–40), 25-direction DBSI-derived axial diffusivity was well-estimated (i.e., falls within the middle half of values at SNR = 100) at SNR ≥ 30 while slightly underestimated at SNR = 20 (Fig. 5A); DBSI-radial diffusivity was well-estimated at SNR ≥ 20 (Fig. 5B); the restricted diffusion fraction was well-estimated at SNR ≥ 40 while overestimated at SNR ≤ 30 (Fig. 5C); and non-restricted diffusion fraction was well-estimated at SNR ≥ 30 while underestimated at SNR = 20 (Fig. 5D).

In vivo DBSI of EAE mice at the onset of optic neuritis

A close examination of the 25-direction DTI and DBSI parameter maps of the representative sham (Figs. 6A–F) and EAE-affected (Figs. 6a–f) mice suggested the presence of axonal injury revealed by the decreased $\lambda_{||}$ derived by both DTI (Fig. 6a) and DBSI (Fig. 6b), and demyelination indicated by the increased λ_{\perp} derived by DTI (Fig. 6c) and DBSI (Fig. 6d), and inflammation implicated by the increased restricted (Fig. 6e) and non-restricted (Fig. 6f) isotropic diffusion fraction in the EAE-affected optic nerve. All diffusion MRI detected pathologies in the EAE optic nerve exhibited a heterogeneous distribution in the cross-section of the nerve (Figs. 6a–f). Apparent heterogeneity of cell infiltration was also seen, consistent with a heterogeneous increase in DAPI-positive cell nuclei staining (Figs. 6K and k). Qualitatively, axonal injury (decreased $\lambda_{||}$) and demyelination (increased λ_{\perp}) occurred within the regions where increased cellularity (increased restricted isotropic diffusion fraction) was present (Figs. 6b, d, and e).

Results from quantitative analyses showed significantly decreased $\lambda_{||}$ and increased λ_{\perp} (mean \pm standard deviation; EAE vs. Sham) in both DBSI and DTI: DBSI $\lambda_{||} = 1.73 \pm 0.22$ vs. $2.10 \pm 0.04 \mu\text{m}^2/\text{ms}$ ($p = 0.020$); DTI $\lambda_{||} = 1.34 \pm 0.37$ vs. $1.89 \pm 0.09 \mu\text{m}^2/\text{ms}$ ($p = 0.028$); DBSI $\lambda_{\perp} = 0.15 \pm 0.03$ vs. $0.11 \pm 0.01 \mu\text{m}^2/\text{ms}$ ($p = 0.047$); and DTI $\lambda_{\perp} = 0.21 \pm 0.04$ vs. $0.11 \pm 0.01 \mu\text{m}^2/\text{ms}$ ($p = 0.0046$). DBSI derived restricted isotropic diffusion fraction (i.e., the putative cellularity) in EAE optic nerves was significantly higher than that of the control (0.10 ± 0.09 vs. 0.03 ± 0.01 , $p = 0.022$). The non-restricted isotropic

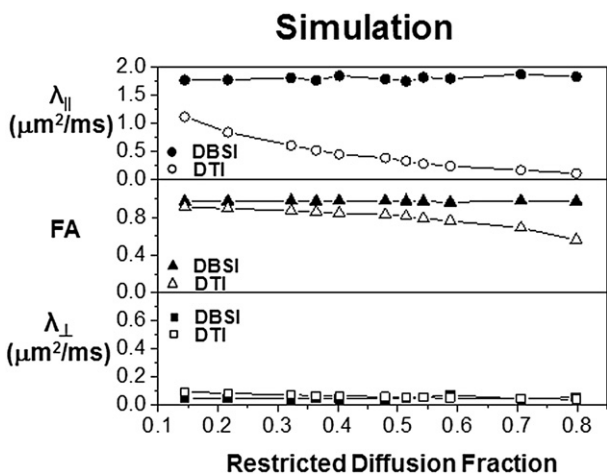


Fig. 3. Due to the difficulty in making reliable experimental phantoms with varying cell contents, Monte-Carlo simulations with varying extents of the restricted diffusion component were performed to mimic the inflammation associated cellularity increase. Increased content of restricted diffusion component significantly underestimated the DTI derived $\lambda_{||}$ and FA without an impact on λ_{\perp} . None of the DBSI derived diffusion parameters was affected by the increased restricted diffusion component.

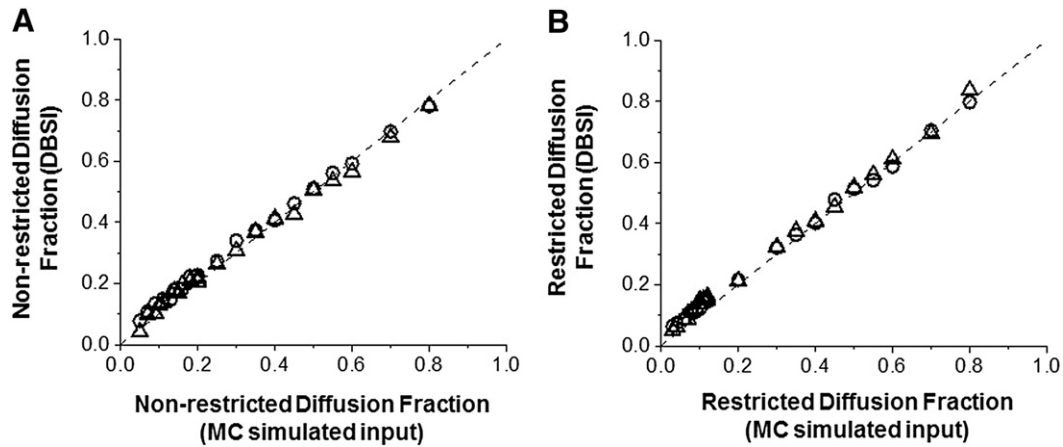


Fig. 4. DBSI derived non-restricted (A) and restricted isotropic diffusion fraction (B) using 99- (circle) and 25-direction (triangle) diffusion encoding scheme was compared with the input values used for Monte-Carlo simulations. Data obtained from both diffusion encoding schemes fall on the line of identity (black dashed lines in A and B) suggesting that DBSI analysis can be accurately performed using 25-direction encoding scheme in situations where fiber crossing is not of concern.

diffusion fraction (i.e., the putative vasogenic edema) was also significantly higher in EAE optic nerves than that of the control (0.15 ± 0.03 vs. 0.03 ± 0.01 , $p < 0.0001$). The increased sum of restricted and non-restricted isotropic diffusion fractions may be a good indicator of inflammation, 0.24 ± 0.12 vs. 0.06 ± 0.02 (EAE vs. Sham, $p = 0.024$).

Quantitative immunohistochemical analyses revealed that DTI/DBSI detected axonal injury and demyelination was also seen in SMI-31-positive axon counts ($5.3 \times 10^5 \pm 1.8 \times 10^5$ vs. $7.4 \times 10^5 \pm 0.2 \times 10^5$ counts/mm²; $p = 0.03$; Figs. 7 A and C) and MBP-positive staining area ($37\% \pm 5\%$ vs. $45\% \pm 3\%$; $p = 0.01$) exhibiting statistically

significant correlations (Figs. 7B and D). The DAPI-positive nuclear counts increased in EAE optic nerves ($6.6 \times 10^3 \pm 5.0 \times 10^3$ vs. $3.5 \times 10^3 \pm 0.7 \times 10^3$ counts/mm²) without reaching a statistical significance ($p = 0.2$). DAPI-positive nuclear counts correlated with DBSI estimated cellularity ($r = 0.65$, $p = 0.042$; Fig. 7E).

Discussion

This study investigated the effect of increased cellularity and vasogenic edema, commonly seen in CNS injuries, on the DTI derived

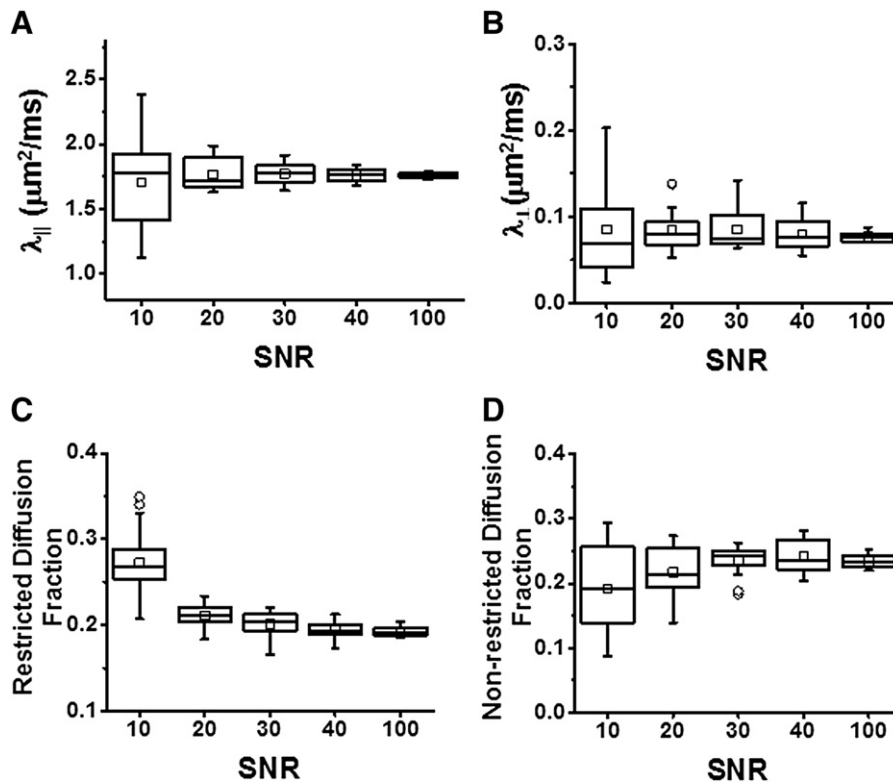


Fig. 5. Monte-Carlo simulation of 25-direction diffusion weighted data with SNR of non-diffusion weighted image at 10, 20, 30, 40 and 100 was performed on a mild cell infiltration model (model # 12). The noise affected the bias and precision of the 25-direction DBSI-derived axial diffusivity (A), radial diffusivity (B), restricted isotropic diffusion tensor fraction (C), and non-restricted isotropic diffusion tensor fraction (D). At SNR = 100, DBSI axial diffusivity, radial diffusivity, restricted isotropic diffusion and non-restricted isotropic diffusion fractions were all estimated with high precision indicated by a small interquartile range and absence of outliers. With decreasing SNR, both bias and precision worsened. At SNR = 40, achieved on the current *in vivo* DBSI examinations of EAE and sham control mice, DBSI-derived $\lambda_{||}$ (A), λ_{\perp} (B), restricted (C), and non-restricted (D) diffusion fraction were all well-estimated.

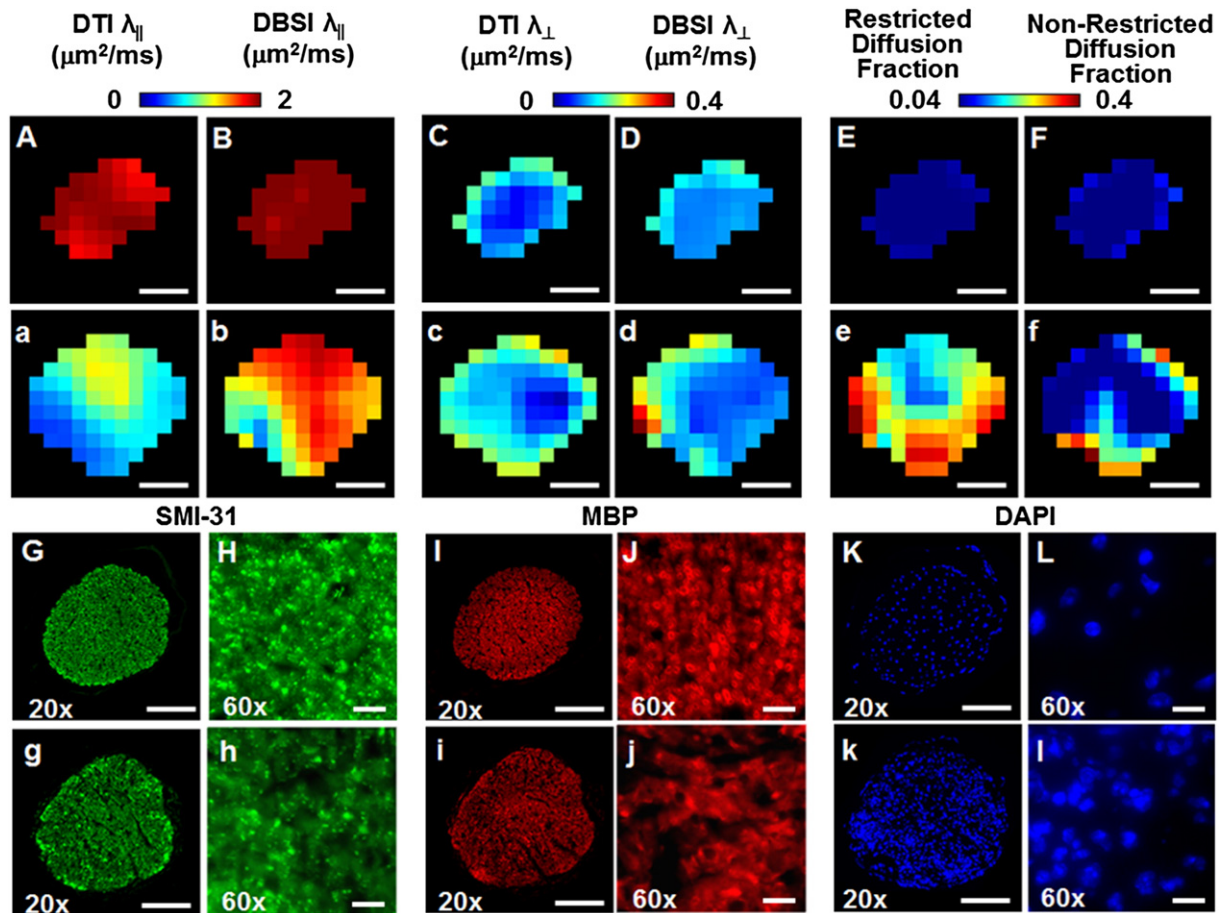


Fig. 6. Representative *in vivo* DTI/DBSI parameter maps and post-MRI immunohistochemical staining of the optic nerves from the sham (labeled by capital letters) and EAE-affected mice (labeled by lower case letters) were employed to detect underlying optic nerve pathologies. The decreased $\lambda_{||}$ measured by DTI (a) and DBSI (b) matching the SMI-31 staining (g and h) in EAE optic nerve comparing with those seen in the sham (A, B, G, and H) reflected axonal injury. Demyelination was seen as increased λ_{\perp} in EAE optic nerves derived by DTI (c) and DBSI (d) and the loss of MBP staining (i and j) comparing with that of the sham (C, D, I, and J). Increased restricted diffusion fraction (e) of EAE matched the pattern of increased DAPI-positive nuclear staining (k and l), comparing with that of the sham optic nerve (E, K, and L). Increased non-restricted diffusion tensor fraction derived by DBSI was also increased (f) in the EAE optic nerve comparing with the sham (E), potentially reflecting the increased vasogenic edema at the onset of optic neuritis. The correspondence between *in vivo* DBSI and postmortem immunohistochemistry findings supports that the 25-direction diffusion encoding scheme is adequate for assessing optic nerve pathologies in EAE mice. Quantitative analysis of immunohistochemical staining was performed on the 60 \times images (H, h, J, j) for SMI-31 and MBP, and on 20 \times image of DAPI (K, k). Scale bars represent 100 μ m (20 \times), 10 μ m (60 \times).

diffusion parameters of white matter tracts. Specifically, increased cellularity, as evidenced by increased isotropic restricted diffusion, decreased the DTI derived FA and $\lambda_{||}$ while having a limited impact on λ_{\perp} . Increased vasogenic edema, as evidenced by increased non-restricted isotropic diffusion, also decreased the DTI derived FA but increased λ_{\perp} with the extent of impact on $\lambda_{||}$ depending on the ADC value of edema relative to $\lambda_{||}$ and λ_{\perp} of axon. These confounding effects were resolved and quantified by the recently developed DBSI analysis (Wang et al., 2011), as demonstrated herein using data generated by both Monte-Carlo simulation and tissue phantoms. Our prior study used 99-direction diffusion encoding (Wang et al., 2011). A 25-direction diffusion encoding scheme (Batchelor et al., 2003) was assessed in this study to demonstrate its adequacy for performing DBSI analysis on optic nerves from the mouse at the onset of acute optic neuritis.

The partial volume effect of CSF, *i.e.*, non-restricted (free) isotropic diffusion, on DTI indices has long been recognized, and limits DTI capability in regions abutting CSF, such as periventricular regions that are commonly affected by MS. The inclusion of the isotropic component of free diffusion improved fiber diffusion measurements (Alexander et al., 2001; Papadakis et al., 2002). However, such modification is insufficient to deal with coexisting CNS inflammation (increased cellularity and vasogenic edema) or tissue loss that may be seen in diseased tissues

(Horsfield and Jones, 2002). To properly model the effect of CNS inflammation and tissue loss, allowing a more accurate evaluation of the diffusion properties of white matter fiber tracts, multiple extra-fiber diffusion components (both restricted and non-restricted isotropic diffusion components) must be identified and quantified. DBSI considers a spectrum of isotropic diffusion components of a wide range of ADC to account for the extra-fiber tissue and pathological components. The current results from fixed normal tissues and gel phantoms, and our previous *in vivo* mouse brain data (Wang et al., 2011) suggest that the DBSI approach allowed for an accurate estimation of white matter tract diffusion properties in the presence of increased cellularity and vasogenic edema.

The close agreement between the experimental measurements of fixed trigeminal nerve plus gel phantoms and the results from Monte-Carlo simulations using restricted and non-restricted isotropic diffusion components to mimic cells and vasogenic edema supported our approach of including a linear combination of isotropic diffusion spectra to account for the effect of CNS inflammation and tissue loss. One advantage of using DBSI is its capability to resolve crossing fibers while still quantitatively deriving fiber associated anisotropic diffusion tensors to assess the axon and myelin integrity (Wang et al., 2011). Previously, to resolve crossing fibers and quantifying extra-fiber cellularity and edema a 99-direction diffusion encoding scheme was employed

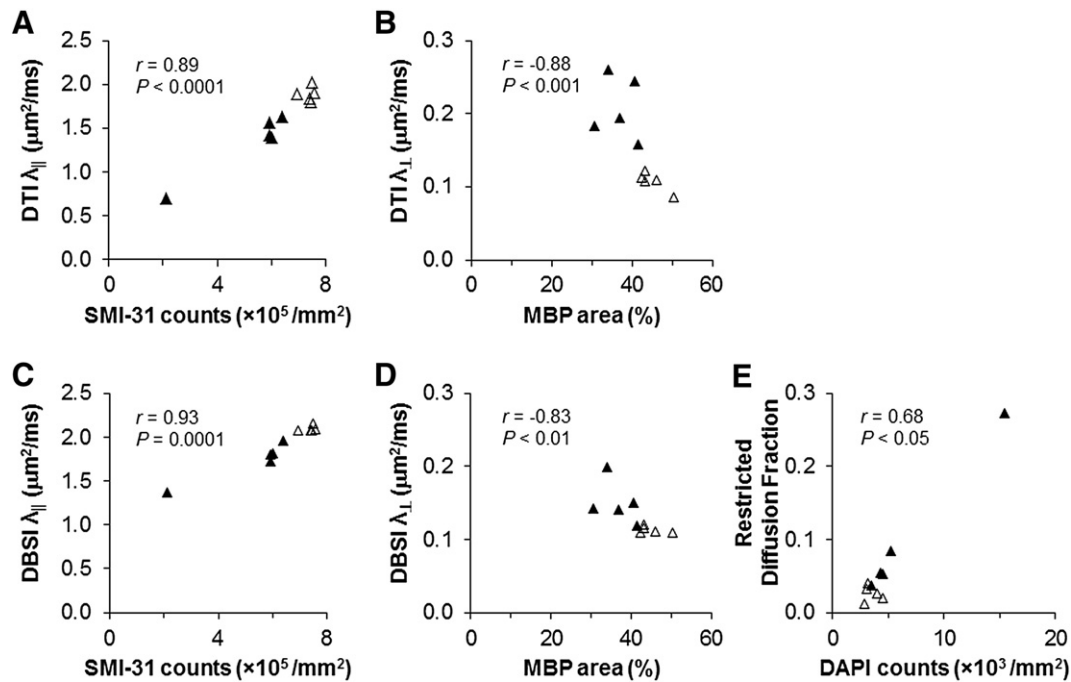


Fig. 7. Consistent with previous findings that *in vivo* DTI derived $\lambda_{||}$ and λ_{\perp} correctly reflected optic nerve axonal injury and demyelination (A, and B). During the onset of optic neuritis, inflammation led to the increased cellularity (evidenced by increased DAPI-positive counts and increased DBSI-derived restricted diffusion fraction) and edema (increased non-restricted diffusion fraction detected by DBSI). It is unclear how exactly these two factors counteracted in computation of DTI derived parameters. The current and previous results suggest that DTI detected the underlying axonal injury and demyelination in optic nerves of EAE mice. DBSI derived $\lambda_{||}$, λ_{\perp} , and the restricted diffusion fraction correlated with SMI-31 (C), MBP (D), and DAPI (E) staining well.

(Wang et al., 2011). In the case where crossing fibers are not of concern such as when studying optic nerve and spinal cord white matter tracts, a reduced data acquisition scheme may be sufficient for DBSI analysis. In the present study, the 25-direction diffusion scheme was assessed and proved to be adequate for DBSI analysis of coherent white matter tracts to quantify the extent of cellularity and edema. Thus, existing diffusion weighted data acquired using 25- or other multiple-direction encoding schemes with multiple b-values may be suitable for DBSI analysis without reacquiring new data to examine the single coherent fiber tracts.

Similar to previous results on corpus callosum from cuprizone treated mice (Wang et al., 2011), *in vivo* DBSI derived restricted isotropic diffusion fraction map of optic nerve from EAE mice revealed a heterogeneous increase in cellularity, closely matching the pattern of DAPI-positive cell nuclei staining of the same nerve (Figs. 6e, k, and l). Note that “cellularity” used in this context is not an equivalent of cell density. Instead, it is a measure of T1, T2, and proton density weighted signal fraction corresponding to restricted isotropic diffusion components within each image voxel (Eq. (1)). Restricted isotropic diffusion fractions have been assigned as “cellularity” fractions because our phantom and animal studies demonstrated a linear correlation between this restricted isotropic diffusion fraction and DAPI nuclei counts.

Various MR techniques have been used to assess inflammation of optic neuritis, but rarely demonstrated the ability to image cellularity changes non-invasively. For example, gadolinium-enhanced T1W images reflect the leakage of blood–brain barrier (Guy et al., 1990; Hickman et al., 2004b; Qi et al., 2007) without information regarding the cellular infiltration. Iron-oxide particles have been used to allow *in vivo* visualization of macrophages, but this method is insensitive to non-phagocytic cells involved in inflammation (Vellinga et al., 2008). An increased optic nerve area (swelling) has also been considered to reflect the severity of inflammation in acute optic neuritis (Boretius et al., 2008; Hickman et al., 2004a). Unfortunately, this method is nonspecific,

as a changed nerve cross-sectional size may reflect cell infiltration and/or edema and is further confounded by any tissue loss that may be present (Hickman et al., 2004a).

In the present study, both DTI and DBSI derived axial and radial diffusivity correctly detected axonal injury and demyelination in the optic nerve at the onset of optic neuritis. This suggests that DTI works well on these mice probably due to the counteraction of increased restricted and hindered/free diffusion tensor components. When examined using DBSI, the co-localization of axonal injury and myelin damage with cell infiltration was seen in the EAE-affected optic nerve. Interestingly, the region of increased cellularity did not always correspond to visible nerve damage (Figs. 6a, b, and e). This is consistent with the pathogenesis of optic neuritis in EAE, *i.e.*, nerve injury originates from the induced CNS inflammation but may not always occur with inflammation, and when it does occur axon injury may extend well outside the region of inflammation (Gold et al., 2006; Iglesias et al., 2001). Such pathological profile can now be detected using DBSI noninvasively.

MRI greatly aids CNS disease diagnosis, but current methods do not assess specific elements of CNS pathology. Gadolinium contrast enhancement (Gd+) can detect a compromised blood–CNS-barrier (BBB), which is useful to screen potential new anti-inflammatory disease modifying drugs. However, Gd + MRI is not sensitive to small inflammatory lesions or inflammation behind the intact BBB, underscoring the need to improve imaging sensitivity and specificity to identify new beneficial therapies. Without injecting Gadolinium contrast agent, DBSI provides a noninvasive imaging biomarker of inflammation, which could potentially enhance our capability to more accurately evaluate neuro-inflammation in CNS disease. In addition, DBSI-derived indices hold the promise to reflect the various specific components of the CNS pathology to identify new beneficial therapies that affect more than just inflammation. To be most useful, a new technique should be feasible on present clinical scanners. With fast diffusion-weighted EPI sequence available on 3.0 T clinical scanners,

99-direction human whole brain DBSI scans can be performed within 15 min, making DBSI protocol feasible for routine clinical scanning of patients.

DBSI in its current form does not consider the effect of water exchange between intracellular and extracellular space, which can potentially affect the accuracy of DBSI metrics, especially under pathological conditions where the permeability of cell membranes may be altered. In addition, DBSI was developed to quantify the effect of inflammation on diffusion MRI determined axonal injury and demyelination in white matter tracts. Further generalization of DBSI model is needed to expand its use in quantifying changes in gray matter pathology commonly seen in CNS disorders.

In summary, we have demonstrated that DBSI removes confounding effects of increased cellularity and vasogenic edema on DTI derived $\lambda_{||}$, λ_{\perp} , and FA. In addition, DBSI quantified the extent of increased cellularity and vasogenic edema resulting from inflammation. We have also demonstrated using *in vivo* DBSI and post-MRI immunohistochemistry on EAE mice that in the coherent white matter tracts such as optic nerves the 25-direction diffusion weighting scheme is sufficient to estimate fiber $\lambda_{||}$, λ_{\perp} , FA, and restricted (correlating with cellularity) and non-restricted diffusion fractions.

Acknowledgments

The authors thank Robert Mikesell for his assistance with the immunization of mice to induce EAE. This study was supported in part by the grants from the National Institute of Health R01-NS047592 (S.-K.S.), P01-NS059560 (A.H.C.), National Multiple Sclerosis Society (NMSS) RG 4549A4/1 (S.-K.S.), and Department of Defense Ideal Award W81XWH-12-1-0457 (S.-K.S.).

Appendix A. 99-Direction DBSI diffusion encoding scheme (Wang et al., 2011)

Number	Gro	Gpe	Gss	Number	Gro	Gpe	Gss	Number	Gro	Gpe	Gss
1	-3	0	0	34	-1	2	0	67	1	-2	1
2	-2	-2	0	35	-1	2	1	68	1	-1	-2
3	-2	-1	-1	36	0	-3	0	69	1	-1	-1
4	-2	-1	0	37	0	-2	-2	70	1	-1	0
5	-2	-1	1	38	0	-2	-1	71	1	-1	1
6	-2	0	-2	39	0	-2	0	72	1	-1	2
7	-2	0	-1	40	0	-2	1	73	1	0	-2
8	-2	0	0	41	0	-2	2	74	1	0	-1
9	-2	0	1	42	0	-1	-2	75	1	0	0
10	-2	0	2	43	0	-1	-1	76	1	0	1
11	-2	1	-1	44	0	-1	0	77	1	0	2
12	-2	1	0	45	0	-1	1	78	1	1	-2
13	-2	1	1	46	0	-1	2	79	1	1	-1
14	-2	2	0	47	0	0	-3	80	1	1	0
15	-1	-2	-1	48	0	0	-2	81	1	1	1
16	-1	-2	0	49	0	0	-1	82	1	1	2
17	-1	-2	1	50	0	0	0	83	1	2	-1
18	-1	-1	-2	51	0	0	1	84	1	2	0
19	-1	-1	-1	52	0	0	2	85	1	2	1
20	-1	-1	0	53	0	0	3	86	2	-2	0
21	-1	-1	1	54	0	1	-2	87	2	-1	-1
22	-1	-1	2	55	0	1	-1	88	2	-1	0
23	-1	0	-2	56	0	1	0	89	2	-1	1
24	-1	0	-1	57	0	1	1	90	2	0	-2
25	-1	0	0	58	0	1	2	91	2	0	-1
26	-1	0	1	59	0	2	-2	92	2	0	0
27	-1	0	2	60	0	2	-1	93	2	0	1
28	-1	1	-2	61	0	2	0	94	2	0	2
29	-1	1	-1	62	0	2	1	95	2	1	-1
30	-1	1	0	63	0	2	2	96	2	1	0
31	-1	1	1	64	0	3	0	97	2	1	1
32	-1	1	2	65	1	-2	-1	98	2	2	0
33	-1	2	-1	66	1	-2	0	99	3	0	0

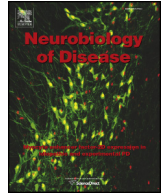
Appendix B. 25-Direction icosahedral sampling scheme (Batchelor et al., 2003)

Number	Gro	Gpe	Gss
1	0	-0.2	0
2	-0.17	-0.46	0
3	0.24	-0.62	0
4	0.21	-0.65	-0.42
5	-0.53	-0.53	-0.53
6	-0.16	-0.16	0.16
7	0.31	-0.31	0.31
8	0.11	-0.35	0.59
9	0	-0.29	-0.77
10	0	-0.33	0.88
11	0.15	-0.11	-0.29
12	-0.54	-0.17	0
13	0.69	-0.22	0
14	0.72	0	-0.45
15	-0.5	0	-0.82
16	-0.37	0	-0.14
17	-0.56	0	0.21
18	0.32	0.23	-0.64
19	-0.6	0.44	-0.46
20	0.67	0.49	0.52
21	0.07	0.22	0.38
22	-0.37	0.37	0.37
23	0.2	0.63	-0.41
24	-0.53	0.72	0
25	0.59	0.81	0

References

- Alexander, D.C., Pierpaoli, C., Basser, P.J., Gee, J.C., 2001. Spatial transformations of diffusion tensor magnetic resonance images. *IEEE Trans. Med. Imaging* 20, 1131–1139.
- Alexander, D.C., Hubbard, P.L., Hall, M.G., Moore, E.A., Ptito, M., Parker, G.J., Dyrby, T.B., 2010. Orientationally invariant indices of axon diameter and density from diffusion MRI. *NeuroImage* 52, 1374–1389.
- Anderson, A.W., Xie, J., Pizzonia, J., Bronen, R.A., Spencer, D.D., Gore, J.C., 2000. Effects of cell volume fraction changes on apparent diffusion in human cells. *Magn. Reson. Imaging* 18, 689–695.
- Assaf, Y., Basser, P.J., 2005. Composite hindered and restricted model of diffusion (CHARMED) MR imaging of the human brain. *NeuroImage* 27, 48–58.
- Assaf, Y., Ben-Bashat, D., Chapman, J., Peled, S., Biton, I.E., Kafri, M., Segev, Y., Hendler, T., Korczyn, A.D., Graif, M., Cohen, Y., 2002. High b-value q-space analyzed diffusion-weighted MRI: application to multiple sclerosis. *Magn. Reson. Med.* 47, 115–126.
- Batchelor, P.G., Atkinson, D., Hill, D.L., Calamante, F., Connolly, A., 2003. Anisotropic noise propagation in diffusion tensor MRI sampling schemes. *Magn. Reson. Med.* 49, 1143–1151.
- Blewitt, E.S., Pogmore, T., Talbot, I.C., 1982. Double embedding in agar/paraffin wax as an aid to orientation of mucosal biopsies. *J. Clin. Pathol.* 35, 365.
- Boretius, S., Gadjanski, I., Demmer, I., Bahr, M., Diem, R., Michaelis, T., Frahm, J., 2008. MRI of optic neuritis in a rat model. *NeuroImage* 41, 323–334.
- Chiang, C.W., Wang, Y., Lin, T.H., Cross, A.H., Song, S.K., 2011. Acute visual function impairment in EAE is primarily caused by optic nerve inflammation as assessed by DBSI. *Proc. Int. Soc. Magn. Reson. Med.* 20, 3085.
- DeBoy, C.A., Zhang, J., Dike, S., Shats, I., Jones, M., Reich, D.S., Mori, S., Nguyen, T., Rothstein, B., Miller, R.H., Griffin, J.T., Kerr, D.A., Calabresi, P.A., 2007. High resolution diffusion tensor imaging of axonal damage in focal inflammatory and demyelinating lesions in rat spinal cord. *Brain* 130, 2199–2210.
- Gold, R., Linington, C., Lassmann, H., 2006. Understanding pathogenesis and therapy of multiple sclerosis via animal models: 70 years of merits and culprits in experimental autoimmune encephalomyelitis research. *Brain* 129, 1953–1971.
- Guy, J., Mancuso, A., Quisling, R.G., Beck, R., Moster, M., 1990. Gadolinium-DTPA-enhanced magnetic resonance imaging in optic neuropathies. *Ophthalmology* 97, 592–599 (discussion 599–600).
- Hickman, S.J., Toosy, A.T., Jones, S.J., Altmann, D.R., Miszkil, K.A., MacManus, D.G., Barker, G. J., Plant, G.T., Thompson, A.J., Miller, D.H., 2004a. A serial MRI study following optic nerve mean area in acute optic neuritis. *Brain* 127, 2498–2505.
- Hickman, S.J., Toosy, A.T., Miszkil, K.A., Jones, S.J., Altmann, D.R., MacManus, D.G., Plant, G.T., Thompson, A.J., Miller, D.H., 2004b. Visual recovery following acute optic neuritis – a clinical, electrophysiological and magnetic resonance imaging study. *J. Neurol.* 251, 996–1005.
- Horsfield, M.A., Jones, D.K., 2002. Applications of diffusion-weighted and diffusion tensor MRI to white matter diseases – a review. *NMR Biomed.* 15, 570–577.
- Iglesias, A., Bauer, J., Litznerburger, T., Schubart, A., Linington, C., 2001. T- and B-cell responses to myelin oligodendrocyte glycoprotein in experimental autoimmune encephalomyelitis and multiple sclerosis. *Glia* 36, 220–234.

- Jensen, J.H., Helpert, J.A., Ramani, A., Lu, H., Kaczynski, K., 2005. Diffusional kurtosis imaging: the quantification of non-gaussian water diffusion by means of magnetic resonance imaging. *Magn. Reson. Med.* 53, 1432–1440.
- Kim, J.H., Budde, M.D., Liang, H.F., Klein, R.S., Russell, J.H., Cross, A.H., Song, S.K., 2006. Detecting axon damage in spinal cord from a mouse model of multiple sclerosis. *Neurobiol. Dis.* 21, 626–632.
- Kuo, L.W., Chen, J.H., Wedeen, V.J., Tseng, W.Y., 2008. Optimization of diffusion spectrum imaging and q-ball imaging on clinical MRI system. *NeuroImage* 41, 7–18.
- Liu, C., Bammer, R., Acar, B., Moseley, M.E., 2004. Characterizing non-Gaussian diffusion by using generalized diffusion tensors. *Magn. Reson. Med.* 51, 924–937.
- Lodygensky, G.A., West, T., Stump, M., Holtzman, D.M., Inder, T.E., Neil, J.J., 2010. In vivo MRI analysis of an inflammatory injury in the developing brain. *Brain Behav. Immun.* 24, 759–767.
- Naismith, R.T., Xu, J., Tutlam, N.T., Scully, P.T., Trinkaus, K., Snyder, A.Z., Song, S.K., Cross, A.H., 2010. Increased diffusivity in acute multiple sclerosis lesions predicts risk of black hole. *Neurology* 74, 1694–1701.
- Panagiotaki, E., Schneider, T., Siow, B., Hall, M.G., Lythgoe, M.F., Alexander, D.C., 2012. Compartment models of the diffusion MR signal in brain white matter: a taxonomy and comparison. *NeuroImage* 59, 2241–2254.
- Papadakis, N.G., Martin, K.M., Mustafa, M.H., Wilkinson, I.D., Griffiths, P.D., Huang, C.L., Woodruff, P.W., 2002. Study of the effect of CSF suppression on white matter diffusion anisotropy mapping of healthy human brain. *Magn. Reson. Med.* 48, 394–398.
- Pasternak, O., Sochen, N., Gur, Y., Intrator, N., Assaf, Y., 2009. Free water elimination and mapping from diffusion MRI. *Magn. Reson. Med.* 62, 717–730.
- Qi, X., Lewin, A.S., Sun, L., Hauswirth, W.W., Guy, J., 2007. Suppression of mitochondrial oxidative stress provides long-term neuroprotection in experimental optic neuritis. *Invest. Ophthalmol. Vis. Sci.* 48, 681–691.
- Scherrer, B., Warfield, S.K., 2012. Parametric representation of multiple white matter fascicles from cube and sphere diffusion MRI. *PLoS ONE* 7, e48232.
- Schmierer, K., Wheeler-Kingshott, C.A., Boulby, P.A., Scaravilli, F., Altmann, D.R., Barker, G.J., Tofts, P.S., Miller, D.H., 2007. Diffusion tensor imaging of post mortem multiple sclerosis brain. *NeuroImage* 35, 467–477.
- Song, S.K., Sun, S.W., Ramsbottom, M.J., Chang, C., Russell, J., Cross, A.H., 2002. Demyelination revealed through MRI as increased radial (but unchanged axial) diffusion of water. *NeuroImage* 17, 1429–1436.
- Stanisz, G.J., Szafer, A., Wright, G.A., Henkelman, R.M., 1997. An analytical model of restricted diffusion in bovine optic nerve. *Magn. Reson. Med.* 37, 103–111.
- Stolzenburg, J.U., Reichenbach, A., Neumann, M., 1989. Size and density of glial and neuronal cells within the cerebral neocortex of various insectivorous species. *Glia* 2, 78–84.
- Sun, S.W., Liang, H.F., Trinkaus, K., Cross, A.H., Armstrong, R.C., Song, S.K., 2006. Noninvasive detection of cuprizone induced axonal damage and demyelination in the mouse corpus callosum. *Magn. Reson. Med.* 55, 302–308.
- Sun, S.W., Liang, H.F., Cross, A.H., Song, S.K., 2008. Evolving Wallerian degeneration after transient retinal ischemia in mice characterized by diffusion tensor imaging. *NeuroImage* 40, 1–10.
- Tu, T.W., Budde, M.D., Quirk, J.D., Song, S.K., 2010. Using absorption-mode images to improve in vivo DTI quality. *Proc. Int. Soc. Magn. Reson. Med.* 18, 4001.
- Vellinga, M.M., Engberink, R.D.O., Seewann, A., Pouwels, P.J.W., Wattjes, M.P., van der Pol, S.M.A., Pering, C., Polman, C.H., de Vries, H.E., Geurts, J.J.G., Barkhof, F., 2008. Pluriformity of inflammation in multiple sclerosis shown by ultra-small iron oxide particle enhancement. *Brain* 131, 800–807.
- Wang, Y., Wang, Q., Haldar, J.P., Yeh, F.C., Xie, M., Sun, P., Tu, T.W., Trinkaus, K., Klein, R.S., Cross, A.H., Song, S.K., 2011. Quantification of increased cellularity during inflammatory demyelination. *Brain* 134, 3590–3601.
- Wedeen, V.J., Hagmann, P., Tseng, W.Y., Reese, T.G., Weisskoff, R.M., 2005. Mapping complex tissue architecture with diffusion spectrum magnetic resonance imaging. *Magn. Reson. Med.* 54, 1377–1386.
- Werring, D.J., Clark, C.A., Barker, G.J., Thompson, A.J., Miller, D.H., 1999. Diffusion tensor imaging of lesions and normal-appearing white matter in multiple sclerosis. *Neurology* 52, 1626–1632.
- Zhang, H., Schneider, T., Wheeler-Kingshott, C.A., Alexander, D.C., 2012. NODDI: practical in vivo neurite orientation dispersion and density imaging of the human brain. *NeuroImage* 61, 1000–1016.



Diffusion fMRI detects white-matter dysfunction in mice with acute optic neuritis



Tsen-Hsuan Lin^{a,1}, William M. Spees^{b,e}, Chia-Wen Chiang^b, Kathryn Trinkaus^c, Anne H. Cross^{d,e}, Sheng-Kwei Song^{b,e,*}

^a Department of Physics, Washington University, St. Louis, MO 63130, USA

^b Department of Radiology, Washington University School of Medicine, St. Louis, MO 63110, USA

^c Department of Biostatistics, Washington University School of Medicine, St. Louis, MO 63110, USA

^d Department of Neurology, Washington University School of Medicine, St. Louis, MO 63110, USA

^e Hope Center for Neurological Disorders, Washington University School of Medicine, St. Louis, MO 63110, USA

ARTICLE INFO

Article history:

Received 24 December 2013

Revised 18 February 2014

Accepted 25 February 2014

Available online 13 March 2014

Keywords:

Diffusion fMRI

White matter

EAE

Optic neuritis

Visual acuity

ABSTRACT

Optic neuritis is a frequent and early symptom of multiple sclerosis (MS). Conventional magnetic resonance (MR) techniques provide means to assess multiple MS-related pathologies, including axonal injury, demyelination, and inflammation. A method to directly and non-invasively probe white-matter function could further elucidate the interplay of underlying pathologies and functional impairments. Previously, we demonstrated a significant 27% activation-associated decrease in the apparent diffusion coefficient of water perpendicular to the axonal fibers (ADC_{\perp}) in normal C57BL/6 mouse optic nerve with visual stimulation using diffusion fMRI. Here we apply this approach to explore the relationship between visual acuity, optic nerve pathology, and diffusion fMRI in the experimental autoimmune encephalomyelitis (EAE) mouse model of optic neuritis. Visual stimulation produced a significant 25% (vs. baseline) ADC_{\perp} decrease in sham EAE optic nerves, while only a 7% (vs. baseline) ADC_{\perp} decrease was seen in EAE mice with acute optic neuritis. The reduced activation-associated ADC_{\perp} response correlated with post-MRI immunohistochemistry determined pathologies (including inflammation, demyelination, and axonal injury). The negative correlation between activation-associated ADC_{\perp} response and visual acuity was also found when pooling EAE-affected and sham groups under our experimental criteria. Results suggest that reduction in diffusion fMRI directly reflects impaired axonal-activation in EAE mice with optic neuritis. Diffusion fMRI holds promise for directly gauging in vivo white-matter dysfunction or therapeutic responses in MS patients.

© 2014 Elsevier Inc. All rights reserved.

Introduction

Multiple sclerosis (MS) is an inflammatory demyelinating disease affecting the brain, optic nerve, and spinal cord (Compston and Coles, 2008; Filippi et al., 2012; Trapp and Nave, 2008). Optic neuritis is a frequent first sign of MS, which produces blurred vision and/or pain in the affected eye due to inflammation and demyelination at foci within optic nerve (Arnold, 2005; Beck et al., 2003; Brodsky et al., 2008). Experimental autoimmune encephalomyelitis (EAE) induced by inoculation of myelin oligodendrocyte glycoprotein (MOG) peptide is a widely used animal model of human MS. Many features of the pathology in this EAE model resemble those characteristic of MS, including

inflammation, demyelination, and axonal injury and loss (Diem et al., 2008; Emerson et al., 2009; Gold et al., 2006; Sun et al., 2007).

Magnetic resonance imaging (MRI) is routinely used to detect and quantify pathologies in EAE animal models and MS patients (Emerson et al., 2009; Filippi, 2003; Filippi et al., 2012; Ge, 2006; Inglese and Bester, 2010). For instance, diffusion-MRI-derived axial diffusivity, radial diffusivity, fractional anisotropy, and mean diffusivity have been used to identify axonal injury, demyelination, inflammation, and axonal loss (Naismith et al., 2010; Roosendaal et al., 2009; Song et al., 2005; Sun et al., 2007; Wu et al., 2007). Abnormal T2-weighted hyperintensities within white matter may reflect several pathologies, including inflammation, demyelination, and axonal loss (Bruck et al., 1997; Sahraian and Eshaghi, 2010). Significant axon loss can lead to persistent T1-weighted hypointensities (van Walderveen et al., 1998). T1-weighted gadolinium contrast-enhancement is indicative of compromised blood–brain barrier (BBB), which is associated with inflammation in EAE models and MS (Boretius et al., 2008; Broom et al., 2005; Bruck et al., 1997; Filippi et al., 1995; Nessler et al., 2007). More accurate and novel approaches have recently been introduced to distinguish coexisting inflammation,

* Corresponding author at: Biomedical MR Laboratory, Campus Box 8227, Washington University School of Medicine, Room 2313, 4525 Scott Ave, St. Louis, MO 63110, USA. Fax: +1 314 362 0526.

E-mail address: ssong@wustl.edu (S.-K. Song).

Available online on ScienceDirect (www.sciencedirect.com).

¹ Current Address: Institute of Biomedical Sciences, Academia Sinica, Taipei City 11529, Taiwan.

demyelination, and axonal injury using diffusion basis spectrum image (DBSI) or diffusion kurtosis image (DKI) (Chiang et al., 2012; Raz et al., 2013; Tu et al., 2012; Wang et al., 2011).

MRI also holds potential to probe functional integrity in real time. For instance, blood oxygen level dependent (BOLD) fMRI has been applied to study brain plasticity and cortical activation in MS patients (Gallo et al., 2012; Rocca et al., 2012a,b; Staffen et al., 2002) as a reflection of motor or visual functional deficits. However, conventional BOLD fMRI relies on local modulation of blood volume and blood flow, secondary to neuronal activation and metabolic demand, it is an approach which is largely limited to cortical and gray-matter regions (Heeger and Ress, 2002; Logothetis, 2008) and mainly reflects post-synaptic activity in cortical regions (Gawryluk et al., 2009; Logothetis et al., 2001). Since EAE and MS are diseases that significantly affect white-matter tracts, a method to directly assess white-matter function (in combination with BOLD fMRI in gray matter) could provide more comprehensive information about disease progression and therapeutic response in experimental models and the clinic.

Diffusion fMRI has recently been introduced and suggested as an alternative approach to directly identify functional integrity of neurons and axons (Darquie et al., 2001; Flint et al., 2009; Le Bihan, 2012; Le Bihan et al., 2006; Spees et al., 2013; Tsurugizawa et al., 2013). Diffusion fMRI offers a promising means to assess axonal function since BOLD-based fMRI has not been successful in white matter and our previous report showed a significant 27% ADC_{\perp} decrease during visual stimulation in healthy mouse optic nerves. Importantly, this activation-associated ADC_{\perp} decrease in optic nerves was found to be independent of any vascular contribution (Spees et al., 2013).

In the current study, diffusion fMRI was evaluated as a non-invasive probe of in vivo optic nerve axonal dysfunction in mice with acute-stage EAE with unilateral optic neuritis. The prevalence of optic neuritis in the disease course of MS provides motivation for the current studies. Moreover, the optic nerve can be viewed as a prototypical white-matter structure, thus the current investigation lays the groundwork for future studies of MS pathophysiology and therapeutic outcome in other CNS white-matter targets.

Materials and methods

All experimental procedures involving animals were approved by Washington University's Animal Studies Committee and conformed to the NIH Policy on Responsibility for Care and Use of Animals.

Experimental autoimmune encephalomyelitis (EAE) mouse model

Fourteen 7-week-old, female C57BL/6 mice were obtained from Jackson Laboratory (Bar Harbor, ME). Before immunization, mice were housed under a 12-hour dark/light cycle for a week. Mice were randomly separated into two groups: seven in the EAE group and seven in the sham group. The mice in the EAE group were immunized with 50 μ g MOG_{35–55} peptide emulsified (1:1) in incomplete Freund's adjuvant (IFA) and desiccated *Mycobacterium tuberculosis*. Pertussis toxin (300 ng; PTX, List Laboratories, Campbell, CA) was injected intravenously on the day of MOG_{35–55} immunization and two days later. Mice in the sham control group underwent the same procedure with only IFA and pertussis toxin injected.

Visual acuity (VA)

Mouse visual acuity was assessed using the Virtual Optometry System (OptoMotry, CerebralMechanics, Inc., Canada). Briefly, virtual rotating columns (vertical light/dark bands) were projected onto four LCD monitors, surrounding a platform where the mouse stands, with varied spatial frequencies in cycles/degree (c/d). The mouse head movement in response to the virtual column rotations was noted. The spatial frequency was changed starting from 0.1 c/d in increments or

decrement of 0.05 c/d until the mouse stopped responding. The VA was defined as the highest spatial frequency of virtual rotating columns to which the mouse responded. Before immunization, normal VA was confirmed for each eye ($n = 28$, $VA = 0.37 \pm 0.02$ c/d) to exclude mice with poor vision at baseline due to unrelated factors. After immunization, VA was assessed daily in all mice. For animals in the EAE group, $VA \leq 0.25$ c/d (8–13 days post-immunization) was defined as the onset of acute optic neuritis (Chiang et al., 2012). For EAE animals, diffusion fMRI measurements were performed on the first day (10.6 ± 1.7 days post-immunization, mean \pm SD) at which their VA was observed to be below 0.25 c/d, at which time the VA decline was invariably unilateral. The mice in the sham group did not develop visual impairment, but underwent the diffusion fMRI procedure within the same time range (10.6 ± 1.7 days post-immunization, mean \pm SD).

Animal anesthesia and set-up

For initial setup, mice were anesthetized with 1.5% isoflurane in O_2 . Anesthetized mice were placed in a custom-made stereotactic head holder. The experimental eye remained open to receive light stimulus. The contralateral eye was covered with Parafilm™ and two layers of black electrical tape to block out the flashing light (also identified as “blocked” eyes in the text). After careful setup the mouse and head holder were placed in the imaging cradle. Respiratory rate and body temperature were monitored during experiments using an MR-compatible animal-monitoring system (SA Instrument, Inc., Stony Brook, NY). The body temperature was maintained at 37 °C via a regulated circulating warm water pad underneath the mouse body and regulated warm air blown into the magnet bore. When mouse respiration was stable, a subcutaneous 0.3 mg/kg bolus of medetomidine was administered followed immediately by a continuous infusion of medetomidine at a rate of 0.6 mg/kg·h through an in-dwelling subcutaneous catheter. Isoflurane in the breathing-gas mixture was gradually discontinued according to previously-described protocols until the animals were breathing room air (Adamczak et al., 2010).

Diffusion-weighted image (DWI) protocol

MRI experiments were performed on a 4.7-T Agilent DirectDrive™ small-animal MRI system (Agilent Technologies, Santa Clara, CA) equipped with a Magnex/Agilent HD imaging gradient coil (Magnex/Agilent, Oxford, UK) capable of pulsed-gradient strengths of up to 58 G/cm and a gradient rise time ≤ 295 μ s. An actively-decoupled 1.7-cm receive-only surface coil was positioned on top of the mouse head. Then, the animal holder assembly, including the receive coil was placed inside an 8-cm actively-decoupled volume transmit coil.

DWI measurements were carried out as previously described (Spees et al., 2013). In brief, a multi-echo spin-echo diffusion-weighted imaging sequence (Tu et al., 2010) was employed to improve the signal-to-noise ratio (SNR) by averaging the extra echoes of the same k-space line, during the readout period after diffusion weighting, with negligible increase in imaging time comparing with the conventional spin-echo diffusion sequence. A train of three echoes were co-added to increase signal-to-noise in the summed MR image. The following acquisition parameters were used: TR = 1.5 s, TE = 37.1 ms, inter-echo delay = 23.6 ms, FOV = 20×20 mm², matrix size = 256×256 (zero-filled to 512×512), slice thickness = 1.3 mm. To obtain the final target image plane and minimize partial volume effects, a middle-sagittal DW image (diffusion gradient applied in the slice-select direction) was acquired based on axial scout images. The sagittal DWI encompassed optic nerves of both eyes longitudinally. An image plane parallel to the optic nerves was placed overlying the nerves. By rotating this image plane by 90°, the final targeted image slice plane was orthogonal to the optic nerves to minimize partial volume effects. Two diffusion-sensitizing factors (b values), 0.1 and 1.4 ms/ μ m², i.e., 100 and 1400 s/mm² (with $\delta = 5$ ms and $\Delta = 18$ ms), were applied to generate a pair of DWIs (Figs. 1A and B).

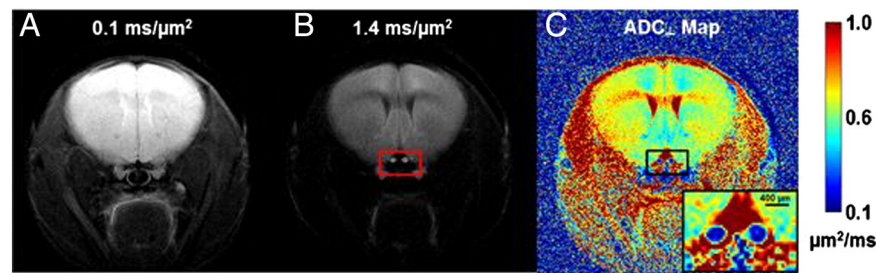


Fig. 1. Two diffusion-weighted images (DWI), which were zero-filled to 512×512 , with diffusion-sensitizing gradients applied in the phase-encoding direction (left-to-right) with b values of $0.1 \text{ ms}/\mu\text{m}^2$ (or $100 \text{ s}/\text{mm}^2$) (A) and $1.4 \text{ ms}/\mu\text{m}^2$ (or $1400 \text{ s}/\text{mm}^2$) (B) were used to generate the resulting ADC_\perp map (C). The red box in panel B highlights the location of optic nerves (bright) and surrounding cerebrospinal fluid, which is highly suppressed. ADC_\perp values in the optic nerves are considerably lower than those in other brain tissues. The regular (nearly circular) shape of the optic nerves suggests good orthogonality between the nerve axes and the slice plane, which minimizes partial volume effects.

Visual stimulation

Visual stimulation was delivered by a flashing white LED (Cree, Model C503C-WAS) placed 5 cm in front of the mouse nose, the corresponding luminance level $\sim 445 \text{ cd}/\text{m}^2$. A step-function signal of 4 V amplitude was repeated at 1.4 Hz with 200/514 ms on/off duration to generate the flashing light stimulus. Equipment set-up was as reported previously (Spees et al., 2013).

Diffusion fMRI strategy

For each mouse, three pairs of diffusion-weighted images were acquired. The first pair of images without visual stimulation was taken as a baseline. Then, the stimulus-on DWI dataset was acquired during application of flashing-light stimulation. Finally, the LED light was turned off for the post-stimulus DWI acquisition.

DWI data analysis

For measurements of diffusion perpendicular to the axonal fibers, signal decay with b -value between 0.1 and $1.4 \text{ ms}/\mu\text{m}^2$ (or 100 and $1400 \text{ s}/\text{mm}^2$) is mono-exponential (Spees et al., 2013). ADC_\perp maps were generated from the pair of DWIs according to the Stejskal–Tanner equation (Stejskal and Tanner, 1965) with code developed in-house and written in MATLAB (Mathworks, Natick, MA). Optic nerve ROIs were drawn based on operator-independent criteria as described previously (Spees et al., 2013).

Immunohistochemistry (IHC) staining in optic nerves

Following MR experiments, mice were perfused with 0.01 M phosphate-buffered saline (PBS) followed by 4% paraformaldehyde in 0.01 M PBS. The brain was excised and post-fixed in 4% paraformaldehyde/PBS for 24 h then transferred to 0.01 M PBS for storage at 4°C until histological analysis. Mouse optic nerves were embedded in 2% agar blocks (Blewitt et al., 1982). Then, the agar block was embedded in paraffin wax and $5\text{-}\mu\text{m}$ thick transverse slices were sectioned for IHC staining. Sections were deparaffinized, rehydrated, and then blocked using 1% bovine serum albumin (BSA, Sigma Inc., MO, US) and 5% normal goat-serum solution for 20 min at room temperature to prevent non-specific binding. Slides were incubated overnight at 4°C with monoclonal anti-phosphorylated neurofilament antibody (SMI-31; $1:1000$, Covance, US) to stain non-injured axons or with rabbit anti-myelin basic protein (MBP) antibody ($1:1000$, Sigma Inc., MO, US) to stain myelin sheaths (Budde et al., 2009; Song et al., 2003; Sun et al., 2008). After rinsing, goat anti-mouse IgG or goat anti-rabbit IgG conjugated Alexa 488 ($1:800$) was applied to visualize immunoreactivity of phosphorylated neurofilament and MBP. Finally, slides were covered using Vectashield Mounting Medium with $4',6\text{-diamidino-2-phenylindole}$ (DAPI, Vector Laboratory, Inc., Burlingame, CA) to stain cell nuclei (Budde et al., 2009; Wang et al., 2011). Histological slides

were examined with a Nikon Eclipse 80i fluorescence microscope equipped with a $60 \times$ water objective, and images from the center of optic nerve were captured with a black-and-white CCD camera with MetaMorph software (Universal Imaging Corporation, Sunnyvale, CA). The $60 \times$ IHC images (0.018 mm^2) covered $\sim 40\%$ of the whole optic nerve area ($0.045 \pm 0.013 \text{ mm}^2$, mean \pm SD). Histological counts are reported for 7 EAE-affected and 6 sham optic nerves in this study (one sham optic nerve specimen was damaged during tissue processing).

Histological data analysis

Whole-field SMI-31, MBP, and DAPI images at $60 \times$ magnification were captured with the same fluorescence light intensity and exposure time. All captured images were converted to 8-bit gray scale and analyzed using threshold, particle analyzer and gray level watershed segmentation functions in ImageJ (<http://bigwww.epfl.ch/sage/soft/watershed/>).

Statistical analysis

ADC_\perp changes (initial/baseline vs. stimulus on, stimulus on vs. stimulus off, etc.) were tested for statistical significance via a cluster linear repeated measures model, which took into account that there were three time points for each eye and two eyes per mouse. The p -values of visual function (VA), SMI-31, MBP, and DAPI were from nonparametric Wilcoxon two-sample tests for difference between sham and EAE groups. The correlation coefficients for VA with each of SMI-31, MBP, DAPI, and decreased ADC_\perp were analyzed by Spearman's rank correlation coefficient.

Results

Impairment of visual function and reduced activation-associated ADC_\perp response in EAE optic nerves

For animals in the EAE group, the onset of optic neuritis, defined as $\text{VA} \leq 0.25 \text{ c}/\text{d}$ (Chiang et al., 2012), occurred in the range from 8 to 13 days post-immunization (10.6 ± 1.7 days post-immunization, mean \pm SD). Group-averaged visual acuities of the EAE-affected (optic neuritis), sham and blocked eyes ($n = 7, 7$, and 14 , respectively) were 0.15 ± 0.08 , 0.36 ± 0.02 , and $0.36 \pm 0.03 \text{ c}/\text{d}$ (mean \pm SD, Fig. 2A). Since all EAE-affected mice in this study developed unilateral visual impairment, the VA of blocked eyes ($n = 14$) were in the normal range. VA of EAE-affected eyes with optic neuritis showed a significant 58% decrease ($p < 0.005$, EAE vs. sham) in measurements just prior to diffusion fMRI.

ADC_\perp maps were generated from the diffusion-weighted image data (Fig. 1). The group-averaged baseline optic-nerve ADC_\perp of affected acute-stage EAE optic neuritis eyes was higher than in sham eyes (Figs. 2B and C, Table 1). Compared to their own pre-stimulus baseline and stimulus off measurements, ADC_\perp during visual stimulus of EAE-affected versus sham eyes showed no significant (7% , $p = 0.45$, vs.

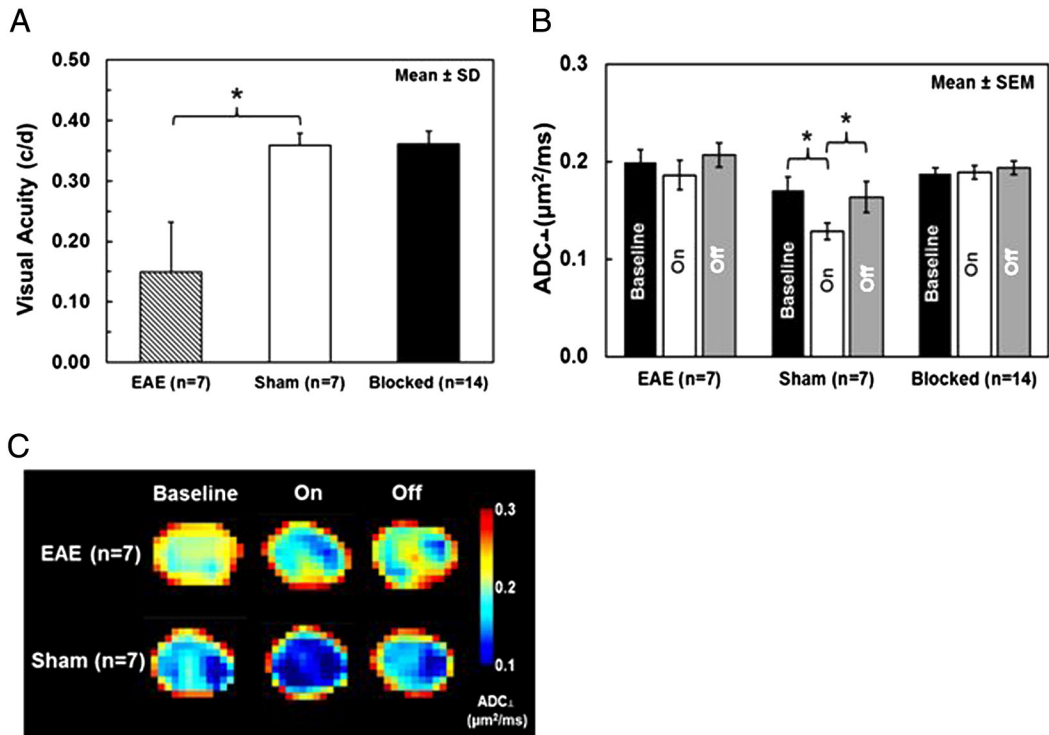


Fig. 2. Group-averaged visual acuity was significantly decreased by 58% ($p < 0.005$, vs. sham) in affected EAE eyes ($n = 7$) compared with the normal vision of sham eyes ($n = 7$); the visual acuity of contralateral blocked ($n = 14$) eyes was in the normal range (A). In this mouse model of EAE optic neuritis, visual deficits typically develop asymmetrically, beginning in only one eye. An activation-associated ADC_⊥ decrease was observed in both EAE and sham eyes but not in blocked eyes (B, C, and Table 1), suggesting that the decreased ADC_⊥ in stimulated EAE and sham optic nerves was caused by axonal activity. When compared to its own baseline and stimulus-off, ADC_⊥ significantly decreased in sham optic nerves by 25 and 22%, respectively (both $p < 0.005$, B, C, and Table 1), with visual stimulation. In contrast, only a slight and non-significant ADC_⊥ decrease (7%, $p = 0.45$, vs. baseline and 10%, $p = 0.13$, vs. stimulus-off) was observed in EAE optic nerves (B, C and Table 1). Group ADC_⊥ maps of EAE ($n = 7$) and sham ($n = 7$) optic nerves were generated by averaging stacked ADC_⊥ maps, which were interpolated to 1024×1024 (C). * indicates $p < 0.005$.

baseline and 10%, $p = 0.15$, vs. stimulus off for EAE) versus significant (25%, $p < 0.005$, vs. baseline and 22%, $p < 0.005$, vs. stimulus off for sham) decrease, respectively. No ADC_⊥ changes were observed between baseline, stimulus on, and stimulus off in the contralateral blocked eyes of mice with EAE ($p = 0.91$ for baseline vs. stimulus on and $p = 0.13$ for stimulus on vs. stimulus off) and sham ($p = 0.97$ for baseline vs. stimulus on and $p = 0.64$ for stimulus on vs. stimulus off) mice (Figs. 2B and C, Table 1). Thus EAE-affected eyes with optic neuritis as evinced by impaired visual acuity exhibited a correspondingly reduced ADC_⊥ response with visual stimulation.

Axonal impairment was assessed by immunohistochemistry (IHC) staining

Previously, we have employed immunohistochemical (IHC) staining of phosphorylated neurofilaments (SMI-31, intact axons), myelin basic protein (MBP, myelin sheath), and 4',6'-diamidino-2-phenylindole (DAPI, cell nuclei) to reflect white-matter integrity (Song et al., 2003; Sun et al., 2007; Wang et al., 2011). Representative zoomed-in $60 \times$ images (56% of the $60 \times$ field of view) from EAE-affected ($n = 7$) optic nerves demonstrated axonal beading, with lower density of intact axons, less myelin positive area (with thinner myelin), and higher density of cell nuclei (Figs. 3A, D, and G) than sham optic nerves ($n = 6$).

Table 1
Group averaged ADC of baseline, stimulus on, and stimulus off of EAE-affected ($n = 7$), sham ($n = 7$), and blocked EAE and sham ($n = 14$) eyes.

	Baseline	Stimulus on	Stimulus off
EAE	0.200 ± 0.012	0.186 ± 0.015	0.207 ± 0.012
Sham	0.171 ± 0.014	0.128 ± 0.008	0.164 ± 0.016
Blocked	0.188 ± 0.006	0.189 ± 0.007	0.196 ± 0.007

ADC (μm²/ms or $\times 10^{-3}$ mm²/s): mean ± standard error of the mean.
Blocked: contralateral EAE and sham eyes.

Group-averaged analysis of SMI-31, MBP, and DAPI (Figs. 3C, F, I and Table 2) at EAE optic neuritis onset showed a significant 22% decrease in density of intact axons [$p < 0.005$, $5.3 (\pm 0.6) \times 10^5$ mm⁻²] and 17% decrease in myelin sheath area [$p < 0.005$, $36.2 (\pm 2.5) \%$] compared with sham group [$6.8 (\pm 0.5) \times 10^5$ mm⁻² and $43.6 (\pm 2.1) \%$, respectively]. Furthermore, the density of cell nuclei in optic nerves at EAE optic neuritis onset was increased by 38% [$p < 0.05$, $5.8 (\pm 1.2) \times 10^3$ mm⁻²] compared with sham group [$4.2 (\pm 0.5) \times 10^3$ mm⁻²]. Based on IHC results, the EAE-affected optic nerves demonstrated unequivocal signs of axonal injury, demyelination, and inflammation.

Reduced activation-associated ADC_⊥ was correlated with impaired visual function and optic nerve pathologies

The correlation between activation-associated ADC_⊥ response and visual acuity was found when pooling EAE and sham groups under our experimental criteria (Fig. 4A, $r = 0.76$, $p = 0.0015$), axon density (Fig. 4B, $r = 0.92$, $p < 0.0001$), and myelin sheath area (Fig. 4C, $r = 0.76$, $p = 0.0023$) and, to a lesser degree, with cell nuclei density (Fig. 4D, $r = 0.60$, $p = 0.03$). The data suggest that diffusion fMRI can provide a means to non-invasively and directly assess axonal dysfunction associated with axonal injury, demyelination, and inflammation at optic neuritis onset in this EAE mouse model.

Discussion

This is the first study applying diffusion fMRI to assess functional deficits of a white-matter tract in vivo. The results presented here demonstrate an attenuated neuronal-activation-associated ADC_⊥ response (~7% non-significant reduction) in EAE mice at the onset of optic neuritis, compared to a significant decremental response in sham mice (~25% reduction). The results for EAE sham mice are comparable to our

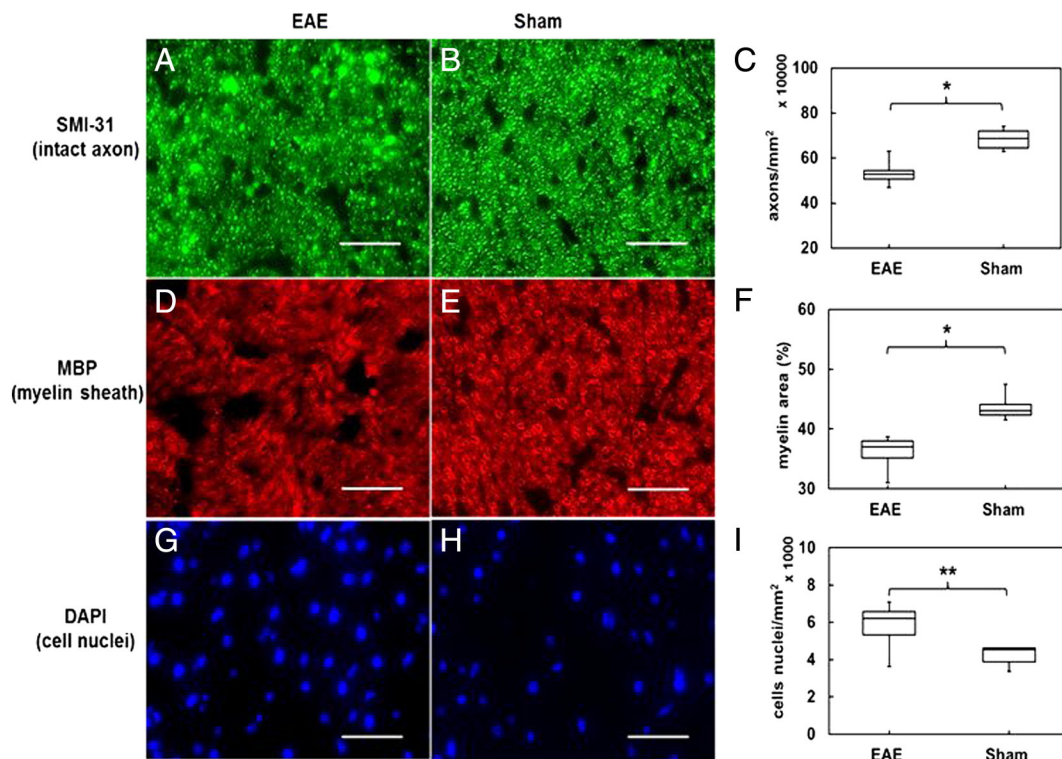


Fig. 3. Representative $60\times$ immunohistochemistry staining images of phosphorylated neurofilaments (SMI-31, intact axons), myelin basic protein (MBP, myelin sheath), and 4', 6-dianidino-2-phenylindole (DAPI, nuclei) from EAE-affected (A, D, and G,) and sham (B, E, and H) optic nerves. EAE optic nerves with optic neuritis demonstrated obvious axonal beading, lower axonal density (A), reduced myelin area (D), and more cell nuclei (G). Group-averaged IHC counts of EAE ($n = 7$) and sham ($n = 6$) optic nerves (Table 2) revealed significant SMI-31 (C) and MBP (F) decrease ($p < 0.005$) and significant DAPI (I) increase ($p < 0.05$) in the EAE-affected group. IHC results suggested that axonal impairment, demyelination, and inflammatory infiltration all contribute to visual deficits in acute-stage optic neuritis in this EAE mouse model. Scale bar: $25\ \mu\text{m}$. * indicates $p < 0.005$. ** indicates $p < 0.05$.

previously-reported $\sim 27\%$ ADC_{\perp} decrease in optic nerves of normal mice (Spees et al., 2013). Reduced activation-associated ADC_{\perp} response in association with impaired visual function (Fig. 4A) correlated with underlying optic-nerve axonal pathology (Fig. 3).

Visual signal conduction through the optic nerve depends on repeated cycles of membrane depolarization/action potential/repolarization, which are accompanied by ion gradient changes (Nicholls et al., 2001; Zhang et al., 2006). Unlike BOLD fMRI, which is largely limited to gray matter (Gawryluk et al., 2009; Logothetis et al., 2001), we proposed that diffusion fMRI could detect the effect of functional activation of axons and further improve our understanding of CNS functionality. Extracellular space (ECS) shrinkage during electrical stimulation has been reported (Holthoff and Witte, 1996; Nicholson and Sykova, 1998; Ransom and Orkand, 1996; Ransom et al., 1985), such ECS shrinkage is highly associated with transient ionic gradient changes, osmotic shifts of water across cell membranes, or glial cell swelling associated with changes in size and shape (Bay and Butt, 2012; Flint et al., 2009; Kole et al., 2008; Le Bihan, 2007; Le Bihan and Johansen-Berg, 2012; Schwartzkroin et al., 1998; Waxman, 1977). We speculated that diffusion measurement, especially, in white matter would be sensitive to extracellular space (ECS) shrinkage with relative minor vascular-coupling effect due to lower blood flow and volume. Therefore, the activation-associated ADC_{\perp} decrease of diffusion fMRI is expected. Indeed, in our

previous study, an activation-associated 27% ADC_{\perp} decrease in healthy mouse optic nerves was shown and observed to be independent of vascular-coupling contributions (Spees et al., 2013). In the same study, we did not observe ADC_{\parallel} changes during the visual stimulation. We speculate that this may be due to that ADC_{\parallel} is likely to be affected more by the intra-axonal water than that in the ECS. Hence, diffusion fMRI measuring ADC_{\perp} of axonal bundles has the potential to directly probe axon functional integrity without confounding blood-flow effects.

For MS and its animal model, EAE, mitochondrial impairment reduces energy production due to increased nitric oxide and free radical/reactive oxygen species (Smith and Lassmann, 2002). Sodium channel redistribution in demyelinated axons is required to maintain signal propagation but this also increases energy consumption (Kornek et al., 2001; Waxman, 2006). The imbalanced energy cycle would eventually lead to energy deficiency associated $\text{Na}^{+}/\text{K}^{+}$ -ATPase pump failure and the reversal of $\text{Na}^{+}/\text{Ca}^{2+}$ exchanger due to increased intracellular Na^{+} . Finally, the resultant influx and accumulation of intracellular Ca^{2+} may further lead to mitochondrial dysfunction and axonal damage (Craner et al., 2005; Stys, 2005; Su et al., 2009). Optic neuritis is frequently the first sign of MS in patients (Beck et al., 2003). Inflammation and demyelination of the affected optic nerves are associated with impeded action potential conduction (Compston and Coles, 2008) and result in impaired visual function. In EAE animal models of MS, several reports demonstrated visual dysfunction accompanying optic neuritis via behavioral or visual evoked potential (VEP) measurements (Diem et al., 2005, 2008; Matsunaga et al., 2012; Meyer et al., 2001). These measurements rely upon functionality of the entire visual pathway including the retina, optic nerve, visual cortex, and/or conscious response of the brain. Thus, they may lack specificity in the location and contribution of specific optic nerve/white-matter lesion sites. Ion-channel dysfunction and deregulation are related to impaired signal propagation. Ion-channel dysfunction and deregulation could also lead to disability of activation-associated modulation in ECS. Therefore, activation-

Table 2
Quantitative immunohistochemistry results of EAE ($n = 7$) and sham ($n = 6$) optic nerves.

	SMI31 (#/mm ²)	MBP (area %)	DAPI (#/mm ²)
EAE	$5.3 (\pm 0.6) \times 10^5$	36.2 ± 2.5	$5.8 (\pm 1.2) \times 10^3$
Sham	$6.8 (\pm 0.5) \times 10^5$	43.6 ± 2.1	$4.3 (\pm 0.5) \times 10^3$

Mean \pm standard deviation.

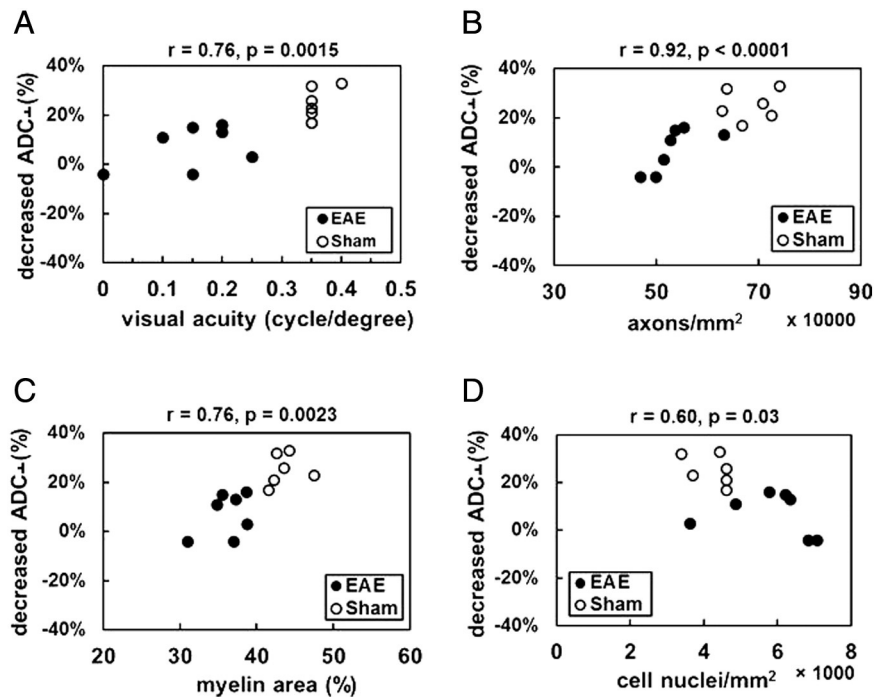


Fig. 4. The activation-associated ADC_{\perp} change (decrease in ADC_{\perp} with stimulation expressed as a percentage of baseline ADC_{\perp}) correlated well with visual function (A, $r = 0.76$, $p = 0.0015$) and the density of intact axons (B, $r = 0.92$, $p < 0.0001$) and myelination (C, $r = 0.76$, $p = 0.0023$). Reduced activation-associated ADC_{\perp} response was associated with the severity of inflammation (D, $r = 0.60$, $p = 0.03$). These data suggest that axonal impairment and dysfunction can be assessed by diffusion fMRI.

associated ADC_{\perp} decrease, which likely results from ECS shrinkage during axonal activation, was less in EAE-affected optic nerves than in sham mice optic nerves during visual stimulation.

In this study, visual acuity measurements in EAE and sham eyes represent overall function of the entire visual efferent pathway (Douglas et al., 2005; Prusky et al., 2004). If we accept that the VA measurement reflects overall electrophysiological competence as measured by VEP (Ridder and Nusinowitz, 2006), and that the optic nerve is the primary site of impaired visual function in this EAE animal model, then the VA measurement provides an indirect measure of optic nerve electrical competence. As expected, the VA in EAE optic neuritis eyes was significantly lower than that in sham eyes (Fig. 2A) in the current study. Subsequent histological results of these same optic nerves revealed axonal injury, demyelination, and inflammation (Figs. 3C, F, and I), suggesting that these optic-nerve-specific pathologies were a primary source of the impaired visual function in EAE mice.

Based on VEP measurement in the mouse visual system, the optimal visual stimulation condition in C57BL/6 mice has been determined (Ridder and Nusinowitz, 2006) and applied to this study. During diffusion measurement with visual stimulation, decreased ADC_{\perp} and unchanged ADC_{\parallel} were observed in unblocked and blocked normal (sham) eyes, respectively (Figs. 2B and C), suggesting that the ADC_{\perp} directly revealed the effect of functional activation in optic nerves. For the unblocked eyes, the ADC_{\perp} change in EAE-affected optic nerves was less than that in sham optic nerves and provides some measure of the extent of axonal dysfunction (Figs. 2B and C).

Since contributions from retinal dysfunction at the early time point measured herein may (Quinn et al., 2011; Shindler et al., 2008) or may not (Meyer et al., 2001) be ruled out, the RGC (retinal ganglion cell) histological data of our own EAE model were confirmed before this study. The RGC counting results of sham and EAE-affected groups at these early time-points were no different, and suggested that RGC pathologies may occur later in the progression of optic neuritis (Chiang et al., unpublished). Therefore, the attenuated diffusion fMRI response (reduced ADC_{\perp} decrease with stimulation) is likely a direct result of axonal dysfunction. The somewhat elevated baseline ADC_{\perp} in EAE optic neuritis (Table 2) may result from acute demyelination or vasogenic

edema since radial diffusivity or ADC increases reflecting those two pathologies have been reported in EAE mice and MS patients (Boretius et al., 2008; Castriota-Scanderbeg et al., 2002; Chiang et al., 2012; Hickman et al., 2004; Song et al., 2005; Sun et al., 2007).

Our results showed that the functional deficits in EAE-affected optic nerves using diffusion fMRI provide a unique perspective on the consequences of inflammatory demyelinating pathologies. Since the EAE optic neuritis nerves at the acute stage exhibit multiple coexisting pathologies, it is not possible to determine contributions of each specific type of tissue damage to the overall reduced activation-associated ADC_{\perp} response. Consequently, pre-onset study for EAE optic neuritis would be needed to understand if functional deficits precede morphological changes and the inter-relationship between mild injury and diffusion fMRI activation. In vivo diffusion fMRI is a promising tool for direct investigations of evolving pathology, therapeutic targets, and/or longitudinal assessment in white-matter tracts.

Acknowledgments

The authors thank Mr. Bob Mikesell for his excellent technical assistance. This study was supported in part by the grants from the National Institutes of Health R01-NS047592 (S.-K.S.) and P01-NS059560 (A.H.C.) and the National Multiple Sclerosis Society (NMSS) RG 4549A4/1 (S.-K.S.) and an NMSS Pilot Award PP1865 (W.M.S.).

References

- Adamczak, J.M., Farr, T.D., Seehafer, J.U., Kalthoff, D., Hoehn, M., 2010. High field BOLD response to forepaw stimulation in the mouse. *Neuroimage* 51, 704–712.
- Arnold, A.C., 2005. Evolving management of optic neuritis and multiple sclerosis. *Am J. Ophthalmol.* 139, 1101–1108.
- Bay, V., Butt, A.M., 2012. Relationship between glial potassium regulation and axon excitability: a role for glial Kir4.1 channels. *Glia* 60, 651–660.
- Beck, R.W., Trobe, J.D., Moke, P.S., Gal, R.L., Xing, D., Bhatti, M.T., Brodsky, M.C., Buckley, E. G., Chrousos, G.A., Corbett, J., Eggenberger, E., Goodwin, J.A., Katz, B., Kaufman, D.I., Keltner, J.L., Kupersmith, M.J., Miller, N.R., Nazarian, S., Orengo-Nania, S., Savino, P.J., Shults, W.T., Smith, C.H., Wall, M., 2003. High- and low-risk profiles for the development of multiple sclerosis within 10 years after optic neuritis: experience of the optic neuritis treatment trial. *Arch. Ophthalmol.* 121, 944–949.

- Blewitt, E.S., Pogmore, T., Talbot, I.C., 1982. Double embedding in agar/paraffin wax as an aid to orientation of mucosal biopsies. *J. Clin. Pathol.* 35, 365.
- Boretius, S., Gadjanski, I., Demmer, I., Bahr, M., Diem, R., Michaelis, T., Frahm, J., 2008. MRI of optic neuritis in a rat model. *Neuroimage* 41, 323–334.
- Brodsky, M., Nazarian, S., Orengo-Nania, S., Hutton, G.J., Buckley, E.G., Massey, E.W., Bhatti, M.T., Greer, M., Goodwin, J., Wall, M., Savino, P.J., Leist, T., Miller, N.R., Irani, D., Trobe, J.D., Cornblath, W., Kaufman, D.L., Eggenberger, E., Kupersmith, M.J., Shults, W.T., McAllister, L., Hamilton, S., Beck, R.W., Dontchev, M., Gal, R.L., Kollman, C., Keltner, J. L., Smith, C.H., Grp, O.N.S., 2008. Multiple sclerosis risk after optic neuritis — final optic neuritis treatment trial follow-up. *Arch. Neurol.* 65, 727–732.
- Broom, K.A., Anthony, D.C., Blamire, A.M., Waters, S., Styles, P., Perry, V.H., Sibson, N.R., 2005. MRI reveals that early changes in cerebral blood volume precede blood–brain barrier breakdown and overt pathology in MS-like lesions in rat brain. *J. Cereb. Blood Flow Metab.* 25, 204–216.
- Bruck, W., Bitsch, A., Kolenda, H., Bruck, Y., Stiefel, M., Lassmann, H., 1997. Inflammatory central nervous system demyelination: correlation of magnetic resonance imaging findings with lesion pathology. *Ann. Neurol.* 42, 783–793.
- Budde, M.D., Xie, M., Cross, A.H., Song, S.K., 2009. Axial diffusivity is the primary correlate of axonal injury in the experimental autoimmune encephalomyelitis spinal cord: a quantitative pixelwise analysis. *J. Neurosci.* 29, 2805–2813.
- Castriota-Scanderbeg, A., Sabatini, U., Fasano, F., Floris, R., Fraracci, L., Mario, M.D., Nocentini, U., Caltagirone, C., 2002. Diffusion of water in large demyelinating lesions: a follow-up study. *Neuroradiology* 44, 764–767.
- Chiang, C.W., Wang, Y., Lin, T.H., Cross, A.H., Song, S.K., 2012. Acute visual function impairment in EAE is primarily caused by optic nerve inflammation as assessed by DBSI. *Proc. Int. Soc. Magn. Reson. Med.* 20, 3058.
- Compston, A., Coles, A., 2008. Multiple sclerosis. *Lancet* 372, 1502–1517.
- Craner, M.J., Damarjian, T.G., Liu, S., Hains, B.C., Lo, A.C., Black, J.A., Newcombe, J., Cuzner, M.L., Waxman, S.G., 2005. Sodium channels contribute to microglia/macrophage activation and function in EAE and MS. *Glia* 49, 220–229.
- Darquie, A., Poline, J.B., Poupon, C., Saint-Jalmes, H., Le Bihan, D., 2001. Transient decrease in water diffusion observed in human occipital cortex during visual stimulation. *Proc. Natl. Acad. Sci. U. S. A.* 98, 9391–9395.
- Diem, R., Sattler, M.B., Merkler, D., Demmer, I., Maier, K., Stadelmann, C., Ehrenreich, H., Bahr, M., 2005. Combined therapy with methylprednisolone and erythropoietin in a model of multiple sclerosis. *Brain* 128, 375–385.
- Diem, R., Demmer, I., Boretius, S., Merkler, D., Schmeling, B., Williams, S.K., Sattler, M.B., Bahr, M., Michaelis, T., Frahm, J., Bruck, W., Fuchs, E., 2008. Autoimmune optic neuritis in the common marmoset monkey: comparison of visual evoked potentials with MRI and histopathology. *Invest. Ophthalmol. Vis. Sci.* 49, 3707–3714.
- Douglas, R.M., Alam, N.M., Silver, B.D., McGill, T.J., Tschetter, W.W., Prusky, G.T., 2005. Independent visual threshold measurements in the two eyes of freely moving rats and mice using a virtual-reality optokinetic system. *Vis. Neurosci.* 22, 677–684.
- Emerson, M.R., Gallagher, R.J., Marquis, J.G., LeVine, S.M., 2009. Enhancing the ability of experimental autoimmune encephalomyelitis to serve as a more rigorous model of multiple sclerosis through refinement of the experimental design. *Comp. Med.* 59, 112–128.
- Filippi, M., 2003. MRI-clinical correlations in the primary progressive course of MS: new insights into the disease pathophysiology from the application of magnetization transfer, diffusion tensor, and functional MRI. *J. Neurol. Sci.* 206, 157–164.
- Filippi, M., Campi, A., Martinelli, V., Colombo, B., Yousry, T., Canal, N., Scotti, G., Comi, G., 1995. Comparison of triple dose versus standard dose gadolinium-DTPA for detection of MRI enhancing lesions in patients with primary progressive multiple sclerosis. *J. Neurol. Neurosurg. Psychiatry* 59, 540–544.
- Filippi, M., Rocca, M.A., Barkhof, F., Bruck, W., Chen, J.T., Comi, G., DeLuca, G., De Stefano, N., Erickson, B.J., Evangelou, N., Fazekas, F., Geurts, J.J., Lucchinetti, C., Miller, D.H., Pelletier, D., Popescu, B.F., Lassmann, H., 2012. Association between pathological and MRI findings in multiple sclerosis. *Lancet Neurol.* 11, 349–360.
- Flint, J., Hansen, B., Vestergaard-Poulsen, P., Blackband, S.J., 2009. Diffusion weighted magnetic resonance imaging of neuronal activity in the hippocampal slice model. *Neuroimage* 46, 411–418.
- Gallo, A., Esposito, F., Sacco, R., Docimo, R., Bisecco, A., Della Corte, M., D'Ambrosio, A., Corbo, D., Rosa, N., Lanza, M., Cirillo, S., Bonavita, S., Tedeschi, G., 2012. Visual resting-state network in relapsing-remitting MS with and without previous optic neuritis. *Neurology* 79, 1458–1465.
- Gawryluk, J.R., Brewer, K.D., Beyea, S.D., D'Arcy, R.C., 2009. Optimizing the detection of white matter fMRI using asymmetric spin echo spiral. *Neuroimage* 45, 83–88.
- Ge, Y., 2006. Multiple sclerosis: the role of MR imaging. *AJNR Am. J. Neuroradiol.* 27, 1165–1176.
- Gold, R., Linington, C., Lassmann, H., 2006. Understanding pathogenesis and therapy of multiple sclerosis via animal models: 70 years of merits and culprits in experimental autoimmune encephalomyelitis research. *Brain* 129, 1953–1971.
- Heeger, D.J., Ress, D., 2002. What does fMRI tell us about neuronal activity? *Nat. Rev. Neurosci.* 3, 142–151.
- Hickman, S.J., Toosy, A.T., Jones, S.J., Altmann, D.R., Miszkil, K.A., MacManus, D.G., Barker, G.J., Plant, G.T., Thompson, A.J., Miller, D.H., 2004. A serial MRI study following optic nerve mean area in acute optic neuritis. *Brain* 127, 2498–2505.
- Holthoff, K., Witte, O.W., 1996. Intrinsic optical signals in rat neocortical slices measured with near-infrared dark-field microscopy reveal changes in extracellular space. *J. Neurosci.* 16, 2740–2749.
- Inglese, M., Bester, M., 2010. Diffusion imaging in multiple sclerosis: research and clinical implications. *NMR Biomed.* 23, 865–872.
- Kole, M.H., Ilschner, S.U., Kampa, B.M., Williams, S.R., Ruben, P.C., Stuart, G.J., 2008. Action potential generation requires a high sodium channel density in the axon initial segment. *Nat. Neurosci.* 11, 178–186.
- Kornek, B., Storch, M.K., Bauer, J., Djamshidian, A., Weissert, R., Wallstroem, E., Steffler, A., Zimprich, F., Olsson, T., Linington, C., Schmidbauer, M., Lassmann, H., 2001. Distribution of a calcium channel subunit in dystrophic axons in multiple sclerosis and experimental autoimmune encephalomyelitis. *Brain* 124, 1114–1124.
- Le Bihan, D., 2007. The 'wet mind': water and functional neuroimaging. *Phys. Med. Biol.* 52, R57–R90.
- Le Bihan, D., 2012. Diffusion, confusion and functional MRI. *Neuroimage* 62, 1131–1136.
- Le Bihan, D., Johansen-Berg, H., 2012. Diffusion MRI at 25: exploring brain tissue structure and function. *Neuroimage* 61, 324–341.
- Le Bihan, D., Urayama, S., Aso, T., Hanakawa, T., Fukuyama, H., 2006. Direct and fast detection of neuronal activation in the human brain with diffusion MRI. *Proc. Natl. Acad. Sci. U. S. A.* 103, 8263–8268.
- Logothetis, N.K., 2008. What we can do and what we cannot do with fMRI. *Nature* 453, 869–878.
- Logothetis, N.K., Pauls, J., Augath, M., Trinath, T., Oeltermann, A., 2001. Neurophysiological investigation of the basis of the fMRI signal. *Nature* 412, 150–157.
- Matsunaga, Y., Kezuka, T., An, X., Fujita, K., Matsuyama, N., Matsuda, R., Usui, Y., Yamakawa, N., Kuroda, M., Goto, H., 2012. Visual functional and histopathological correlation in experimental autoimmune optic neuritis. *Invest. Ophthalmol. Vis. Sci.* 53, 6964–6971.
- Meyer, R., Weissert, R., Diem, R., Storch, M.K., de Graaf, K.L., Kramer, B., Bahr, M., 2001. Acute neuronal apoptosis in a rat model of multiple sclerosis. *J. Neurosci.* 21, 6214–6220.
- Naismith, R.T., Xu, J., Tutlam, N.T., Trinkaus, K., Cross, A.H., Song, S.K., 2010. Radial diffusivity in remote optic neuritis discriminates visual outcomes. *Neurology* 74, 1702–1710.
- Nessler, S., Boretius, S., Stadelmann, C., Bittner, A., Merkler, D., Hartung, H.P., Michaelis, T., Bruck, W., Frahm, J., Sommer, N., Hemmer, B., 2007. Early MRI changes in a mouse model of multiple sclerosis are predictive of severe inflammatory tissue damage. *Brain* 130, 2186–2198.
- Nicholls, J.G., Kuffler, S.W., Robert, M.A., 2001. From Neuron to Brain, 4th ed. Sinauer Associates, Sunderland, Mass.
- Nicholson, C., Sykova, E., 1998. Extracellular space structure revealed by diffusion analysis. *Trends Neurosci.* 21, 207–215.
- Prusky, G.T., Alam, N.M., Beekman, S., Douglas, R.M., 2004. Rapid quantification of adult and developing mouse spatial vision using a virtual optomotor system. *Invest. Ophthalmol. Vis. Sci.* 45, 4611–4616.
- Quinn, T.A., Dutt, M., Shindler, K.S., 2011. Optic neuritis and retinal ganglion cell loss in a chronic murine model of multiple sclerosis. *Front. Neurol.* 2, 50.
- Ransom, B.R., Orkand, R.K., 1996. Glial–neuronal interactions in non-synaptic areas of the brain: studies in the optic nerve. *Trends Neurosci.* 19, 352–358.
- Ransom, B.R., Yamate, C.L., Connors, B.W., 1985. Activity-dependent shrinkage of extracellular space in rat optic nerve: a developmental study. *J. Neurosci.* 5, 532–535.
- Raz, E., Bester, M., Sigmund, E.E., Tabesh, A., Babb, J.S., Jaggi, H., Helsen, J., Mitnick, R.J., Inglese, M., 2013. A better characterization of spinal cord damage in multiple sclerosis: a diffusional kurtosis imaging study. *AJNR Am. J. Neuroradiol.* 34 (9), 1846–1852.
- Ridder III, W.H., Nusinowitz, S., 2006. The visual evoked potential in the mouse—origins and response characteristics. *Vis. Res.* 46, 902–913.
- Rocca, M.A., Absinta, M., Filippi, M., 2012a. The role of advanced magnetic resonance imaging techniques in primary progressive MS. *J. Neurol.* 259, 611–621.
- Rocca, M.A., Valsasina, P., Martinelli, V., Misci, P., Falini, A., Comi, G., Filippi, M., 2012b. Large-scale neuronal network dysfunction in relapsing-remitting multiple sclerosis. *Neurology* 79, 1449–1457.
- Roosendaal, S.D., Geurts, J.J., Vrenken, H., Hulst, H.E., Cover, K.S., Castelijns, J.A., Pouwels, P. J., Barkhof, F., 2009. Regional DTI differences in multiple sclerosis patients. *Neuroimage* 44, 1397–1403.
- Sahraian, M.A., Eshaghi, A., 2010. Role of MRI in diagnosis and treatment of multiple sclerosis. *Clin. Neurol. Neurosurg.* 112, 609–615.
- Schwartzkroin, P.A., Baraban, S.C., Hochman, D.W., 1998. Osmolarity, ionic flux, and changes in brain excitability. *Epilepsy Res.* 32, 275–285.
- Shindler, K.S., Ventura, E., Dutt, M., Rostami, A., 2008. Inflammatory demyelination induces axonal injury and retinal ganglion cell apoptosis in experimental optic neuritis. *Exp. Eye Res.* 87, 208–213.
- Smith, K.J., Lassmann, H., 2002. The role of nitric oxide in multiple sclerosis. *Lancet Neurol.* 1, 232–241.
- Song, S.K., Sun, S.W., Ju, W.K., Lin, S.J., Cross, A.H., Neufeld, A.H., 2003. Diffusion tensor imaging detects and differentiates axon and myelin degeneration in mouse optic nerve after retinal ischemia. *Neuroimage* 20, 1714–1722.
- Song, S.K., Yoshino, J., Le, T.Q., Lin, S.J., Sun, S.W., Cross, A.H., Armstrong, R.C., 2005. Demyelination increases radial diffusivity in corpus callosum of mouse brain. *Neuroimage* 26, 132–140.
- Spees, W.M., Lin, T.H., Song, S.K., 2013. White-matter diffusion fMRI of mouse optic nerve. *Neuroimage* 65, 209–215.
- Staffen, W., Mair, A., Zauner, H., Unterrainer, J., Niederhofer, H., Kutzelnigg, A., Ritter, S., Golaszewski, S., Iglseder, B., Ladurner, G., 2002. Cognitive function and fMRI in patients with multiple sclerosis: evidence for compensatory cortical activation during an attention task. *Brain* 125, 1275–1282.
- Stejskal, E.O., Tanner, J.E., 1965. Spin diffusion measurements: spin echoes in the presence of a time-dependent field gradient. *J. Chem. Phys.* 42, 288–292.
- Stys, P.K., 2005. General mechanisms of axonal damage and its prevention. *J. Neurol. Sci.* 233, 3–13.
- Su, K.G., Banker, G., Bourdette, D., Forte, M., 2009. Axonal degeneration in multiple sclerosis: the mitochondrial hypothesis. *Curr. Neurol. Neurosci. Rep.* 9, 411–417.
- Sun, S.W., Liang, H.F., Schmidt, R.E., Cross, A.H., Song, S.K., 2007. Selective vulnerability of cerebral white matter in a murine model of multiple sclerosis detected using diffusion tensor imaging. *Neurobiol. Dis.* 28, 30–38.
- Sun, S.W., Liang, H.F., Cross, A.H., Song, S.K., 2008. Evolving Wallerian degeneration after transient retinal ischemia in mice characterized by diffusion tensor imaging. *Neuroimage* 40, 1–10.

- Trapp, B.D., Nave, K.A., 2008. Multiple sclerosis: an immune or neurodegenerative disorder? *Annu. Rev. Neurosci.* 31, 247–269.
- Tsurugizawa, T., Djemai, B., Ciobanu, L., Le Bihan, D., 2013. Diffusion fMRI can detect neural activation when the BOLD fMRI response is abolished by nitroprussiate. *Proc. Int. Soc. Magn. Reson. Med.* 21, 0416.
- Tu, T.W., Budde, M.D., Quirk, J.D., Song, K.S., 2010. Using absorption-mode images to improve in vivo DTI quality. *Proc. Int. Soc. Magn. Reson. Med.* 18, 4001.
- Tu, T.W., Wang, Y., Chiang, C.W., Lin, T.H., Chen, Y.J., Cross, A.H., Song, S.K., 2012. Diffusion basis spectrum imaging detects evolving axonal injury, demyelination and inflammation in the course of EAE. *Proc. Int. Soc. Magn. Reson. Med.* 20, 3598.
- van Walderveen, M.A., Kamphorst, W., Scheltens, P., van Waesberghe, J.H., Ravid, R., Valk, J., Polman, C.H., Barkhof, F., 1998. Histopathologic correlate of hypointense lesions on T1-weighted spin-echo MRI in multiple sclerosis. *Neurology* 50, 1282–1288.
- Wang, Y., Wang, Q., Haldar, J.P., Yeh, F.C., Xie, M., Sun, P., Tu, T.W., Trinkaus, K., Klein, R.S., Cross, A.H., Song, S.K., 2011. Quantification of increased cellularity during inflammatory demyelination. *Brain* 134, 3590–3601.
- Waxman, S.G., 1977. Conduction in myelinated, unmyelinated, and demyelinated fibers. *Arch. Neurol.* 34, 585–589.
- Waxman, S.G., 2006. Axonal conduction and injury in multiple sclerosis: the role of sodium channels. *Nat. Rev. Neurosci.* 7, 932–941.
- Wu, Q., Butzkueven, H., Gresle, M., Kirchhoff, F., Friedhuber, A., Yang, Q., Wang, H., Fang, K., Lei, H., Egan, G.F., Kilpatrick, T.J., 2007. MR diffusion changes correlate with ultra-structurally defined axonal degeneration in murine optic nerve. *Neuroimage* 37, 1138–1147.
- Zhang, C.L., Wilson, J.A., Williams, J., Chiu, S.Y., 2006. Action potentials induce uniform calcium influx in mammalian myelinated optic nerves. *J. Neurophysiol.* 96, 695–709.

Diffusion basis spectrum imaging detects and distinguishes coexisting subclinical inflammation, demyelination and axonal injury in experimental autoimmune encephalomyelitis mice

Xiaojie Wang^a, Matthew F. Cusick^b, Yong Wang^c, Peng Sun^c, Jane E. Libbey^b, Kathryn Trinkaus^d, Robert S. Fujinami^b and Sheng-Kwei Song^{c,e*}

Clinicopathological paradox has hampered significantly the effective assessment of the efficacy of therapeutic intervention for multiple sclerosis. Neuroimaging biomarkers of tissue injury could guide more effective treatment by accurately reflecting the underlying subclinical pathologies. Diffusion tensor imaging-derived directional diffusivity and anisotropy indices have been applied to characterize white matter disorders. However, these biomarkers are sometimes confounded by the complex pathologies seen in multiple sclerosis and its animal models. Recently, a novel technique of diffusion basis spectrum imaging has been developed to quantitatively assess axonal injury, demyelination and inflammation in a mouse model of inflammatory demyelination. Lenaldegkar, which inhibits T-cell expansion in a non-cytolytic manner, has been shown to suppress relapses and preserve white matter integrity in mice with experimental autoimmune encephalomyelitis. In this study, relapsing–remitting experimental autoimmune encephalomyelitis was induced through active immunization of SJL/J mice with a myelin proteolipid protein peptide. The therapeutic efficacy of Lenaldegkar treatment was evaluated via daily clinical score, cross-sectional *ex vivo* diffusion basis spectrum imaging examination and histological analysis. Lenaldegkar greatly reduced relapse severity and protected white matter integrity in these experimental autoimmune encephalomyelitis mice. Diffusion basis spectrum imaging-derived axial diffusivity, radial diffusivity and restricted diffusion tensor fraction accurately reflected axonal injury, myelin integrity and inflammation-associated cellularity change, respectively. These results support the potential use of diffusion basis spectrum imaging as an effective outcome measure for preclinical drug evaluation. Copyright © 2014 John Wiley & Sons, Ltd.

Keywords: multiple sclerosis; diffusion MRI; axonal injury; inflammation; demyelination; diffusion basis spectrum imaging (DBSI); Lenaldegkar; experimental autoimmune encephalomyelitis (EAE)

INTRODUCTION

Multiple sclerosis is an inflammatory demyelinating disorder of the central nervous system (CNS) characterized by lymphocytic infiltration and axon and myelin injury (1). Although inflammatory demyelination is the hallmark of white matter pathology, axonal injury is now widely accepted to play a significant role in irreversible neurological disability (1,2). Currently, an

efficacious therapy to stop the progressive neurodegeneration in multiple sclerosis is not available.

Myelin-specific autoreactive T cells mediate early lesion formation (3) and correlate with the extent of acute axonal injury in multiple sclerosis (4). Thus, autoreactive T-cell modulation may be a potential therapeutic approach for human multiple sclerosis. Lenaldegkar (LDK), 1H-indole-3-carbaldehyde quinolin-8-yl-hydrazone, is an anti-leukemia agent proven to effectively

* Correspondence to: S.-K. Song, Professor of Radiology, Room 2313, East Building, Campus Box 8227, Washington University School of Medicine, 4525 Scott Ave., St. Louis, MO 63110, USA.
E-mail: ssong@wustl.edu

a X. Wang
Department of Chemistry, Washington University, St. Louis, MO, USA

b M. F. Cusick, J. E. Libbey, R. S. Fujinami
Department of Pathology, University of Utah School of Medicine, Salt Lake City, UT, USA

c Y. Wang, P. Sun, S.-K. Song
Department of Radiology, Washington University, St. Louis, MO, USA

d K. Trinkaus
Department of Biostatistics, Washington University, St. Louis, MO, USA

e S.-K. Song
Hope Center for Neurological Disorders, Washington University, St. Louis, MO, USA

Abbreviations used: CFA, complete Freund's adjuvant; CNS, central nervous system; CS, clinical score; DAPI, 4',6-diamidino-2-phenylindole; DBSI, diffusion basis spectrum imaging; DMSO, dimethyl sulfoxide; DTI, diffusion tensor imaging; EAE, experimental autoimmune encephalomyelitis; IHC, immunohistochemistry; LDK, Lenaldegkar; MBP, myelin basic protein; mTOR, mammalian target of rapamycin; PBS, phosphate-buffered saline; PI3K, phosphatidylinositol 3-kinase; PLP, proteolipid protein; RA, relative anisotropy; ROI, region of interest; VLWM, ventral–lateral white matter.

eliminate immature T cells (5). It has been shown to inhibit relapses and to reduce demyelination in mice with experimental autoimmune encephalomyelitis (EAE) (6).

With promising new therapies for multiple sclerosis on the horizon, novel neuroimaging modalities providing quantitative assessment of CNS axonal integrity are needed to non-invasively assess treatment efficacy. Conventional MRI has revolutionized the diagnosis of multiple sclerosis. Nevertheless, it is hardly quantitative and lacks specificity with regard to the differentiation of complicated pathologies. Advanced MR methods, such as myelin water imaging (7) and magnetization transfer ratio (8), have emerged to reflect myelin integrity in multiple sclerosis. Diffusion tensor imaging (DTI) has shown promise for the differentiation between axon and myelin pathologies through changes in axial diffusivity ($\lambda_{||}$, describing water diffusion parallel to axons) and radial diffusivity (λ_{\perp} , describing water diffusion perpendicular to axons) (9,10). However, the interpretation of these DTI findings is confounded by the presence of inflammation (11,12), tissue loss (13), crossing fibers (14) and cerebrospinal fluid contamination (15,16). A novel diffusion basis spectrum imaging (DBSI) approach has been developed to resolve crossing fiber tracts, remove cerebrospinal fluid partial volume effects and quantitatively assess axonal injury, demyelination and inflammation in a mouse model of cuprizone-induced inflammatory demyelination (17).

In this study, the therapeutic efficacy of LDK treatment was assessed by treating EAE mice at the first relapse. Spinal cords from EAE and control mice were examined using diffusion MRI and immunohistochemistry (IHC). Significant preservation of myelin and axonal integrity was observed by DBSI-derived $\lambda_{||}$ and λ_{\perp} in LDK-treated mice, the extent of inflammation was also accurately reflected by DBSI-derived cellularity. DBSI derived $\lambda_{||}$, λ_{\perp} and cellularity correlated with IHC findings. In contrast, the DTI findings did not accurately reflect the treatment effect. Our studies indicate that DBSI has major advantages over DTI.

MATERIALS AND METHODS

DBSI

The diffusion MRI signals were analyzed according to Equation [1] (17):

$$S_k = \sum_{i=1}^{N_{\text{Aniso}}} f_i e^{-|\vec{b}_k| \lambda_{||i}} e^{-|\vec{b}_k| (\lambda_{||i} - \lambda_{\perp i}) \cos^2 \psi_{ik}} \quad [1]$$

$$+ \int_a^b f(D) e^{-|\vec{b}_k| D} dD \quad (k = 1, 2, 3, \dots)$$

In Equation [1], S_k and $|\vec{b}_k|$ are the diffusion-weighted MR signal and b value of the k th diffusion gradient, N_{Aniso} is the number of anisotropic tensors (reflecting fibers), ψ_{ik} is the angle between the k th diffusion gradient and the principal direction of the i th anisotropic tensor, $\lambda_{||i}$ and $\lambda_{\perp i}$ are the axial and radial diffusivities of the i th anisotropic tensor, f_i is the signal intensity fraction for the i th anisotropic tensor, and a and b are the low and high diffusivity limits for the isotropic diffusion spectrum (reflecting cellularity and edema) $f(D)$. In the present study, a single anisotropic tensor (i.e. $N_{\text{Aniso}} = 1$) fitted the spinal cord white matter well. Thus, the derived $\lambda_{||}$ and λ_{\perp} were interpreted similarly to those derived by DTI, but without extra-axon isotropic tensor components confounding the measurements. The isotropic diffusion spectrum was

tentatively divided on the basis of the apparent diffusion coefficient (ADC) into three components representing cellularity (restricted diffusion), vasogenic edema (hindered diffusion) and cerebrospinal fluid or tissue loss (free diffusion).

Animal preparation

To induce EAE, 15 female SJL/J mice (Jackson Laboratory, Bar Harbor, ME, USA) were injected subcutaneously with 200 μ g/mL of myelin proteolipid protein (PLP) peptide (PLP_{139–151}) in complete Freund's adjuvant (CFA) consisting of incomplete Freund's adjuvant (Pierce Biotechnology, Rockford, IL, USA) containing *Mycobacterium tuberculosis* H37 Ra (2 mg/mL) (Difco Laboratories, Detroit, MI, USA). On days 0 and 2 following immunization, mice were injected intravenously with 100 μ L of *Bordetella pertussis* with an initial concentration of 1.0×10^{11} organisms/mL (Michigan Department of Public Health, Lansing, MI, USA). Five additional mice, which received only CFA in the absence of PLP_{139–151}, served as age- and sex-matched controls (sham group). Mice were scored daily for clinical signs using a standard 0–5 scoring system: 1, limp tail; 2, hind limb weakness sufficient to impair righting; 3, one limb paralyzed; 4, two limbs paralyzed; 5, three or more limbs paralyzed or the animal is moribund (mice were killed if they reached grade 5). At the first remission [clinical score (CS) = 0], five mice were killed and subjected to intra-cardiac perfusion fixation using 0.01 M phosphate-buffered saline (PBS) followed by 4% paraformaldehyde in 0.01 M PBS. Vertebral columns were excised and post-fixed in the same fixative overnight, and then transferred to 0.01 M PBS. Starting at the first relapse (CS ≥ 0.5), the remaining ten EAE mice were injected intraperitoneally with 40 mg/kg/day of LDK ($n = 5$) or vehicle [dimethyl sulfoxide (DMSO), $n = 5$] until the study end point when all EAE mice were at the second remission (CS = 0). All LDK- and vehicle-treated EAE and sham control mice were killed and perfusion fixed at the end point of the study.

MRI

For *ex vivo* MRI scans, excised vertebral columns were placed in 1-mL syringes filled with 0.01 M PBS. A solenoid coil of 8 mm in diameter and 25 mm in length was used for data acquisition. *Ex vivo* diffusion MRI examinations were performed on a 4.7-T Agilent DirectDrive small-animal MRI system (Agilent Technologies, Santa Clara, CA, USA) equipped with Magnex/Agilent HD imaging gradients (Magnex/Agilent, Oxford, UK). The magnet, gradient coil and gradient power supply were interfaced with an Agilent DirectDrive console (Agilent Technologies) controlled by a Linux workstation.

A sagittal image of the mouse vertebral column was acquired using a gradient echo sequence to visualize vertebral disks, as references to plan the target axial images. A diffusion-weighted, multi-echo spin-echo imaging sequence (18) was employed to acquire diffusion-weighted images of eight contiguous transverse slices covering T12 to L2 vertebrae. The acquisition parameters were as follows: field of view, $9 \times 9 \text{ mm}^2$; data matrix, 128×128 (resulting in voxel dimensions of $70 \times 70 \mu\text{m}^2$, zero filled to $35 \times 35 \mu\text{m}^2$); TR = 1.0 s; TE = 38 ms; $\Delta = 20 \text{ ms}$; $\delta = 5 \text{ ms}$; slice thickness, 1.0 mm; 99 diffusion-encoding directions prescribed by placing the position vectors at the grid points (q_x, q_y, q_z) in the three-dimensional q space assuming that $(q_x^2 + q_y^2 + q_z^2) \leq r^2$, where $r = 3$ (17). The maximum b value was 3000 s/mm^2 . The total data acquisition time was 3 h and 31 min.

Histological analysis

Following *ex vivo* imaging, mouse vertebral columns were decalcified for 48 h and then embedded in paraffin. The embedded tissues were sectioned using a sliding microtome set at a thickness of 5 μ m. The slides were then deparaffinized, rehydrated and blocked using 1% bovine serum albumin and 5% goat serum in 0.01 M PBS for 30 min at room temperature. Myelin and axonal integrity were assessed by incubating the processed slides with polyclonal anti-myelin basic protein (anti-MBP; 1 : 500 dilution; Sigma Chemical Company, St. Louis, MO, USA) and monoclonal anti-phosphorylated neurofilaments (SMI31; 1 : 1000 dilution; Convance, Emeryville, CA, USA) antibodies, respectively, at 4°C overnight. After rinsing in 0.01 M PBS for 30 min, the slides were incubated with Alexa Fluor 488 conjugated goat-anti-mouse IgG (H+L) (1 : 400 dilution; Invitrogen Co., Camarillo, CA, USA) antibody for 1 h at room temperature to visualize immunoreactive materials. After washing in 0.01 M PBS for 30 min, the slides were mounted in Vectashield medium with 4',6-diamidino-2-phenylindole (DAPI) (Vector Laboratory, Burlingame, CA, USA). DAPI stains cell nuclei. It was used to validate the reliability of the DBSI-derived restricted isotropic diffusion component as a cellularity marker. Increased cellularity reflects the extent of inflammation as it is commonly seen in CNS inflammation. Images were acquired with a Hamamatsu NanoZoomer 2.0-HT System (Hamamatsu, Shizuoka Prefecture, Japan).

The whole field of each staining (SMI31, MBP or DAPI) image at 40 \times magnification was captured with the same fluorescence light intensity and exposure time. Using ImageJ (<http://rsbweb.nih.gov/ij/>), all captured images were converted to 8-bit gray scale and subjected to background subtraction followed by Gaussian blurring (DAPI images) or edge preservation (SMI31 and MBP images). Then, the DAPI and SMI31 images were segmented using the gray-scale watershed algorithm, quantified using the 'analyze particles' function following threshold. The MBP images, however, were quantified directly using the 'analyze particles' function following automatic threshold without segmentation.

Data analysis

The diffusion-weighted MR data were analyzed via a DTI/DBSI analysis package developed in house using MatLab® (MathWorks, Natick, MA, USA). The ventral-lateral white matter (VLWM) area was manually delineated as the region of interest (ROI) on the b_0 (non-diffusion-weighted) image using ImageJ with customized tools. DTI-derived $\lambda_{||}$, λ_{\perp} and relative anisotropy (RA) maps were used as references whilst defining VLWM ROIs. Group-averaged DTI- and DBSI-derived parameters, SMI31-positive axon density, DAPI-stained cell density and MBP-positive region fraction were compared for the VLWM region between sham control mice, mice with EAE at first remission and mice with EAE at second remission with LDK and vehicle treatment. Wilcoxon rank-sum test was used to determine whether any differences existed among these groups, and a significance level of 0.05 was used for all tests. The p values were adjusted using the false discovery rate to account for the large number of tests. Spearman's rank correlation was used to test for the presence of a monotonic increase or decrease between IHC results and DTI or DBSI parameters. All data are expressed as the mean \pm standard deviation.

RESULTS

LDK prevented EAE relapse

The initial neurological disability associated with an acute attack of EAE in SJL/J mice was observed between days 10 and 12 post-immunization with PLP_{139–151}; the first relapse occurred at days 25–29, and remitted at days 36–37 in vehicle-treated EAE mice (Fig. 1, filled squares). Five EAE mice were killed after the first remission (at day 21). LDK or vehicle treatment was initiated on the day of the observed EAE relapse ($CS \geq 0.5$, day 26) and was continued daily thereafter. The treatment continued until the second remission of all EAE mice (day 37). LDK effectively ameliorated EAE relapse. The mean peak CS during the relapse of the LDK-treated group was 0.8 ± 0.8 , whereas that of the vehicle-treated group was 2.8 ± 0.4 . At day 30 post-immunization and

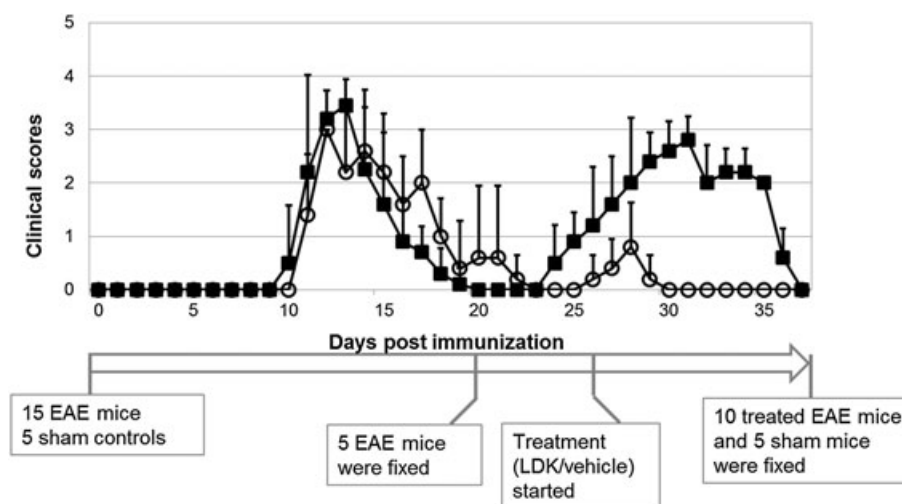


Figure 1. Clinical score time course of Lenaldek (LDK)- and vehicle-treated experimental autoimmune encephalomyelitis (EAE) mice. Female SJL/J mice were immunized with myelin proteolipid protein (PLP) peptide (PLP_{139–151}) in complete Freund's adjuvant (CFA). On EAE relapse at day 26, the mice were injected with LDK (40 mg/kg/day, open circles) or vehicle [dimethyl sulfoxide (DMSO), filled squares] once a day for days 26–37. The mean clinical score was lower in the LDK-treated group during EAE relapse. Data represent mean clinical scores \pm standard deviation for groups of five mice.

beyond, none of the LDK-treated mice showed any clinical signs of disease (Fig. 1, open circles), whereas the vehicle-treated mice still showed significant clinical signs of disease (Fig. 1, filled squares).

DTI detected axonal and myelin injury at remission

Color-coded DTI maps of the VLWM region were overlaid on T_2 -weighted images (Fig. 2). White matter tract lesions were detected on representative DTI parameter maps at the T13 vertebral level of the spinal cord from EAE mice at the first and second remission (Fig. 2). At the first remission, before treatment, decreased $\lambda_{||}$ and RA, as well as increased λ_{\perp} , were visible in the VLWM regions (arrows, second column, Fig. 2). At the second remission, RA and $\lambda_{||}$ showed a further decrease, and λ_{\perp} increased more in the VLWM of vehicle-treated spinal cords (third column, Fig. 2). At the second remission following LDK treatment, normal-appearing VLWM $\lambda_{||}$ was seen (fourth column, Fig. 2). A slight increase in VLWM λ_{\perp} of the LDK-treated mouse resulted in an apparent RA decrease in the same region (arrows, fourth column, Fig. 2).

DBSI detected axon/myelin injury and inflammation at remission

The VLWM of spinal cords from the same representative mice as shown in Fig. 2 was examined using DBSI. Compared with the sham control spinal cord (first column, Fig. 3), the EAE spinal cord exhibited moderately decreased $\lambda_{||}$ in the VLWM at the first remission (arrow, second column, Fig. 3). Increased λ_{\perp} was also observed in the same representative spinal cord (arrows, second column, Fig. 3). At the second remission, increased patchy

lesions can be seen in the VLWM of the vehicle-treated mouse, marked by significantly decreased $\lambda_{||}$ and increased λ_{\perp} (arrows, third column, Fig. 3). In addition, a substantial increase in restricted and hindered diffusion fraction can be seen in the vehicle-treated mouse spinal cord at the second remission (arrows, third column, Fig. 3). With therapeutic LDK treatment (fourth column, Fig. 3), all DBSI parameters of the representative mouse spinal cord exhibited an overall improvement compared with those of the vehicle-treated mouse. Residual patches of lesions remained visible in the λ_{\perp} map.

LDK preserved axons, reduced inflammation and prevented demyelination

In Fig. 4, SMI31 and DAPI double-stained images are shown for the same representative spinal cord from each group at the T13 vertebral level. At the first remission, massive meningeal and perivascular (arrows) cell infiltration was seen in the VLWM (Fig. 4b). At the second remission, a markedly increased and diffuse cell population was observed in the representative vehicle-treated spinal cord, coinciding with substantial loss of SMI31-positive axons (Fig. 4c). In contrast, the representative LDK-treated spinal cord at the second remission exhibited significantly decreased cellularity and increased SMI31-positive axon staining (Fig. 4d). Nevertheless, meningeal cell aggregation (arrows) was still seen in the LDK-treated spinal cord (Fig. 4d). MBP and DAPI double-stained images (Fig. 5) revealed moderate demyelination at the proximity of the meninges with massive cell aggregation at the first remission (Fig. 5b). At the second remission, progression of myelin damage was apparent in the vehicle-treated spinal cord (Fig. 5c). Myelin staining of the spinal

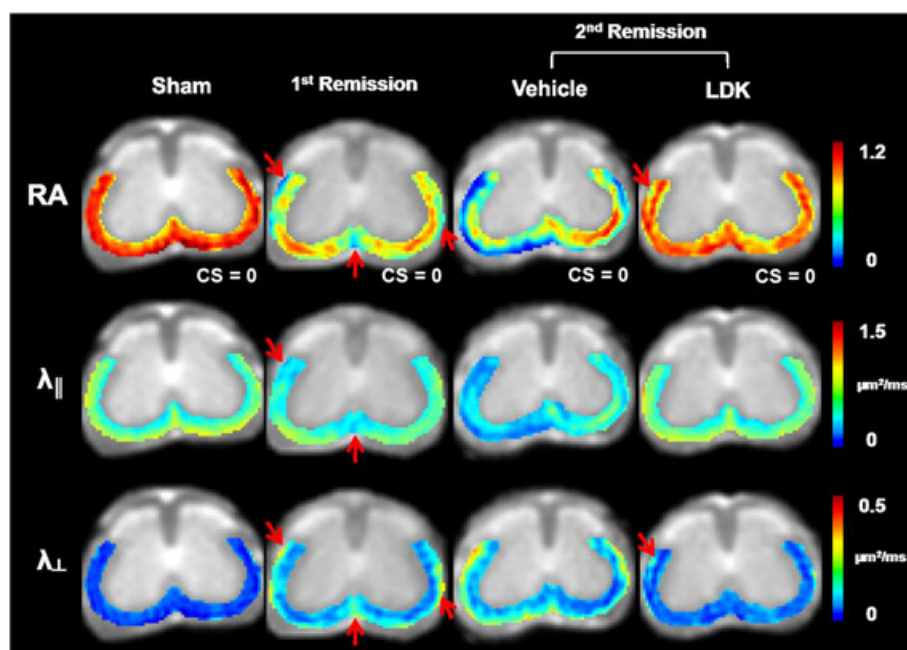


Figure 2. Representative diffusion tensor imaging (DTI) maps. Color-coded relative anisotropy (RA), $\lambda_{||}$ and λ_{\perp} maps of the ventral-lateral white matter (VLWM) region were overlaid on gray-scale T_2 -weighted images. One set of DTI maps is shown for one representative mouse spinal cord at the T13 level from each of the four groups. At the first remission, a decrease in RA was detected at the VLWM, especially in perivascular regions (arrows). Decreased $\lambda_{||}$ and increased λ_{\perp} were also detected in the same areas. At the second remission, the vehicle-treated mouse exhibited markedly decreased RA and $\lambda_{||}$, as well as increased λ_{\perp} . The perivascular and meningeal white matter areas were most severely injured, which formed a 'hypointense border' lining the RA and $\lambda_{||}$ maps. In contrast, the Lenalidekar (LDK)-treated mouse exhibited normalized $\lambda_{||}$ at the second remission. However, slightly increased λ_{\perp} was still seen at the VLWM, resulting in decreased RA (arrows). CS, clinical score.

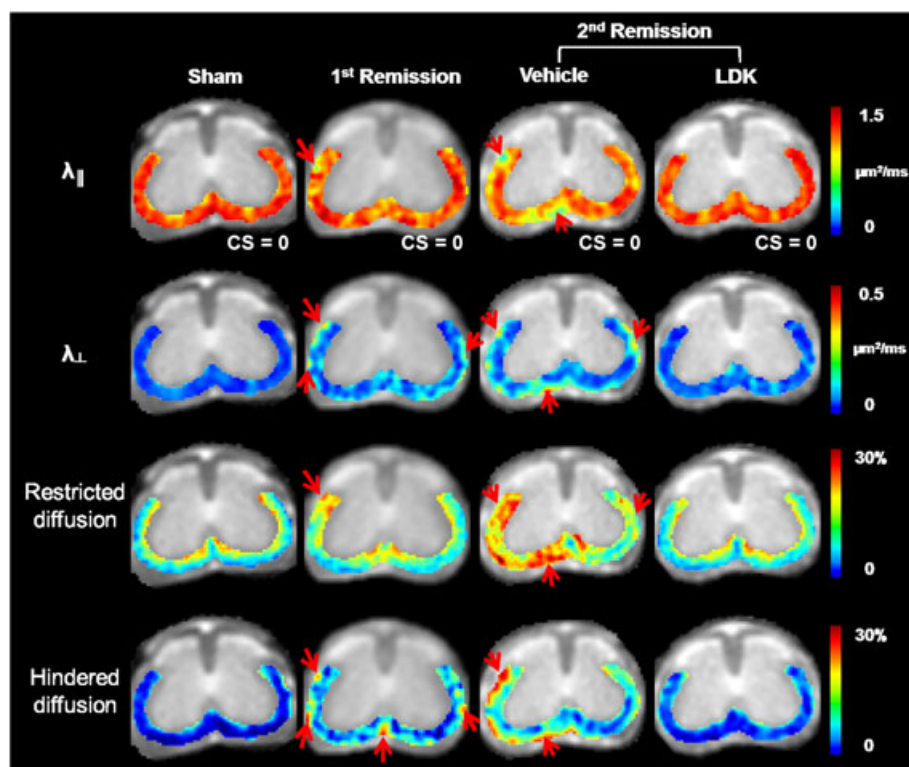


Figure 3. Representative diffusion basis spectrum imaging (DBSI) maps. Color maps of $\lambda_{||}$, λ_{\perp} and restricted and hindered diffusion fractions at the T13 level for the same representative mouse spinal cords as shown in Fig. 2. Compared with the sham mouse, the experimental autoimmune encephalomyelitis (EAE) mouse showed moderately decreased $\lambda_{||}$ in the ventral-lateral white matter (VLWM) at the first remission. An observed increase in λ_{\perp} was detected in the representative spinal cord at this time point (arrows). At the second remission, a further decrease in $\lambda_{||}$ and increase in λ_{\perp} are readily detected in the representative vehicle-treated mouse. Patchy lesions were seen at the periphery of the VLWM, marked by significantly decreased $\lambda_{||}$ and increased λ_{\perp} (arrows). A substantially increased fraction of restricted isotropic diffusion was overwhelmingly seen in the left VLWM. The fraction of hindered isotropic diffusion increased in the peripheral VLWM. With therapeutic Lenalidekar (LDK) treatment, all DBSI parameters were improved compared with those of the vehicle-treated group. The $\lambda_{||}$ and restricted and hindered water ratios of LDK-treated mouse spinal cord were comparable with those of the sham control spinal cord, yet λ_{\perp} was still elevated. CS, clinical score.

cord appeared normal in the representative LDK-treated EAE mouse at the second remission, whereas perivascular and meningeal cell infiltration was still visible (arrows, Fig. 5d).

Group analysis: axonal injury

Because of the exclusion of the isotropic restricted diffusion tensor component with lower apparent diffusion coefficient, the DBSI-derived $\lambda_{||}$ was systematically higher than that derived by conventional DTI (Fig. 6a, b). Axonal injury at the first remission was evidenced by the decreased $\lambda_{||}$ derived by DTI (Fig. 6a) and DBSI (Fig. 6b), as well as by the reduction in the SMI31-positive axon density (Fig. 6c), in mice with EAE. However, none of these differences reached statistical significance compared with control (sham). At the second remission, DTI/DBSI-derived $\lambda_{||}$ and SMI31-positive axon density decreased further in the vehicle-treated EAE mice. The difference between the first and second remission vehicle-treated groups was statistically significant for SMI31-positive axon density. Neither DTI- or DBSI-derived $\lambda_{||}$ in the LDK-treated group at the second remission decreased as seen in the vehicle-treated group. Higher DTI- and DBSI-derived $\lambda_{||}$ was seen in the LDK-treated group than in the vehicle-treated group at the second remission without reaching statistical significance. This is consistent with a significantly higher SMI31-positive axon density in the LDK-treated group compared with the vehicle-treated group at the second remission.

Group analysis: demyelination

Significantly increased λ_{\perp} derived by both DTI and DBSI was seen in EAE mice at the first remission compared with the sham group (Fig. 6d, e). At the second remission, the vehicle-treated EAE mice showed comparable λ_{\perp} relative to the mice at the first remission (Fig. 6d, e). However, mice treated with LDK showed a lower λ_{\perp} at the second remission than non-treated EAE mice at the first remission and vehicle-treated EAE mice at the second remission. In line with these DTI- and DBSI-derived λ_{\perp} findings, reduced MBP staining was seen in EAE groups at the first and second remission (Fig. 6f). LDK treatment improved the myelin integrity at the second remission compared with vehicle treatment, but this improvement did not reach statistical significance.

Group analysis: inflammation

The DBSI-derived fraction of the restricted isotropic diffusion tensor component was increased significantly in EAE mice without treatment at the first remission and in the vehicle-treated group at the second remission, compared with the sham group (Fig. 6g). In the LDK-treated EAE mice, the restricted isotropic diffusion tensor component fraction was decreased compared with that of the first and second remission vehicle-treated group, although statistical significance was not reached. This is consistent with the DAPI-positive nuclear staining results (Fig. 6h).

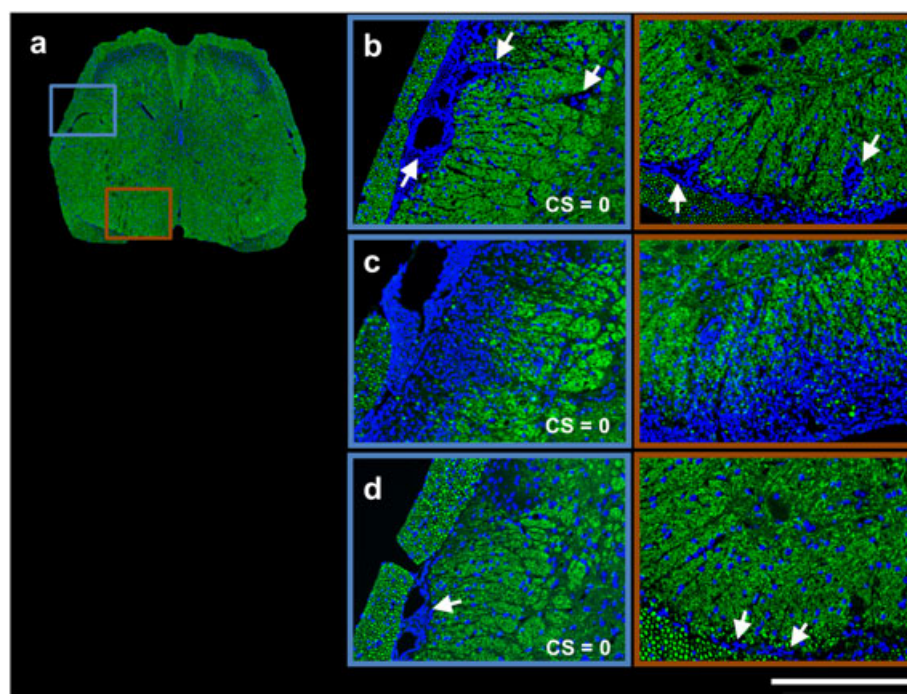


Figure 4. SMI31 and 4',6-diamidino-2-phenylindole (DAPI) double-stained spinal cord images of representative sham control (a), first remission (b), second remission vehicle-treated (c) and second remission Lenalidekar (LDK)-treated (d) mice. Images are shown for the same representative spinal cord as in Figs 2 and 3 from each group at the T13 level. For the representative sham control mouse, the entire spinal cord is displayed (a). For the other three groups, magnified views of the highlighted boxes in (a) are displayed (b–d). At the first remission, massive meningeal cell infiltration (arrows) is readily visible in the ventral–lateral white matter (VLWM) region (b). At the second remission, a markedly increased and diffuse cell population can be seen in the representative vehicle-treated mouse spinal cord, coinciding with substantial loss of SMI31-positive axons (c). In contrast, the representative LDK-treated spinal cord at the second remission exhibits significantly decreased cellularity and increased SMI31-positive axon staining. Nevertheless, meningeal cell aggregation (arrows) is still seen in the LDK-treated spinal cord (d). Scale bar, 250 μ m. CS, clinical score.

Group analysis: correlating diffusion MRI findings with histology

DBSI-derived $\lambda_{||}$ and λ_{\perp} showed strong correlation with SMI31-positive axon density and MBP-positive myelin area, respectively (Fig. 7a, b). The DBSI-derived restricted isotropic diffusion tensor component fraction correlated with the DAPI density (Fig. 7c). The DTI-derived $\lambda_{||}$ did not correlate with SMI31-positive axon counts (Fig. 7d). The DTI-derived λ_{\perp} , however, demonstrated correlation with MBP-positive myelin area with lesser significance than that of DBSI.

DISCUSSION

In this study, we verified the previously reported therapeutic efficacy of LDK in relapsing–remitting EAE in mice (6) by performing a cross-sectional examination of white matter integrity of the spinal cord using both *ex vivo* diffusion MRI and IHC. Diffusion MRI findings supported the utility of the newly developed DBSI technique to not only more accurately reflect axonal and myelin integrity, but also to assess the extent of inflammation. All animals at the time of examination exhibited no hind limb disabilities (CS=0, Fig. 1) with various degrees of white matter pathology reflected by diffusion MRI (Figs. 2 and 3) and IHC (Figs. 4 and 5), suggesting the need for a biomarker to assess disease progression and treatment efficacy, overcoming the clinicopathological paradox.

The sensitivity of *in vivo* DTI-derived $\lambda_{||}$ and λ_{\perp} to reflect IHC-detected axonal and myelin injury in EAE mouse spinal cord

white matter has been reported (19–22). Consistent with previous reports, current *ex vivo* DTI-derived $\lambda_{||}$ and λ_{\perp} correctly reflected lesions detected by SMI31 and MBP staining (Figs. 2, 4 and 5). Perivascular and meningeal lesions were seen in SMI31/MBP images, as well as in DTI-derived $\lambda_{||}$ and λ_{\perp} maps, reflecting the hallmark EAE pathologies. The loss of SMI31 and MBP staining largely appeared at the regions with increased DAPI staining, yet not all SMI31/MBP lesions co-localized with positive DAPI staining. Similar to DTI, DBSI-derived $\lambda_{||}$ and λ_{\perp} also reflected SMI31- and MBP-detected lesions in EAE mice (Figs. 3–5), suggesting a potential role for diffusion MRI as an outcome measure for the assessment of EAE spinal cord pathologies.

It has been reported that the presence of high cellularity decreases the DTI-derived $\lambda_{||}$ (23). Thus, an exaggerated decrease in DTI-derived $\lambda_{||}$ might result from the region in which axonal injury occurs with increased DAPI staining (i.e. increased cellularity associated with inflammation). This could explain the over-estimated axonal injury by DTI in the first remission group compared with the sham group (Fig. 6a). To take this confounding factor into account, DBSI models diffusion MRI signals as a linear combination of anisotropic (discrete axonal fiber tracts) and isotropic (various inter-axonal components reflecting vasogenic edema and cellularity) diffusion tensors. By removing the confounding effect from isotropic diffusion associated with inflammation or tissue loss, DBSI-derived fiber directional diffusivity more accurately reflects the diffusion characters of axonal tracts. Thus, there was a closer trend between DBSI-derived $\lambda_{||}$ and SMI31-positive axon density (Figs. 6b, c) than between DTI-derived $\lambda_{||}$ and SMI31-positive axon density (Figs. 6a, c). In addition, DBSI

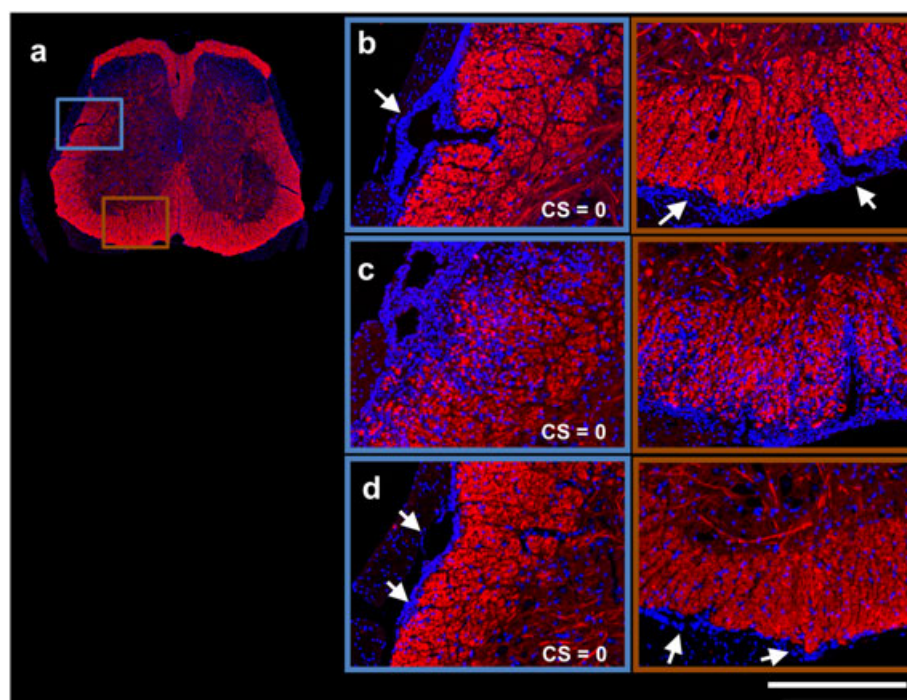


Figure 5. Myelin basic protein (MBP) and 4',6-diamidino-2-phenylindole (DAPI) double-stained spinal cord images of representative sham control (a), first remission (b), second remission vehicle-treated (c) and second remission Lenalidekar (LDK)-treated (d) mice. Images are shown for the same representative spinal cord as in Figs 2–4 from each group at the T13 level. For the representative sham control mouse, the entire spinal cord is displayed (a). For the other three groups, magnified views of the highlighted boxes in (a) are displayed (b–d). The MBP and DAPI double-stained images revealed moderate demyelination at the proximity of the meninges with massive meningeal cell aggregation (arrows) at the first remission (b). At the second remission, progression of myelin damage was apparent in the vehicle-treated spinal cord (c). Myelin staining of the spinal cord appeared normal in the representative LDK-treated experimental autoimmune encephalomyelitis (EAE) mouse, but perivascular and meningeal cell aggregation was still visible (arrows, d). Scale bar, 250 μ m. CS, clinical score.

enables the estimation of increased cellularity (restricted diffusion) and vasogenic edema (hindered isotropic diffusion) associated with inflammation. Although there is no IHC equivalent of vasogenic edema reflected by hindered isotropic diffusion, the restricted diffusion component offers a putative surrogate marker reflecting the extent of increased DAPI-positive nuclear counting (Figs. 3–5).

It is thought that relapsing–remitting EAE is initiated via perivascular and meningeal lymphocyte and neutrophil infiltration, followed by resolution of the inflammatory infiltrate and progression of axon and myelin damage (24). At the first remission, a significant increase in the DBSI-estimated restricted isotropic diffusion tensor fraction (Fig. 6g) and cell density (Fig. 6h) was observed. Meanwhile, we saw a decreased $\lambda_{||}$ and increased λ_{\perp} derived by DBSI in EAE mice at first remission relative to the sham control (Figs. 6b, e). These changes in directional diffusivity were consistent with the observed decrease in SMI31-positive axon density (Fig. 6c) and MBP-positive area fraction (Fig. 6f), respectively. Thus, pathologically, both DBSI and IHC results suggest that moderate axon/myelin damage and only partial resolution of inflammation occurred at the first remission, although full functional recovery was suggested by clinical signs (CS = 0, Fig. 1).

The underlying mechanisms of remission following the acute paralytic attack are not well understood. However, it has been demonstrated that the EAE relapse is mediated predominantly by T cells, specific for endogenous myelin epitopes, which are activated as a result of myelin debris generated from acute inflammatory demyelination, a phenomenon known as epitope

spreading (25,26). At the second remission, further damage to the axons was detected in the spinal cord from vehicle-treated EAE mice using both DBSI (significantly decreased $\lambda_{||}$ compared with that of the sham group) and histology assessment (significantly decreased SMI31-positive axon density compared with that of the first remission) (Figs. 6b, c). Interestingly, the extent of myelin injury seen in the spinal cord from vehicle-treated EAE mice at the second remission was comparable with that at the first remission (Figs. 6e, f). This might be caused by a potential remyelination process occurring in these EAE mice. Meanwhile, further increased cellularity was also observed in the vehicle-treated EAE mouse spinal cord at the second remission (Fig. 6h). Both DBSI and histology results suggested an increased mean cellularity in the VLWM region relative to the first remission, which did not reach statistical significance (Figs. 6g, h).

LDK was first found to be a potent inhibitor of immature leukemic T cells, where it dephosphorylated members of the phosphatidylinositol 3-kinase (PI3K)/AKT/mammalian target of rapamycin (mTOR) pathway and delayed sensitive cells in late mitosis (5). Later, the efficacy of LDK in treating relapsing–remitting EAE in mice was demonstrated, and the mechanism was thought to possibly involve the modulation of highly active T cells in a non-cytolytic manner (6). Here, the treatment efficacy of LDK in the same EAE model was reproduced (Fig. 1). The current findings further demonstrated that cellularity in the LDK-treated group decreased at the second remission compared with that in the vehicle-treated group (Figs. 6g, h). Thus, an overall inflammation suppression effect can be reasonably inferred. In addition, remyelination was also suggested by the improved

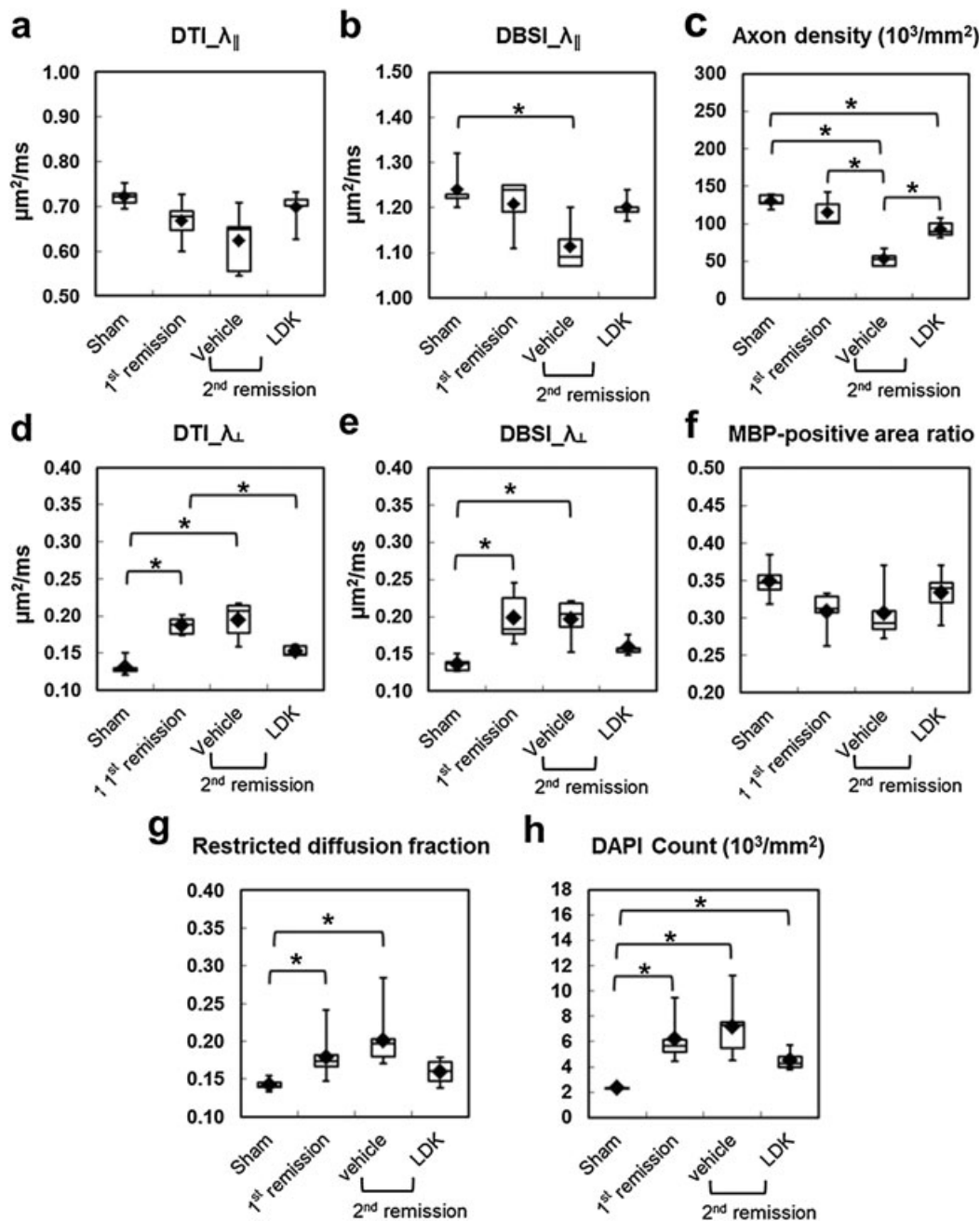


Figure 6. Group analysis of diffusion MR-derived metrics and histology quantifications in the ventral-lateral white matter (VLWM). Group-averaged diffusion tensor imaging (DTI)- (a) and diffusion basis spectrum imaging (DBSI)- (b) derived $\lambda_{||}$, DTI- (d) and DBSI- (e) derived λ_{\perp} , DBSI-derived fraction of restricted diffusion (g) and SMI31-positive axon density (c), myelin basic protein (MBP)-positive area (f) and 4',6-diamidino-2-phenylindole (DAPI)-stained cell density (h) were compared for the VLWM region between sham control, experimental autoimmune encephalomyelitis (EAE) mice at first remission and EAE mice at second remission with Lenalidekar (LDK) and vehicle treatment (five mice per group), as described in the Materials and Methods. DBSI-derived $\lambda_{||}$ (b) was systematically higher than DTI-derived $\lambda_{||}$ (a). LDK-treated mice showed higher DBSI-derived $\lambda_{||}$ (b) and SMI31-positive axon density (c), consistent with the preservation of axons, compared with vehicle-treated mice at the second remission time point. LDK-treated mice showed lower DTI- (d) and DBSI- (without statistical significance) (e) derived λ_{\perp} compared with vehicle-treated mice at the second remission time point and with mice at the first remission time point. LDK treatment also resulted in higher MBP staining, consistent with improved myelin integrity, compared with vehicle-treated mice at the second remission time point and mice at the first remission time point. Meanwhile, LDK-treated mice showed reduced restriction diffusion and cell density compared with vehicle-treated mice at the second remission time point and mice at the first remission time point.

myelin integrity detected by diffusion MRI and IHC after LDK treatment at the onset of EAE relapse (Figs. 6d–f). The improvement in DBSI-derived $\lambda_{||}$ and SMI31-positive axon density in the LDK-treated group compared with the vehicle-treated group at the second remission indicated the potential for axonal

protection by LDK through either anti-inflammatory or potentially direct action (Figs. 6b, c).

In summary, DBSI offered more accurate estimation of white matter integrity relative to DTI in this EAE model, reflected by significantly higher correlation with IHC results. Meanwhile, the

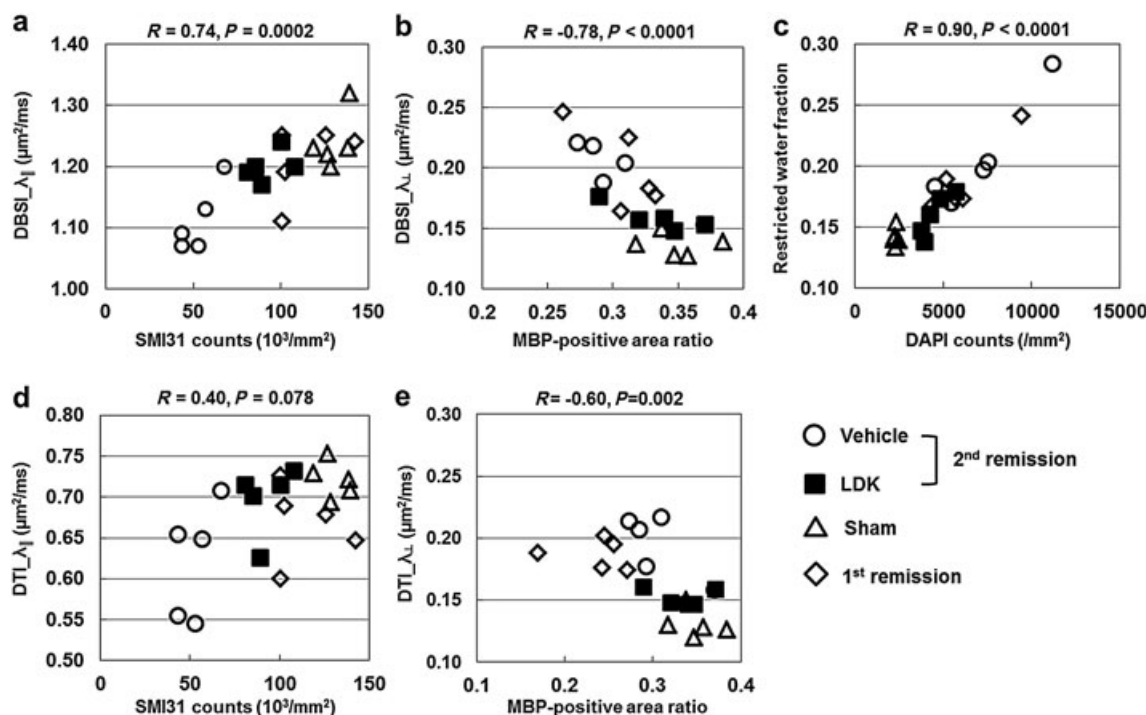


Figure 7. Correlations between diffusion tensor imaging/diffusion basis spectrum imaging (DTI/DBSI)-derived biomarkers and histological quantifications. Correlations between DBSI/DTI-derived $\lambda_{||}$ (a, d) and λ_{\perp} (b, e) and SMI31-positive axon density (a, d) and myelin basic protein (MBP)-positive area (b, e), respectively, and between DBSI-derived fraction of restricted diffusion and 4',6-diamidino-2-phenylindole (DAPI)-stained cell density (c) for individual mice, as determined from the ventral-lateral white matter (VLWM) region of sham control, experimental autoimmune encephalomyelitis (EAE) mice at first remission and EAE mice at second remission with Lenalidekar (LDK) and vehicle treatment (five mice per group). As demonstrated by the R and p values above each graph, correlation is significant in all cases, except for the DTI-derived $\lambda_{||}$ versus SMI31-positive axon count.

DBSI-derived cellularity marker successfully characterized the inflammatory feature of this model and reflected the anti-inflammatory effect of LDK. The excellent linear correlation between the restricted diffusion fraction and DAPI count supports its use as a surrogate marker for cellularity in EAE, multiple sclerosis and other neuroinflammatory disease.

Acknowledgements

We would like to thank Daniel J. Doty for technical assistance. This work was supported in part by the Emma Mary Deland Foundation (RSF), the National Institute of Health T32AI055434 (MFC), R01-NS082102 (RSF), R01-NS047592 (S-KS), P01-NS059560 (S-KS), National Multiple Sclerosis Society (NMSS) RG 4549A4/1 (S-KS) and Department of Defense Ideal Award W81XWH-12-1-0457 (S-KS).

REFERENCES

1. Trapp BD, Nave KA. Multiple sclerosis: an immune or neurodegenerative disorder? *Annu. Rev. Neurosci.* 2008; 31: 247–269.
2. Bitsch A, Schuchardt J, Bunkowski S, Kuhlmann T, Bruck W. Acute axonal injury in multiple sclerosis. Correlation with demyelination and inflammation. *Brain*, 2000; 123(Pt 6): 1174–1183.
3. McFarland HF, Martin R. Multiple sclerosis: a complicated picture of autoimmunity. *Nat. Immunol.* 2007; 8(9): 913–919.
4. Frischer JM, Bramow S, Dal-Bianco A, Lucchinetti CF, Rauschka H, Schmidbauer M, Laursen H, Sorensen PS, Lassmann H. The relation between inflammation and neurodegeneration in multiple sclerosis brains. *Brain*, 2009; 132(Pt 5): 1175–1189.
5. Ridges S, Heaton WL, Joshi D, Choi H, Eiring A, Batchelor L, Choudhry P, Manos EJ, Sofla H, Sanati A, Welborn S, Agarwal A, Spangrude GJ, Miles RR, Cox JE, Frazer JK, Deininger M, Balan K, Sigman M, Muschen M, Perova T, Johnson R, Montpellier B, Guidos CJ, Jones DA, Trede NS. Zebrafish screen identifies novel compound with selective toxicity against leukemia. *Blood*, 2012; 119(24): 5621–5631.
6. Cusick MF, Libbey JE, Trede NS, Eckels DD, Fujinami RS. Human T cell expansion and experimental autoimmune encephalomyelitis inhibited by Lenalidekar, a small molecule discovered in a zebrafish screen. *J. Neuroimmunol.* 2012; 244(1–2): 35–44.
7. MacKay A, Whittall K, Adler J, Li D, Paty D, Graeb D. In vivo visualization of myelin water in brain by magnetic resonance. *Magn. Reson. Med.* 1994; 31(6): 673–677.
8. Chen JT, Kuhlmann T, Jansen GH, Collins DL, Atkins HL, Freedman MS, O'Connor PW, Arnold DL, Canadian MSBMTSG. Voxel-based analysis of the evolution of magnetization transfer ratio to quantify remyelination and demyelination with histopathological validation in a multiple sclerosis lesion. *Neuroimage*, 2007; 36(4): 1152–1158.
9. Song S-K, Sun S-W, Ju W-K, Lin S-J, Cross AH, Neufeld AH. Diffusion tensor imaging detects and differentiates axon and myelin degeneration in mouse optic nerve after retinal ischemia. *Neuroimage*, 2003; 20(3): 1714–1722.
10. Song SK, Sun SW, Ramsbottom MJ, Chang C, Russell J, Cross AH. Demyelination revealed through MRI as increased radial (but unchanged axial) diffusion of water. *Neuroimage*, 2002; 17(3): 1429–1436.
11. Sun SW, Liang HF, Trinkaus K, Cross AH, Armstrong RC, Song SK. Non-invasive detection of cuprizone induced axonal damage and demyelination in the mouse corpus callosum. *Magn. Reson. Med.* 2006; 55(2): 302–308.
12. Xie M, Tobin JE, Budde MD, Chen CI, Trinkaus K, Cross AH, McDaniel DP, Song SK, Armstrong RC. Rostrocaudal analysis of corpus callosum demyelination and axon damage across disease stages refines diffusion tensor imaging correlations with pathological features. *J. Neuropathol. Exp. Neurol.* 2010; 69(7): 704–716.
13. Kim JH, Loy DN, Liang HF, Trinkaus K, Schmidt RE, Song SK. Noninvasive diffusion tensor imaging of evolving white matter pathology in

- a mouse model of acute spinal cord injury. *Magn. Reson. Med.* 2007; 58(2): 253–260.
14. Wheeler-Kingshott CA, Cercignani M. About “axial” and “radial” diffusivities. *Magn. Reson. Med.* 2009; 61(5): 1255–1260.
15. Karampinos DC, Van AT, Olivero WC, Georgiadis JG, Sutton BP. High resolution reduced-FOV diffusion tensor imaging of the human pons with multi-shot variable density spiral at 3T. *Proc. IEEE Eng. Med. Biol. Soc.* 2008; 2008: 5761–5764.
16. Cheng YW, Chung HW, Chen CY, Chou MC. Diffusion tensor imaging with cerebrospinal fluid suppression and signal-to-noise preservation using acquisition combining fluid-attenuated inversion recovery and conventional imaging: comparison of fiber tracking. *Eur. J. Radiol.* 2011; 79(1): 113–117.
17. Wang Y, Wang Q, Haldar JP, Yeh FC, Xie M, Sun P, Trinkaus K, Klein RS, Cross A, Song S. Quantification of increased cellularity during inflammatory demyelination. *Brain*, 2011; 134: 3587–3598.
18. Tu TW, Budde MD, Quirk JD, Song SK. Using absorption-mode images to improve in vivo DTI quality. *Proc. Int. Soc. Magn. Reson. Med.* 2010; 18: 4001.
19. Kim JH, Budde MD, Liang HF, Klein RS, Russell JH, Cross AH, Song SK. Detecting axon damage in spinal cord from a mouse model of multiple sclerosis. *Neurobiol. Dis.* 2006; 21(3): 626–632.
20. Budde MD, Kim JH, Liang HF, Russell JH, Cross AH, Song SK. Axonal injury detected by in vivo diffusion tensor imaging correlates with neurological disability in a mouse model of multiple sclerosis. *NMR Biomed.* 2008; 21(6): 589–597.
21. Cruz-Orengo L, Chen YJ, Kim JH, Dorsey D, Song SK, Klein RS. CXCR7 antagonism prevents axonal injury during experimental autoimmune encephalomyelitis as revealed by in vivo axial diffusivity. *J. Neuroinflamm.* 2011; 8: 170.
22. Wang X, Brieland JK, Kim JH, Chen YJ, O’Neal J, O’Neil SP, Tu TW, Trinkaus K, Song SK. Diffusion tensor imaging detects treatment effects of FTY720 in experimental autoimmune encephalomyelitis mice. *NMR Biomed.* 2013; 26(12): 1742–1750.
23. Wang Y, Wang Q, Haldar JP, Yeh FC, Xie M, Sun P, Tu TW, Trinkaus K, Klein RS, Cross AH, Song SK. Quantification of increased cellularity during inflammatory demyelination. *Brain*, 2011; 134(Pt 12): 3590–3601.
24. Constantinescu CS, Farooqi N, O’Brien K, Gran B. Experimental autoimmune encephalomyelitis (EAE) as a model for multiple sclerosis (MS). *Br. J. Pharmacol.* 2011; 164(4): 1079–1106.
25. McRae BL, Vanderlugt CL, Dal Canto MC, Miller SD. Functional evidence for epitope spreading in the relapsing pathology of experimental autoimmune encephalomyelitis. *J. Exp. Med.* 1995; 182(1): 75–85.
26. McMahon EJ, Bailey SL, Castenada CV, Waldner H, Miller SD. Epitope spreading initiates in the CNS in two mouse models of multiple sclerosis. *Nat. Med.* 2005; 11(3): 335–339.